

MSc in Analysis and Design of Earthquake Resistant Structures

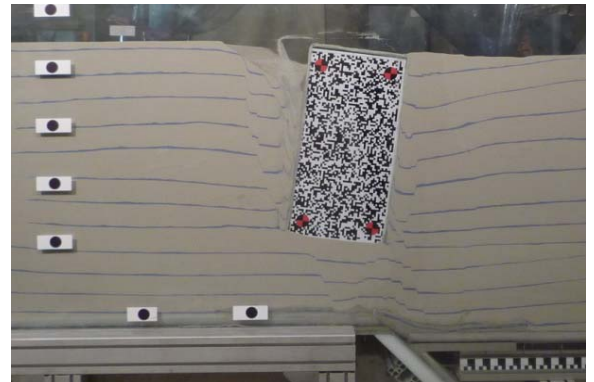
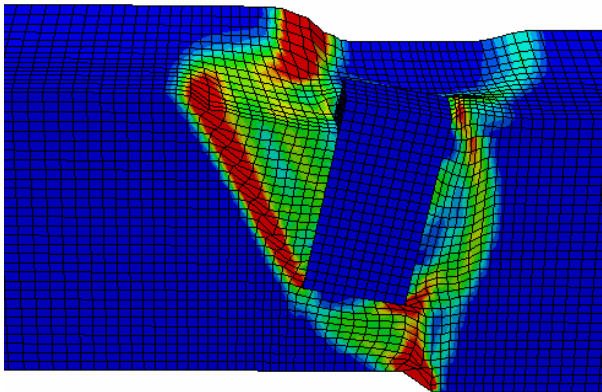
Αλληλεπίδραση Κιβωτιοειδούς Εγκιβωτισμένου  
Θεμελίου με Κανονική και Ανάστροφη Διάρρηξη

Διπλωματική Εργασία

**ΟΡΕΣΤΗ ΖΑΡΖΟΥΡΑ**

Επιβλέποντες:

Καθηγητής **Γεώργιος Γκαζέτας**, Ιωάννης Αναστασόπουλος



**Interaction of Caisson Foundations with Dip - Slip  
Fault Rupture**

Thesis by

**ORESTIS ZARZOURAS**

Supervised by :

Professor **George Gazetas**, Ioannis Anastasopoulos,

February 2011

## *Ευχαριστίες*

Θα ήθελα να εκφράσω τις ειλικρινείς μου ευχαριστίες στον *Καθαγητή μου, Γιώργο Γκαζέτα* για την σπουδαία ευκαιρία που μου έδωσε να δουλέψω και να μαθητέψω κοντά του. Η βοήθειά του και η καθοδήγησή του κατά τη διάρκεια των σπουδών μου και κατά την υλοποίηση αυτής της μεταπτυχιακής εργασίας ήταν καθοριστικές. Οι εύστοχες παρεμβάσεις και παρατηρήσεις του σε όλα τα θέματα βελτίωσαν σίγουρα τον τρόπο με τον οποίο εργάζομαι.

Οφείλω, επίσης, να ευχαριστήσω τον *Γιάννη Αναστασόπουλο*, ο οποίος ήταν πάντα πρόθυμος να μου μεταδώσει τις πλούσιες γνώσεις του και να με βοηθήσει σε κάθε δυσκολία που αντιμετώπισα

Θέλω, τέλος, να ευχαριστήσω τους συνεργάτες μου τόσο στην εργαστηριακή διαδικασία όσο και στην αριθμητική προσομοίωση: *Βασίλη Δρόσο, Τάκη Γεωργαράκο και Μαριάνα Λώλη*, οι οποίοι με τη σειρά τους λειτούργησαν καταλυτικά στην υλοποίηση της εργασίας αυτής.



*Στους γονείς μου*



## ABSTRACT

In many large magnitude earthquakes the causative fault propagates all the way up through the soil and interacts with surface structures. And although, earthquake engineering research and practice has (over the last four decades) emphasized the dynamic response of soil and structural systems to ground oscillations, this should not be taken to imply, that large ground displacements are not a problem, nor that that problem is unsolvable.

Subterranean fault rupture has been responsible for many recorded instances of building damage during past earthquakes. Differential displacement in the ground can cause shearing in overlying structures and can leave structures in an unsupported condition. Structures that are adequately designed against dynamic loads during severe earthquakes may still have a significant risk of failure due to excessive permanent ground deformations induced by surface fault breakage. To take this problem into account, most seismic design codes prevent the erection of structures across, or in the immediate vicinity of seismically active faults. As a reference we recall the *Alquist-Priolo earthquake fault zoning Act* that regulates since 1972 in California the mitigation of hazard of surface faulting to structures and the clause 4.1.2 of the recently approved Part 5 of Eurocode 8 [2].

It should be noted that, a reliable mapping of seismically active faults can be achieved with a reasonable degree of accuracy, at least for the purpose at hand, only in few regions; in most tectonic environments, such as Southern Europe, characterized by diffuse seismicity and seismic faults of relatively small dimensions (up to few tens of km), even the identification of the causative fault of some of the major seismic events may lead seismologists to conflicting viewpoints.

In addition to the uncertainty and inherent lack of completeness related to the mapping activity, it should be remarked that secondary ruptures can also contribute significantly to the overall damage due to excessive ground displacements, and these ruptures can be located at relatively large distances from the main trace of the fault rupture. Several interesting cases are reported for the 1999 Chi-Chi Taiwan earthquake [4] and for the Landers 1992 earthquake in California, where most

ground breakages occurred in an area some tens of meters wide, but extensional cracks were also observed several hundreds of meters from the main trace. Moreover, for long structures, such as bridges, tunnels, pipelines, and embankments, which often cannot avoid crossing such geologic faults, comes the question of the design criteria used. Last but not least, the presence of a structure on top of the soil deposit may further modify the path of the rupture, as the latter propagates from the base rock to the ground surface. Depending on the rigidity of the foundation and the weight of the structure, even a complete diversion of the fault path before it outcrops may take place.

Therefore, at least in the cases of important facilities and infrastructure engineering approaches are needed to limit the damage potential, as the location where the structure will be founded is not a matter of negotiation.

The understanding of the interplay that develops between the propagating fault rupture, the deforming soil under the structure, and the differentially displacing foundation is the aim of this dissertation thesis, as this interplay is of profound significance for the performance of the structure. More specifically, the objective of is to investigate the interaction of rigid embedded foundations, caissons, with dip slip fault imposed deformations, both from normal and reverse faults, and assess their response with respect to possible design implementations.

In this study, fundamental characteristics of earthquake fault rupture propagation have been examined both in dry sand deposit through physical models in 1-g conditions in a laboratory scale of 1 /20, with particular concern on dip-slip fault (normal and reverse) and through numerical simulation of the exact same problem in prototype scale. The 1-g models investigated the pattern of rupture propagation according to fault type (dip-slip normal or reverse), the displacement of underlying fault and the relative position of the caisson foundation to the outcrop in the free field. The numerical simulation and analysis of fault rupture propagation through sand deposit including the caisson foundation is then performed using the finite element method, after the model is adequately validated against the experimental data.

## ΠΕΡΙΛΗΨΗ

Η διάρρηξη ενός σειсмоγόνου ρήγματος στην επιφάνεια της γης και οι επιπτώσεις της στις υπερκείμενες κατασκευές είναι ένα πρόβλημα διαχρονικό, το οποίο έχει τα τελευταία χρόνια ασχολήσει την παγκόσμια επιστημονική κοινότητα, και εξαιτίας πολυ σημαντικών σεισμών. Χαρακτηριστικό παράδειγμα αποτελεί ο καταστροφικός σεισμός  $M_w 7.4$  της Νικομήδειας (Τουρκία) που προκλήθηκε από επαν-ενεργοποίηση του ρήγματος οριζόντιας διάτμησης της Βόρειας Ανατολίας, προξενώντας κανονική διάρρηξη στην λεκάνη διεφελκυσμού του Gölcük. Αποτέλεσμα αυτής της διάρρηξης ήταν επιφανειακοί αναβαθμοί που έφτασαν σε ύψος σχεδόν τα 2.5 m.

Όσον αφορά τον αντισεισμικό σχεδιασμό έμφαση δίνεται μόνο στην δυναμική απόκριση των κατασκευών και των θεμελίων τους. Σε μεγάλο βαθμό αυτό οφείλεται και στις μεγάλες αβεβαιότητες αναφορικά με την ύπαρξη, την ενεργότητα και την επικινδυνότητα των καταγεγραμμένων και μη ρηγματων στις περιοχές ενδιαφέροντος.

Παρ' όλα ταυτα η επιφανειακή εκδήλωση της διάρρηξης μπορεί να διασχίσει αρκετές κατασκευές. Όπως αναμένεται και επιβεβαιώνεται απο τα ιστορικά περιστατικά , πολλές από αυτές είτε καταρρέουν ή υφίστανται σοβαρές βλάβες. Έκπληξη προκαλεί το γεγονός ότι αρκετές από αυτές είναι σε θέση να επιζήσουν της διαρρηξέως πρακτικά ανέπαφες. Σε ορισμένες μάλιστα περιπτώσεις η διαδρομή της επιφανειακής διάρρηξης δείχνει να εκτρέπεται προκειμένου να "αποφύγει" την κατασκευή. Σε άλλες περιπτώσεις οι βλάβες είναι σημαντικές, παρότι η διάρρηξη εμφανίζεται να έχει "απορροφηθεί" από τις επιφανειακές εδαφικές στρώσεις, μη δημιουργώντας καν ευδιάκριτο αναβαθμό.

Οι παλαιότερες αντιλήψεις περί πλήρους απαγόρευσης δομήσεως "στην άμεση γειτονία ενεργού ρήγματος" όχι μόνον θα ήταν καταδικαστικές, αλλά κρίνονται και ως αποδεδειγμένως υπερβολικές, και συχνά ανεφάρμοστες. Ο Νέος Ελληνικός Αντισεισμικός Κανονισμός (ΕΑΚ-2000), ορθώς δέν απαγορεύει την δόμηση στην



γειτονία ενεργού ρήγματος, προδιαγράφει όμως την ανάγκη εκπόνησης ειδικής σεισμικής- γεωλογικής – γεωτεχνικής – στατικής μελέτης.

Η δυσκαμψία της θεμελίωσης φαίνεται ότι επηρέασε σημαντικά την απόκριση των διερευνηθέντων δομητικών συστημάτων. Είναι ενδιαφέρον ότι διερευνηθείσες κατασκευές ήταν θεμελιωμένες με ποικιλία τύπων θεμελίωσης, από μεμονωμένα πέδιλα, έως δύσκαμπτες κιβωτιοειδείς θεμελιώσεις, και πασσαλο-θεμελιώσεις.

Όπως, λοιπόν γίνεται αντιληπτό, είναι επιτακτική ανάγκη να υπάρχει μεθοδολογία υπολογισμού και σχεδιασμού έναντι επιφανειακής διάρρηξης ρήγματος. Στην παρούσα μεταπτυχιακή εργασία εξετάζεται η περίπτωση κανονικής και ανάστροφης διάρρηξης σε ελεύθερο πεδίο αμμώδους εδαφικού σχηματισμού και στη συνέχεια η αλληλεπίδραση της διάρρηξης με εγκιβωτισμένο θεμέλιο (φρέαρ), ως τυπική περίπτωση θεμελίου βάθρου γέφυρας. Η διερεύνηση λαμβάνει χώρα με τη χρήση τόσο εργαστηριακής – νέα συσκευή προσομοίωσης επιφανειακής διάρρηξης κανονικού και ανάστροφου ρήγματος του εργαστηρίου Εδαφομηχανικής της Σχολής Πολιτικών Μηχανικών ΕΜΠ – όσο και αριθμητικής προσομοίωσης με τη χρήση κώδικα τρισδιάστατων πεπερασμένων στοιχείων. Γίνεται συγκριτικά αξιολόγηση των αποτελεσμάτων τόσο μεταξύ τους όσο και με β'σση τη βιβλιογραφία.





<b>ABSTRACT</b> .....	5
<b>CHAPTER 1 - INTRODUCTION</b>	
1.1 Problem Definition.....	12
1.2 Objectives and Tools.....	14
1.3 Organization.....	15
<b>CHAPTER 2 - LITERATURE REVIEW</b>	
2.1 Introduction .....	18
2.2 General Features.....	19
2.3 Remarks on Case Histories and Experiments.....	19
2.3 Fault Rupture–Soil–Foundation–Structure Interaction (FR-SFSI).....	23
Figures.....	27
<b>CHAPTER 3 - EXPERIMENTAL SIMULATION</b>	
3.1 Introduction - Scope.....	42
3.2 Investigated Problem.....	42
3.3 Experimental Layout .....	43
3.3.1 Fault Rupture Box.....	43
3.3.2 Model Scale – Symmetry Conditions.....	44
3.3.3 Experimental Model.....	44
3.3.4 Instrumentation.....	45
3.4 Model Preparation.....	46
Figures.....	49
<b>CHAPTER 4 - NUMERICAL SIMULATION</b>	
4.1 Introduction.....	60
4.2 Finite Element Model.....	65
4.3 Constitutive Modeling of Soil Behavior.....	67
4.4 Soil – Caisson Interface.....	70
Figures.....	71
<b>CHAPTER 5 – NORMAL FAULTING</b>	
5.1 Introduction.....	80
5.2 Free Field.....	81
5.3 Normal Fault Rupture – Caisson Interaction.....	83
5.3.1 Test 1 - NFR: $s/b=0.16$ .....	83
5.3.2 Test 1 - NFR: $s/b=0.38$ .....	86
5.3.3 Test 1 - NFR: $s/b=0.80$ .....	89

5.4 Summary.....91  
Figures.....95

**CHAPTER 6 – REVERSE FAULTING**

6.1 Introduction.....122  
6.2 Free Field.....122  
6.3 Reverse Fault Rupture – Caisson Interaction.....126  
    6.3.1 Test 1 - RFR:  $s/B = 0.66$ .....127  
    6.3.2 Test 1 - RFR:  $s/B = -0.04$ .....129  
    6.3.3 Test 1 - RFR:  $s/B = -0.96$ .....132  
6.4 Summary .....135  
Figures.....139

**CHAPTER 7 – CONCLUSION**

7.1 Conclusions.....166  
7.2 Limitations.....167  
7.3 Future Work.....168

**LIST OF REFERENCES.....172**

**APPENDIX A.....177**

**APPENDIX B.....193**

# ***Chapter 1***

## **INTRODUCTION**

## 1.1 Problem Definition in General

In many large magnitude earthquakes the causative fault propagates all the way up through the soil and interacts with surface structures. And although, earthquake engineering research and practice has (over the last four decades) emphasized the dynamic response of soil and structural systems to ground oscillations, this should not be taken to imply, that large ground displacements are not a problem, nor that that problem is unsolvable.

Subterranean fault rupture has been responsible for many recorded instances of building damage during past earthquakes. Differential displacement in the ground can cause shearing in overlying structures and can leave structures in an unsupported condition. Structures that are adequately designed against dynamic loads during severe earthquakes may still have a significant risk of failure due to excessive permanent ground deformations induced by surface fault breakage. To take this problem into account, most seismic design codes prevent the erection of structures across, or in the immediate vicinity of seismically active faults. As a reference we recall the *Alquist-Priolo earthquake fault zoning Act* that regulates since 1972 in California for the mitigation of hazard of surface faulting to structures and the clause 4.1.2 of the recently approved Part 5 of Eurocode 8 [2].

It should be noted that, a reliable mapping of seismically active faults can be achieved with a reasonable degree of accuracy, at least for the purpose at hand, only in few regions; in most tectonic environments, such as Southern Europe, characterized by diffuse seismicity and seismic faults of relatively small dimensions (up to few tens of km), even the

identification of the causative fault of some of the major seismic events may lead seismologists to conflicting viewpoints.

In addition to the uncertainty and inherent lack of completeness related to the mapping activity, it should be remarked that secondary ruptures can also contribute significantly to the overall damage due to excessive ground displacements, and these ruptures can be located at relatively large distances from the main trace of the fault rupture. Several interesting cases are reported for the 1999 Chi-Chi Taiwan earthquake [4] and for the Landers 1992 earthquake in California, where most ground breakages occurred in an area some tens of meters wide, but extensional cracks were also observed several hundreds of meters from the main trace. Moreover, for long structures, such as bridges, tunnels, pipelines, and embankments, which often cannot avoid crossing such geologic faults, comes the question of the design criteria used. Last but not least, the presence of a structure on top of the soil deposit may further modify the path of the rupture, as the latter propagates from the base rock to the ground surface. Depending on the rigidity of the foundation and the weight of the structure, even a complete diversion of the fault path before it outcrops may take place.

Therefore, at least in the cases of important facilities and infrastructure, engineering approaches are needed to limit the damage potential, as they are particularly susceptible in experiencing surface fault rupture hazards.

The understanding of the interplay that develops between the propagating fault rupture, the deforming soil under the structure, and the differentially displacing foundation is the aim of this dissertation



thesis, as this interplay is of profound significance for the performance of the structure. More specifically, the objective of is to investigate the interaction of rigid embedded foundations, caissons, with dip slip fault imposed deformations, both from normal and reverse faults, and assess their response with respect to possible design implementations.

## 1.2 Objectives and Tools

The phenomenon, named hereafter “Fault-Rupture–Soil–Foundation–Structure Interaction”, (FR–SFSI) has focused some attention, but has not been studied extensively. The prime objective of this research is to explore the role of this interaction, the further investigation into the characteristics of earthquake fault rupture propagation and the behavior of caisson foundations subject to fault displacements for enhancement of earthquake-resistant performance of infrastructures.

Comprehensive study of the field observations (e.g. Youd et al., 2000; Anastasopoulos and Gazetas, 2007 a; Faccioli et al., 2008) and associated numerical analyses (Anastasopoulos and Gazetas, 2007b) showed the importance of the interplay that takes place between the propagating fault rupture, the soil, the foundation and the supported structure. A significant amount of numerical and experimental work has been done over the interaction of dip-slip fault rupture with surface and caisson foundations (e.g. Anastasopoulos et al., 2008; Bransby et al., 2008, Loli et al, 2009).

In this study, fundamental characteristics of earthquake fault rupture propagation through dry sand deposit have been first examined through physical models in 1-g conditions with particular concern on dip-slip fault. The 1-g models investigated the pattern of rupture propagation according to fault type (dip-slip normal or reverse), the displacement of underlying fault and the relative position of the caisson foundation to the outcrop in the free field. The results are compared with similar experiments that took place in the centrifuge apparatus of the University of Dundee. The numerical analysis of fault rupture propagation through sand deposit has been then performed using the finite element method.

Although, testing, even in scale testing, of the physical problems is an excellent tool to achieve qualitative and quantitative results, nevertheless it is accompanied by time and other testing related limitations that do not allow for the conduction of an adequate number of tests to support a full study. Therefore, numerical modeling of the problem is necessary and thus deployed and the experimental results are used to validate the numerical methodology.

### **1.3 Organization**

The dissertation consists of seven chapters. After the first introductory chapter, in Chapter 2 the main features of earthquake fault rupture are described and the idea of fault rupture–soil–foundation–structure interaction is once again introduced. Moreover, reference of the existing research findings over the propagation of dip slip fault rupture through soil and its interaction with surface and deep foundation is made. Chapter 3 presents the basic features of the physical

model and the methods used during the set up, the conduction and the result processing of 1-g experiments. The numerical method is outlined in Chapter 4. The FE model is described and emphasis is put on modeling details regarding the constitutive soil behavior and the soil – foundation interfaces.

The experimental tests and results for reverse and normal faults are presented in the following two chapters. They compared with the results of equivalent numerical simulations and qualitatively with the similar results in the centrifuge. The different mechanisms controlling the behavior of the soil – foundation system are identified and discussed in each case. Moreover, the effectiveness of the numerical methodology to capture the various modes of response is evaluated.

Finally, Chapter 7 presents the main conclusions drawn from the present study and gives recommendations for future work.

# *Chapter 2*

## LITERATURE REVIEW

## 2.1 Introduction

The problem of fault rupture propagation through soil has been assessed, through: (a) real case histories, (b) small-scale experiments, and (c) numerical analyses.

The assessment of real case histories, although being the most reliable method since it is only monitoring what happens in nature, is usually of relatively high uncertainty due to the complexity of the actual soil conditions (especially in depth). The conduction of small-scale experiment undoubtedly has certain advantages: the parameters of the problem are well defined and relatively controllable. However, since soil behavior is largely dependent on the geostatic stresses, in order to realistically simulate the reality centrifuge modeling must be applied, which is costly and time consuming. Another experimental option is the 1-g modeling, which is less costly and its main disadvantage is that it cannot simulate the real scale stress conditions. Numerical modeling possesses some great advantages. The available computing power allows for the conduction of large series of parametric simulations in less time and with lower cost than small-scale experiments. Furthermore, both the soil-related parameters and the loading are fully controllable, not posing problems of repeatability, as in the case of small-scale tests. On the other hand, the realism of the numerical simulation is dependent on the applied constitutive models and consequently the simulation is subjected to inaccuracies linked to the inherent problems of the constitutive model used – especially for the case of simpler models. Moreover, before the numerical simulation is used it has to be adequately validated to real case histories or experimental data.

## 2.2 General Features

Earthquakes are generated from spasmodic relative movements of tectonic plates which occur on new or pre-existing offsets in the geologic structure of the crust, known as faults. The orientation of a fault plane is described by its strike and dip (Kramer, 1996). The *strike of the fault* is the horizontal line produced by the intersection of the fault plane and the horizontal plane. The angle between these two planes is the *dip angle*. Categorized according to the relative movement between the displaced bedrock, there are two main types of faults:

- *strike-slip*, when the movement is occurring in the direction of the slip and
- *dip-slip*, when the movement is occurring in the direction of the dip.

The dip-slip faults are further classified into reverse type or normal type, depending on the faulting direction. The non-displaced side of the soil layer is denoted as the *foot wall* whereas the deforming – moving block is called *hanging wall*.

This thesis focuses on the propagation of dip-slip, both normal and reverse faults in the free field as well as its effect on foundations.

## 2.3 Remarks on the Case Histories and Experiments

### 2.3.1 Case Histories

Beginning with normal faulting, in **Figure 2.1** the most commonly observed propagation patterns are summarized [Bray, 1990]. In all real case histories the footwall remains practically intact with most of the

deformation being concentrated within the hanging wall. The dip of the rupture tends to increase while propagating to the surface. Firstly, it increases at the soil-bedrock interface due to refraction while passing from a rigid to a more compliant medium (soil). Next, the dip tends to increase further, with the rupture path bending over the hanging wall. High plasticity ductile soil layers, bending over the hanging wall, tend to spread the deformation to wider zones, without any fault scarp being actually formed. At the location of maximum bending tensile cracking is usually observed. When the fault dip is small and the soil layer relatively stiff and brittle, secondary antithetic ruptures and gravity grabens may form. Finally, the relative displacement along the slip line tends to decrease with the rupture propagating to the surface.

In thrust faulting, as in the case of normal, most of the deformation is accumulated over the hanging wall, with the footwall being relatively un-deformed. While the fault rupture is propagating to the surface, generally the dip tends to decrease significantly with the hanging wall bending over the footwall. However, some times (i.e. Montague Island, Alaska earthquake, 1964) the dip of the thrust fault was observed to increase while emerging at the surface. This difference in the response can be attributed to the prevailing tectonic compression, combined with a small initial dip (Prucha, Graham & Nickelsen, 1965). **Figure 2.2** presents typical propagation patterns for reverse faulting, according to Bray [1990]. As in the case of normal faulting, ductile earth materials, bending over the slip line, are found to spread the deformation over wider zones. At the maximum bending location, tensile cracking as well as secondary normal-type faulting are observed. The relative

displacement along the slip line is always inferior at the surface, compared to the initial bedrock displacement.

### 2.3.2 Experimental Research

It must be noted that, the experimental research in the field of fault rupture propagation is quite significant. Taking into account the complex nature of the rupturing process the results at least from the qualitative comparison are remarkable.

Generally, the experiments agree that the dip tends to increase in the case of normal faulting and decrease in reverse, while the rupture propagates to the surface. In normal faulting, as observed in the reality, the dip first increases at the soilbedrock interface due to refraction, and then bending over the hanging wall it is augmented further. The main parameters influencing the rupturing process are: (i) the fault dip, (ii) the strength parameters of the medium (friction angle  $\varphi$  and cohesion  $c$ ), (iii) the kinematic parameters (dilation angle  $\psi$ ), and (iv) the initial stress state (geostatic stresses,  $K_0$ ). Although there have been many studies in the field nevertheless no full agreement regarding the relative importance of these parameters has been reached.

Lade & Cole [1984], conducting small-scale experiments in sand, concluded that the rupturing process is mainly dependent on the kinematic parameters, with the *friction angle* being discharged of any importance. Moreover, that the effect of the rate of the soil volume change – expressed by the dilation angle – on the location and the shape of the failure surfaces formed within the soil mass is determinate. The



comparison of the behavior for dense and loose granular materials indicated that there are significant differences between the shapes of the failure surfaces formed in each case (**Figure 2.3 - 2.4**). The failure planes were more distinct and sharp in the case of dense sands. In the case of loose sand layers a larger base displacement was required to propagate the base fault to the surface and the rupture was more widespread bending over the hanging wall. Additionally, normal faults propagate to the surface more quickly, thus for smaller values of base fault throw, compared to reverse faults. The effect of *dilation* is dependent mainly on the kinematics, and this is why it was shown to play an important role, despite the inaccuracies of the modeling procedure.

It is important to remark that, at very low stress levels even an insignificant cohesion of  $1 - 2 \text{ kPa}$  can become the governing factor near the model surface. Since the cohesion is not largely dependent on the stress field, small-scale ( $1-g$ ) testing of cohesive materials can be held to be more realistic, provided that the basic scaling rules are followed ( $Su^{\text{experiment}} = Su^{\text{reality}} \times n$ , where  $n = \text{specimen scale}$ ; for example: if the model is  $1/100$  of the reality, and  $Su^{\text{reality}} = 100 \text{ kPa}$ , then  $Su^{\text{experiment}} = 100 \times 1/100 = 1 \text{ kPa}$ ). Furthermore, according to Bray's experiments [Bray, 1990, Bray et al, 1994] the *failure strain* of the clay is an equivalently decisive parameter. Belousov's experiments [Belousov, 1961] for the simulation of rupture propagation through rock by the use of clayey materials can also be hold as realistic.

The problems of small-scale testing can be solved by the use of centrifuge. Until recently, only a few researchers have performed such

experiments for the simulation of dip-slip faulting (Roth, Scott, and Austin, 1981; Branby et al, 2008; Loli et al 2009). Their results qualitatively generally agree with those of small-scale experiments.

## **2.4 Fault Rupture - Soil – Foundation -Structure Interaction (FR-SFSI)**

The 1999 earthquakes in Turkey and Taiwan, offering a variety of case histories with different deformation patterns, **Figure 2.5**, structures subjected to large tectonic displacements, have supplied the engineering community with some of the most important case histories, concerning the fault rupture propagation through the soil that interacts with foundation and the structure [(a) the Mw 7.4 Kocaeli (August 17) 1999 earthquake in Turkey, (b) the Mw 7.1 Düzce-Bolu (November 12) 1999 earthquake in Turkey, (c) the Mw 7.6 Chi–Chi (September 21) 1999 earthquake in Taiwan]. While several structures were severely damaged or even collapsed, there were numerous examples of satisfactory performance. Even more astonishingly, in specific cases the surface fault rupture was effectively diverted due to the presence of a structure. There have been conducted many studies in order to gain deeper insight into the main mechanisms controlling this fascinating interplay, named Fault-Rupture–Soil–Foundation–Structure Interaction (FR-SFSI), by Anastasopoulos and Gazetas, 2007a and 2007b.

Comprehensive field evidence analyses of FR-SFSI (see Faccioli et al., 2008 and Anastasopoulos & Gazetas, 2007a) highlighted the key role of the foundation type in determining the response of the system and lead to the following conclusions:

- The rigidity and continuity of the foundation appears to be one of the crucial factors affecting the response.

- Structures on rigid and continuous foundations demonstrate a quite satisfactory performance as their rigid body response saves them from structural failure, resulting in only some unavoidable rotation. On the other hand, flexible foundation systems tend to follow the applied deformations leading to substantial stressing and structural damage, **Figure 2.6 – 2.9**.

- Increasing the foundation vertical load (structural weight) improves the performance. Heavier foundations tend to effectively divert the rupture and “avoid” the applied loading. Moreover, as opposed to lighter structures, they don’t suffer significant loss of contact with the underlying soil.

- Piled foundations also force the structure to follow the imposed deformation and their performance appears to be less favourable than that of rigid mat foundations.

The characteristic conclusion from the analysis of the fault rupture–foundation interplay is that it is feasible to design structures able to survive fault rupture that reaches the ground surface. To this end, Gazetas et al, 2008, have proposed a set of practical recommendations, referring to the proper design of structures in the vicinity of active faults. Furthermore, Anastasopoulos et al., (2008c) proposed a general methodology for the design of bridges against large tectonic deformations, taking into account the fault rupture soil pier foundation interaction. Complementary work has been completed in order to add on to the knowledge gained so far; by Bransby et al. (2008a, 2008b) with a series of centrifuge experiments to model dip-slip fault rupture

propagation through sand and its interaction with strip foundations; by Anastasopoulos et al, 2008a; 2008b, who derived semi-analytical relationships to estimate the fault rupture path and the vertical surface displacement profile for the case of fault rupturing in the free field. Moreover, this methodology can capture the dominating FR-SFSI phenomena (fault rupture diversion and modification of displacement profile due to the foundation) achieving satisfactory agreement with the aforementioned experiment results, as has been shown by the work of Loli et al, 2009. All the previous mentioned studies lead to the conclusion that the foundation response varies significantly depending on its position relatively to the fault outcrop position.



# Figures

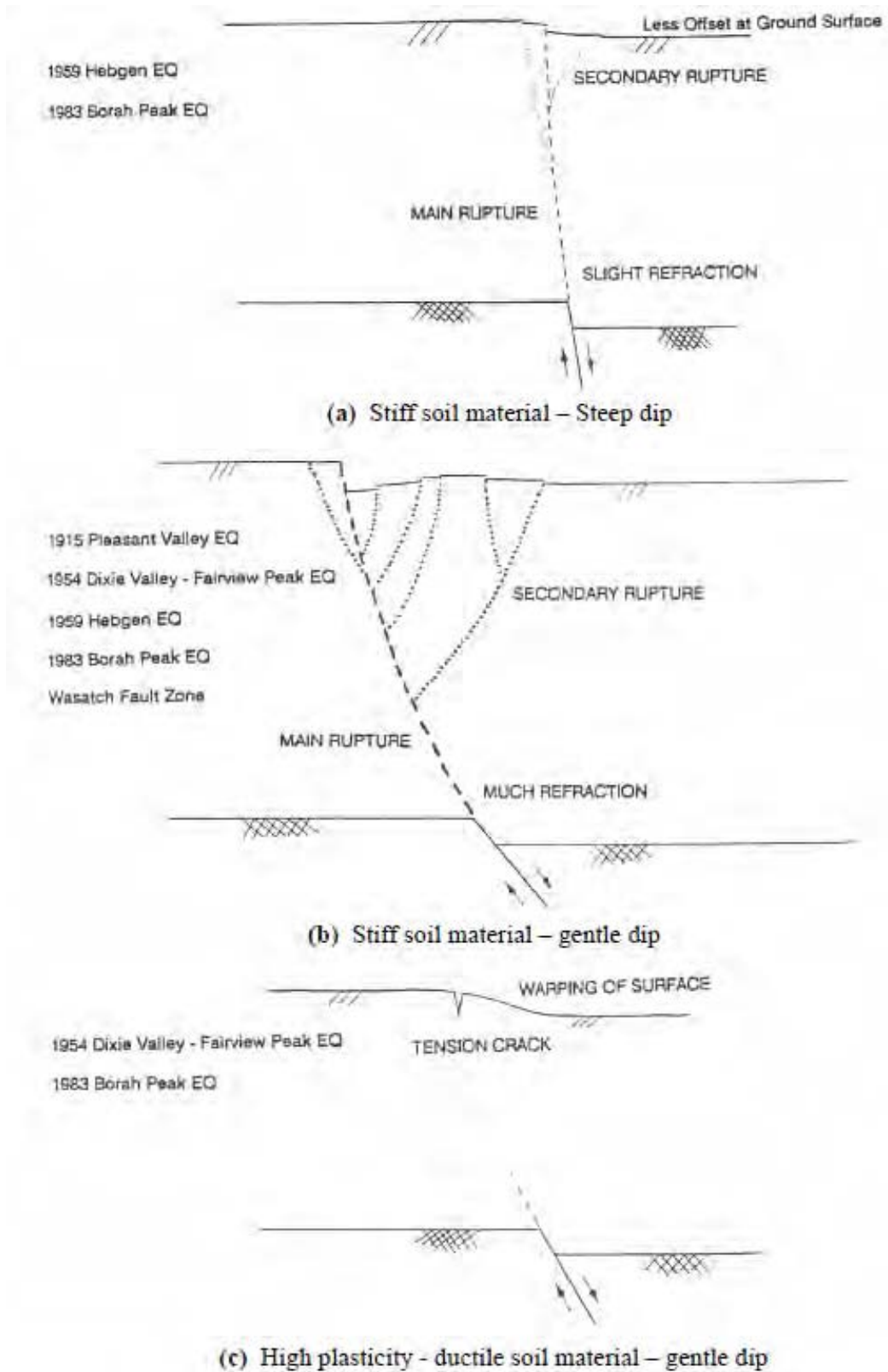


**Figure 2.1** Normal Fault Rupture Propagation

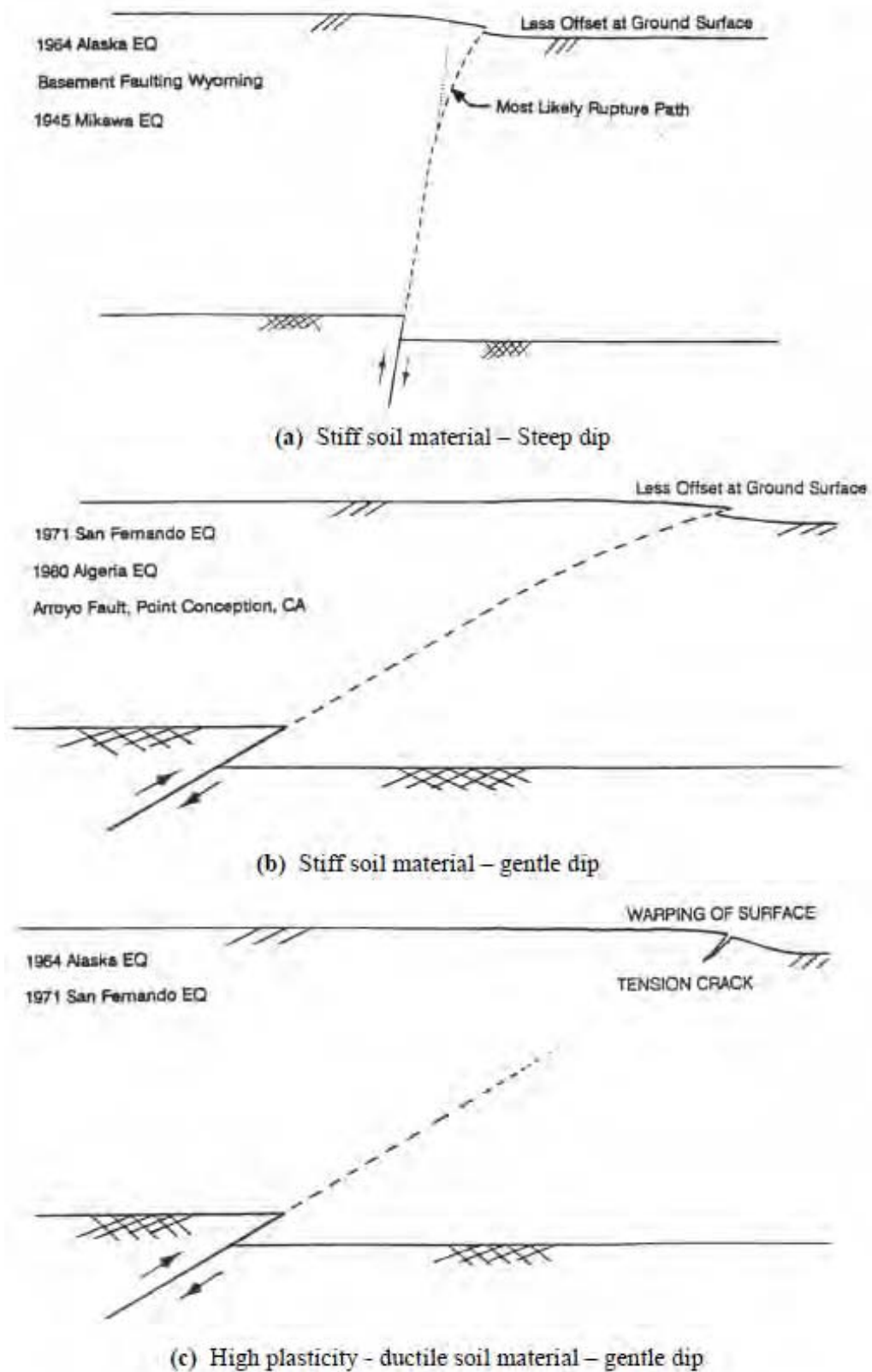


**Figure 2.2** Reverse Fault Rupture Propagation



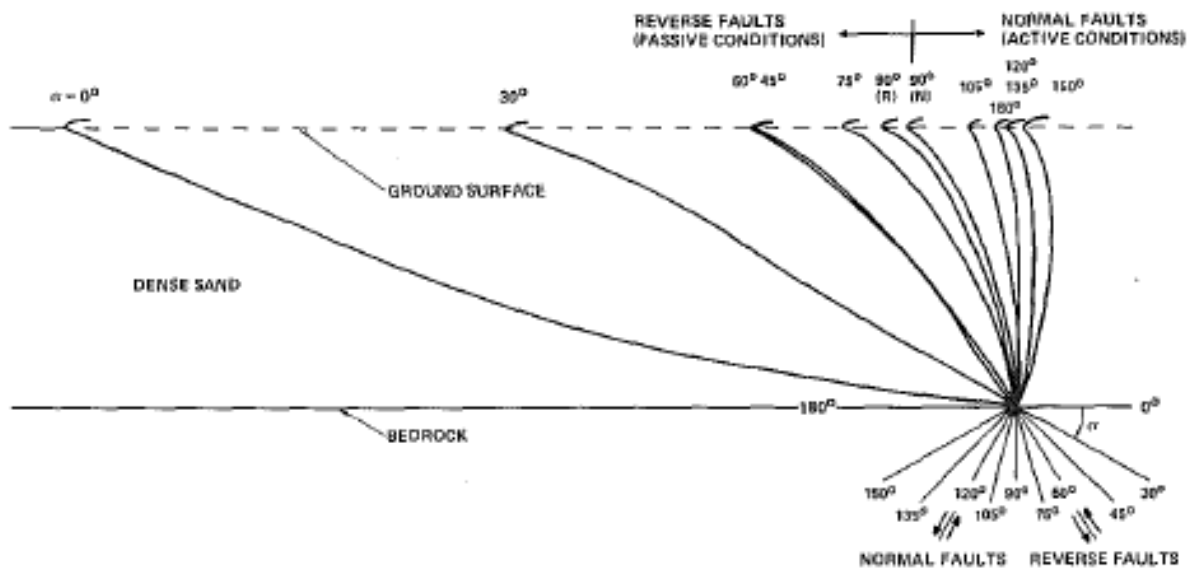


**Figure 2.3** Line drawings of Primary Failure Surfaces observed in tests on dense sand.

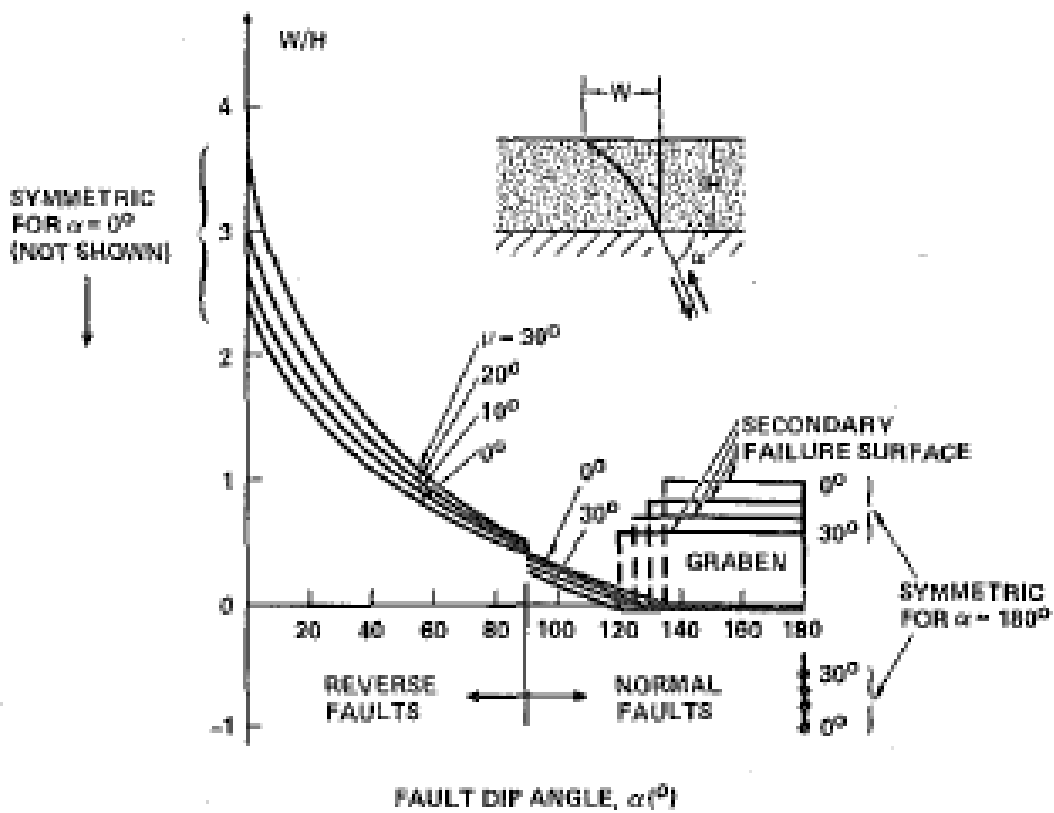


**Figure 2.4** Variation of  $W/H$  for location of surface rupture in alluvium over Dip-Slip Fault as function of Dip Angle,  $\alpha$ , and angle of dilation,  $\nu$ .

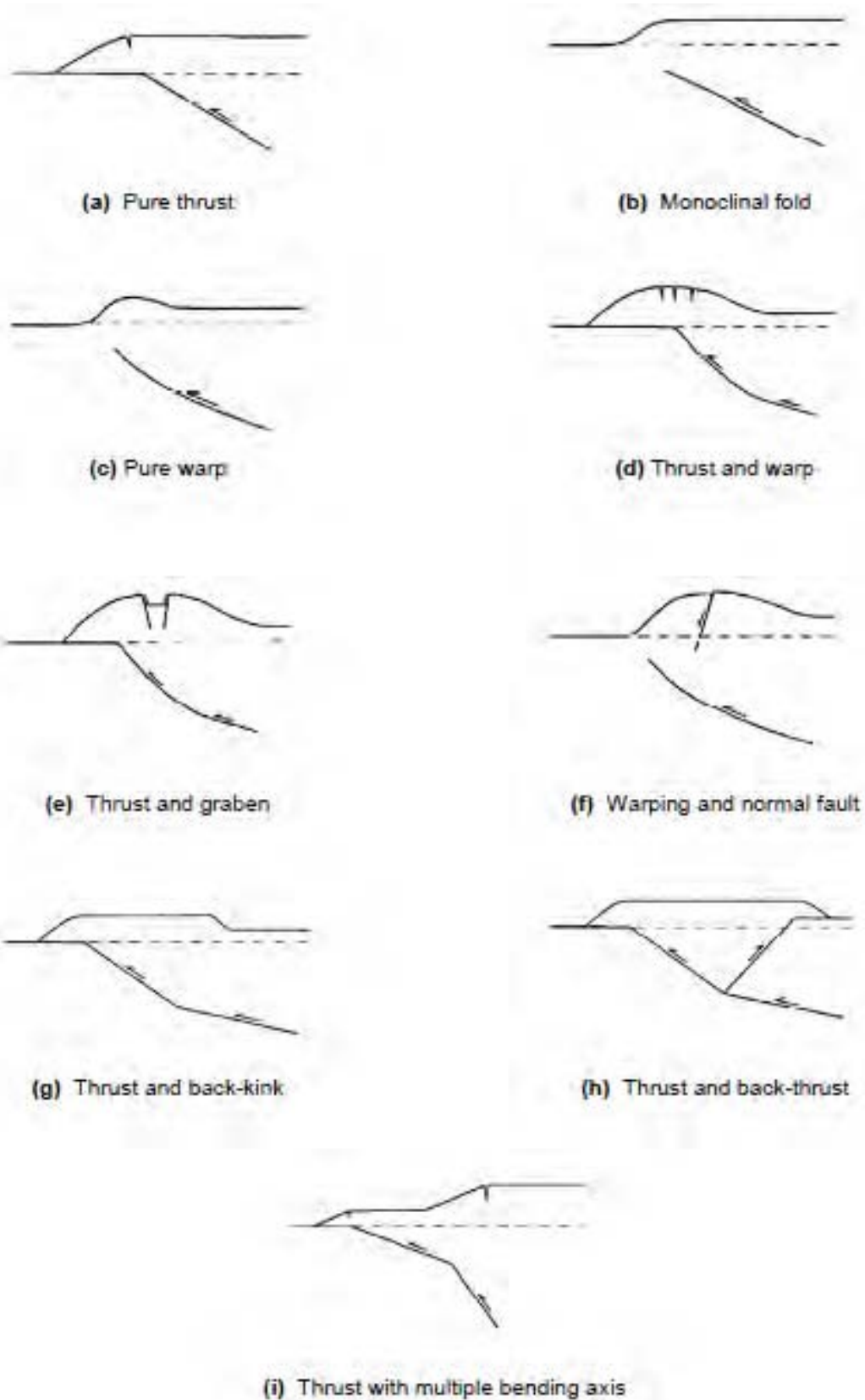


**Figure 2.5** Chi-Chi, Taiwan 1999 : The 9 different deformation patterns of the ground surface due to the reverse fault propagation.

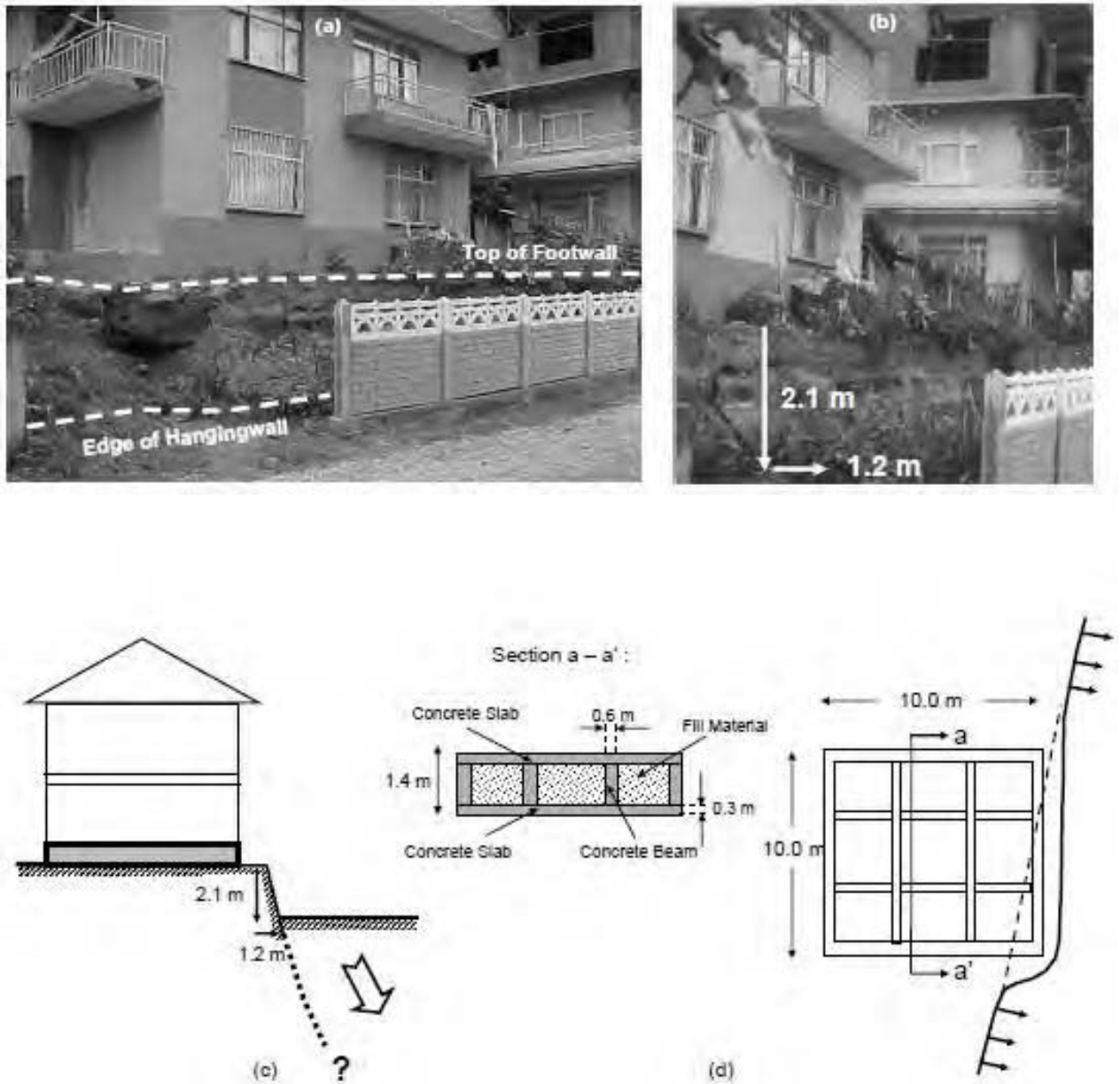


**Figure 2.6** The 1999 Kocaeli Earthquake, Building with two stories plus attic, **Minor Damage** : (a) photo of the building, showing the fault scarp right next to the building, (b) photo of the rupture scarp in front of the building, showing the measured vertical and horizontal displacement, (c) schematic cross-section of the building, and (d) plan view of its box type foundation along with a representation of the **diverted rupture**.

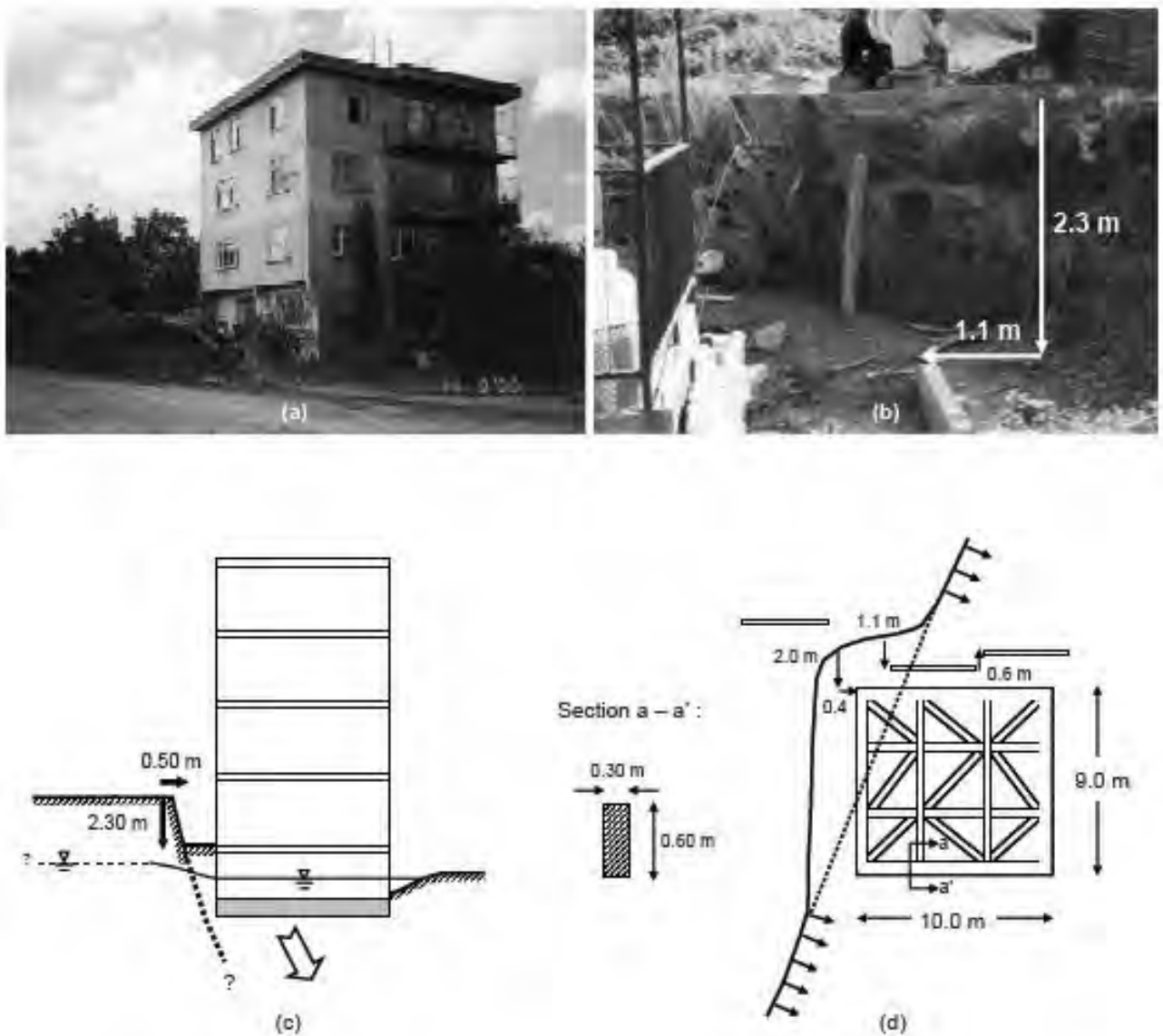


**Figure 2.7** The 1999 Kocaeli Earthquake, Building with four stories plus basement, **Minor Damage** : (a) photograph of the building showing the **fault trace being diverted**, (b) photograph showing the vertical displacement reaching 2.3 m, along with a horizontal component of 1.1 m measured on the torn apart fence of the building, (c) cross-section of the building, and (d) plan view of the foundation (box-type foundation with cross tie beams), along with the horizontal displacements measured around the building.

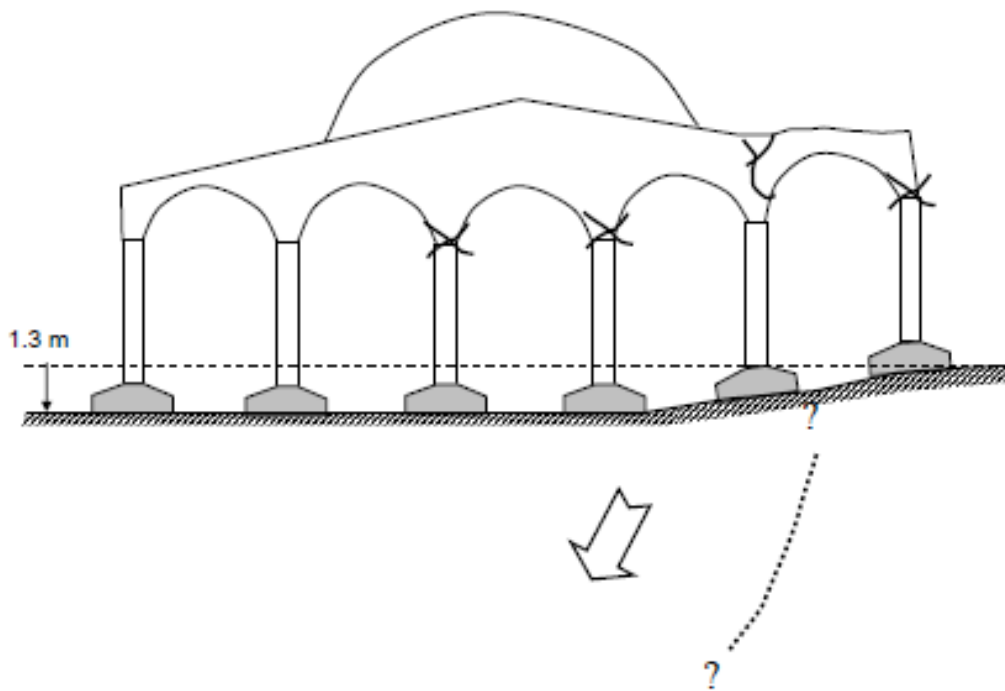


**Figure 2.8** The 1999 Kocaeli Earthquake, Mosque, **Collapse** : (a) photograph of the Mosque showing the differential settlement of the unscarped ground surface and the distress of its superstructure, and (b) sketch of its cross section and foundation (separate footings).

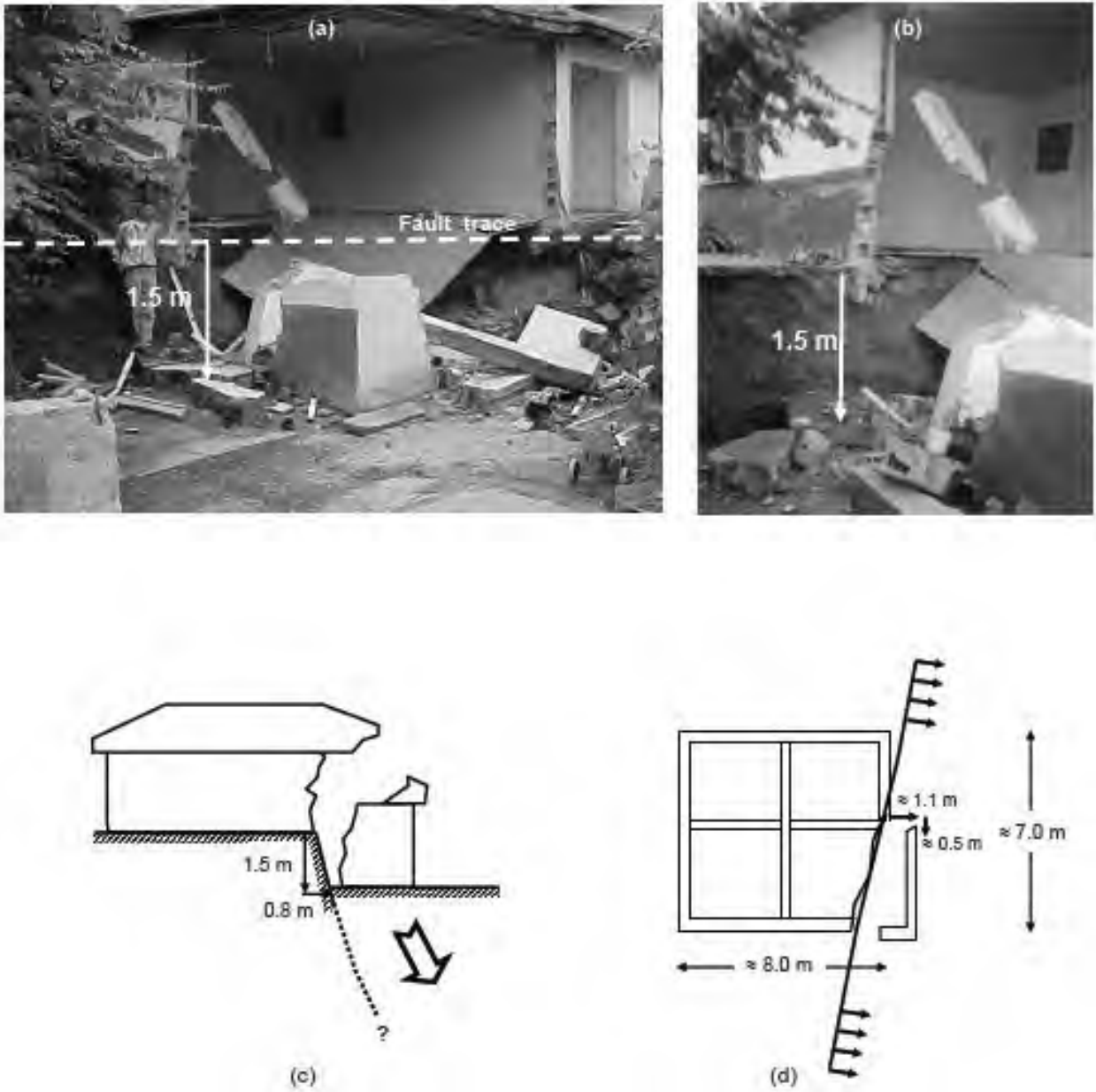


**Figure 2.9** The 1999 Kocaeli Earthquake, Building 2, single story, **Partial Collapse**: (a) photo of the fault trace passing through the building, (b) photo of the rupture–produced cross section of the building (cinder-block walls directly founded on the ground), (c) schematic cross-section of the building, and (d) plan view of the foundation and the measured offset displacements.

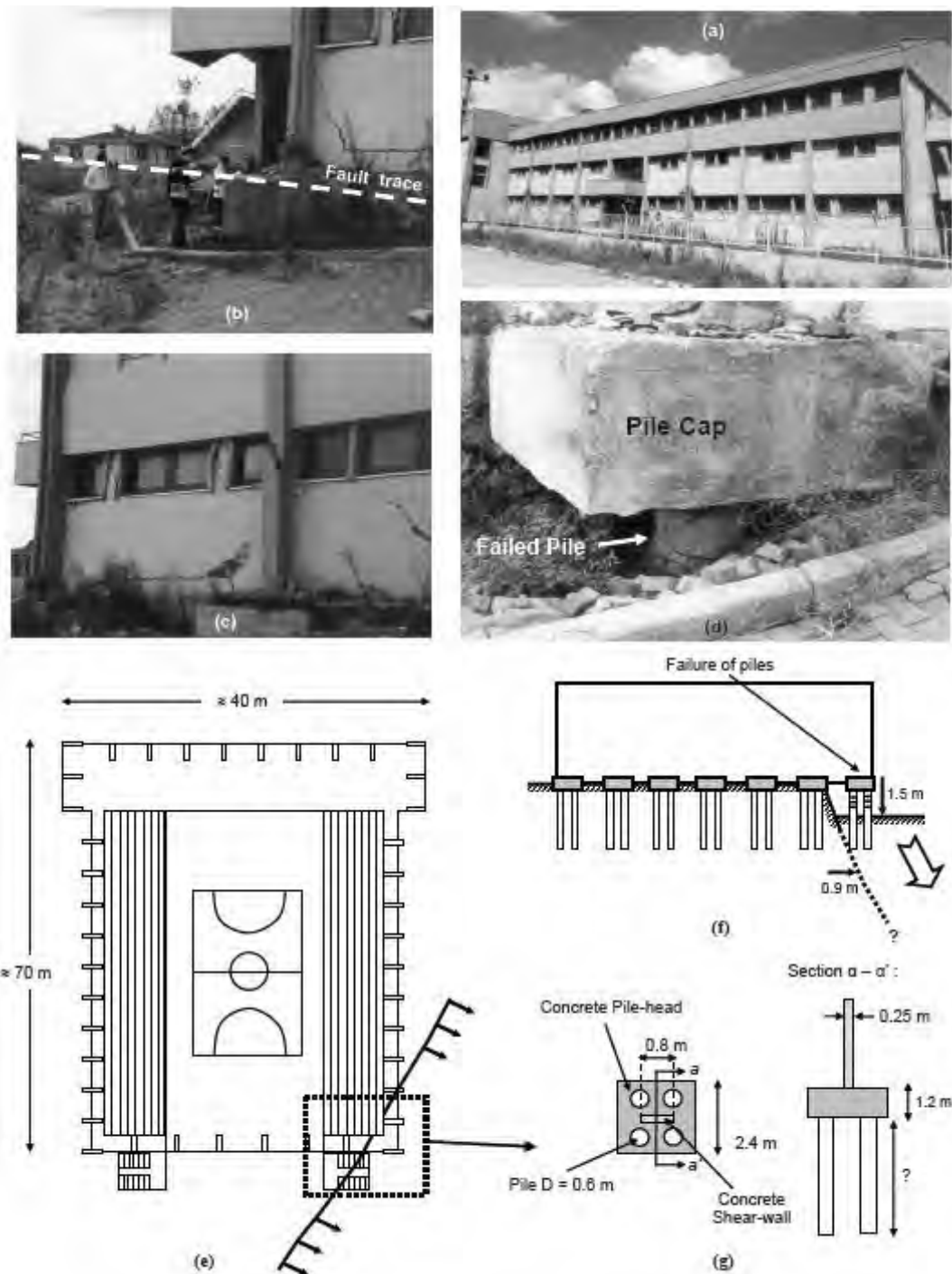


**Figure 2.10** Basketball Court, **Severe Local Damage** : (a) panoramic photo of the building, (b) photo of the building's corner crossed by the fault trace, (c) shear damage due to the **imposed differential settlement**, (d) **tensile failure of the piled foundation**, (e) schematic plan view of the building, along with the rupture trace, (f) cross-section showing the fault displacement and the damage to the (pulled-own) piles, and (g) detail of the foundation.





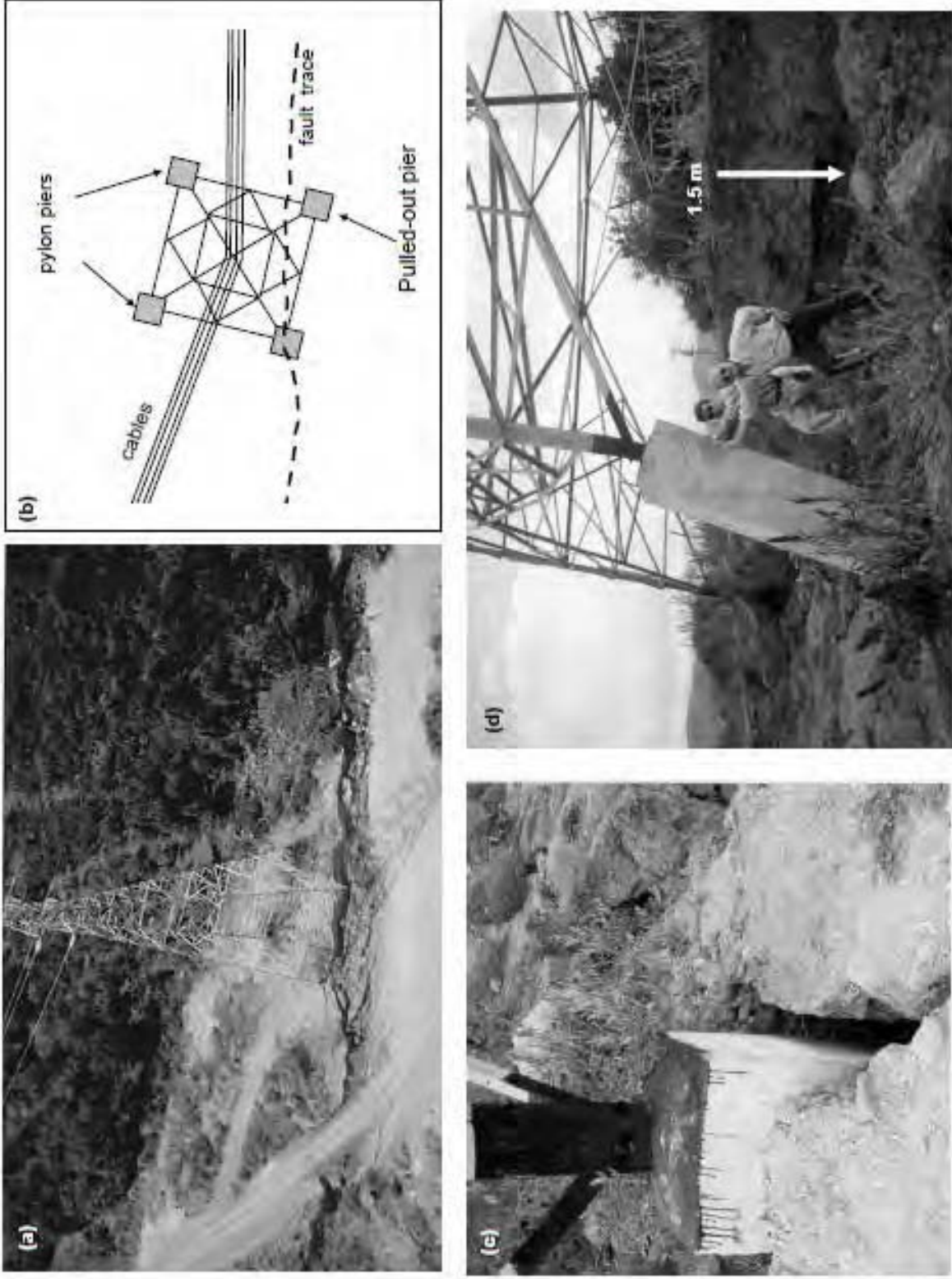


**Figure 2.11** High Voltage Pylon, Minor Damage : (a) aerial photo, (b) plan-view sketch of the pylon and the fault rupture, (c) photo of the directly-hit left foundation pier, and (d) photo of the pulled-out right foundation, relatively small, pier.



# *Chapter 3*

## **EXPERIMENTAL SIMULATION**

### 3.1 Introduction – Scope

The experimental aspect of the thesis aims at investigating the response of the caisson foundation under fault rupture loading and explores the mechanisms of FRSFS. The supporting soil is a layer of dense, dry sand and the analysis focused on the effect of the foundation position relative to the fault, which according to previous studies is a determinative parameter for the response of the system (Bransby et al., 2008 a and 2008b, Loli et al 2009). The main geometric features and the boundary conditions of the studied problem are schematically illustrated in **Figure 3.1**. The figure also defines the x-y-z coordinate system adopted hereafter. The modeling details, the apparatus and the techniques used during the preparation of the model, the conduction of the tests and the analysis of results are described in the following sections.

The experimental series consists of 5 experiments in the Fault Rupture Box of the Laboratory of Soil Mechanics, 2 of which represent normal fault rupture and the 3 reverse fault rupture. The experiments investigated the following parameters: (a) the type of the fault rupture (normal or reverse) and (b) the position of the caisson foundation relative to the position of the fault rupture on the bedrock and the free field.

It should be noted that the first two experiments are those with the free field cases, both normal and reverse, in order to be able to use the results in order to choose the position of the foundation, via the parameter  $s$ , and at the same time pursue a class A prediction, with respect to the expected results according to the theory and other researcher that have conducted similar work.

### 3.2 Investigated Problem

We consider the problem that is depicted graphically in **Figure 3.1**. A reinforced concrete caisson foundation of dimensions 10 x 5 x 5 m (H x W x D) is fully embedded in a stratum of dense sand of 15 m depth. The relative density of the soil stratum is approximately 80% and the weight of the caisson foundation is 20 MN.

The bedrock is subjected to movement due to fault rupture (normal or reverse) with a vertical component  $h$  at an angle of  $45^\circ$ , while the position of the fault  $s$  is defined parametrically relatively to the zone of the fault rupture at the foundation level for the case of the free field. The displacements of the caisson,  $\Delta_x$ ,  $\Delta_z$ , and  $\vartheta$ , and complementary the displacements of the soil mass are recorded during the experiment. The number of the totally examined different cases are 8, and are synopsised in **Table 1**.

### 3.3 Experimental Layout

#### 3.3.1 Fault Rupture Box

For the fulfilment of these experiments the Fault Rupture Box (FRB) of the LSM is utilized, which allows experimental simulation of fault rupture propagation through soil and fault rupture – soil - foundation and the superstructure interaction.

In general, the apparatus is custom designed to simulate quasi-static fault rupture propagation through soil and its interaction with foundation–structure systems. The apparatus is equipped with a fixed and a movable part. The latter can move downwards or upwards to simulate normal or reverse faulting (dip – slip). The angle of rupture is adjustable from 45 to 90 degrees. At the two sides of the box, special transparent barriers are installed to allow observation of soil deformations. With a total length of 3 m and total height of 1.6 m, the apparatus is capable of rupturing soil specimens of up to 1 m in height, at a maximum imposed fault “offset” of +/-200 mm (i.e., 20% of deformation).

More specifically, the apparatus, **Figure 2**, consists of: (a) a box of internal dimensions 2.60 x 1.10 x 1.00 m (length x width x height), within which the soil layering takes place, (b) an electromechanical piston imposing the displacement (for this experimental series - at a constant angle of  $45^\circ$ ) and (c) a data acquisition system for measuring and controlling the imposed displacement.

The apparatus is composed by two parts, the stable and the movable part, in which the desired displacement is enforced. The movable part is moving upwards or

downwards for the simulation of the normal or reverse fault rupture respectively. In general the angle of the dip can be set from  $45^{\circ}$  to  $90^{\circ}$ . In the present experimental series the angle chosen is fixed at  $45^{\circ}$ . In the larger sides of the box there have been placed specific transparent barriers that are composed of Plexiglas from the outside, for rigidity and durability, and glass from the inside, in order to achieve minimum friction during the displacement of the movable part and simultaneously avoid the scratching of the Plexiglas. Utilising these barriers both the observation and the monitoring of the evolution of the fault rupture propagation, the deformation of the soil mass and the displacement of the caisson foundation is achieved.

The maximum ability of the electromechanical piston (screw jack type) to impose the displacement is 5 tones and the maximum imposed displacement is 20 cm.

### 3.3.2 Model Scale – Symmetry Conditions

Taking into account the capacity of the Fault Rupture Box (FRB) the chosen model scale is 1:20, which is considered appropriate for the 1-g simulation of the prototype problem, while the choice of dimension and materials used in the model is based upon the rules of similarity [Gibson, 1997].

Given the out of plane rigidity of the FRB borders, they are considered as symmetry planes, thus half the caisson foundation, that is tangent to the barrier is simulated. Thus, we have the opportunity to simultaneously investigate up to two cases during each experiment (either only the free filed case, a combination of the free filed at the one side and one position of the caisson foundation at the other side of the apparatus or two different cases for the position of the caisson foundation), imposed to the same fault rupture loading, normal or reverse.

### 3.3.3 Experimental Model

The experimental model of the rigid caisson, **Figure 3**, is made of steel of density  $8 \text{ Mg/m}^3$ . The choice of the material regarded as suitable to achieve simultaneously the desired similarity between model and prototype scale both in terms of

dimensions (N) and in terms of weight ( $N^3$ ). The dimensions of the half model are 0.5 x 0.25 x 0.125 m (H x W x D). The caisson's upper boundary is set at the level of the surface and it is placed with its base horizontally.

The backfill consisted of dry “Longstone” sand, a very fine and uniform quartz sand with  $D_{50} = 0.15$  mm and uniformity coefficient  $D_{60}/D_{10} = 1.42$ , industrially produced with adequate quality control. The grain size distribution curve for the sand is shown in **Figure 4**. The void ratios at the loosest and densest state were measured in the laboratory. Following the procedure described by Kolbuszewski [1948]  $e_{max} = 0.995$ , while  $e_{min} = 0.614$ , and  $G_s = 2.64$ .

Direct shear tests were carried out to define peak and post-peak strength characteristics of the sand. Tests were performed on medium loose  $D_r = 45 \pm 0.02\%$  and dense specimens  $D_r = 80 \pm 0.07\%$  and for a normal stress range from 13 kPa (due to the weight of the top cap only) to 300 kPa. The low normal stress is more representative of the stress level prevailing in the shaking table tests. Loose specimens were prepared by raining the sand into the box while dense specimens were obtained by tapping the box after raining. The loose specimens have shown critical state behavior. The angle of shearing resistance appears to depend strongly on stress level and for stresses higher than 120 kPa  $\varphi' \approx 32^\circ$ , while for stress levels lower than 100 kPa  $\varphi'$  increases up to  $47^\circ$  at normal stress  $\sigma = 13$  kPa. For the dense specimens the angle of shearing resistance increases to  $\varphi' \approx 35^\circ$  for higher stress levels and to  $51^\circ$  at the lowest normal stress. These values drop after displacement of 6 mm to post-peak values similar to the peak strength of the medium-loose specimens, indicating an angle of dilation  $\psi \approx 6^\circ$ .

#### 3.3.4 Instrumentation

The instrumented observation – monitoring of the experiments takes place by the use of instruments outside of the model. More specifically:

- Digital cameras are used to take pictures of the model from a fixed position outside the fault rupture box, one at each side. Quite a few pictures

per test were taken at progressively increasing fault displacements. The photographic data were then analyzed using the Geo-PIV programme, written by White et al. [2003], to calculate caisson displacements and the shear strains developed within the soil.

- A row of 8 laser displacement transducers were set above the free surface of the model to monitor and record the progress of fault actuation during the test and to validate and complement the image analysis results, **Figure 5**. All the laser transducers are placed to be perpendicular to the axis of the model (and thus almost vertical). Moreover the row is assigned on a device that can move from one end of the model to the other in order to scan the surface of the model during each displacement increment, while retaining a constant height during each “scanning”. Due to this procedure it is possible to scan the surface and reproduce the digital regeneration of the deformed relief after each increment of equivalent fault rupture displacement  $h$ .
- The data from all the instruments are gathered through proper cables and saved in the record system of the Laboratory.

### 3.4 Model Preparation

Due to the fact that the FRB has adequate width it is possible to simultaneously investigate two cases during one experiment: the model of the caisson (half) is placed in the one transparent border of the device and the free field or a second caisson, but in a different position relative to the position of the fault rupture on the bedrock  $s$ , is investigated on the other transparent border. The relative distance between the two caissons is assumed adequate so as to avoid important interaction between them; this assumption is proven to be less accurate in some cases of the interaction between the caisson and the free field under reverse fault rupture. Nevertheless taking into account the diversion from the theoretically expected results and the limitations of the experimental procedure, the results are considered more than adequate to serve the purpose of the research aim.



The model preparation begins with the sand layering within the FRB. The sand layering is succeeded through an appropriate electronically controlled device of the Laboratory, with which it is possible to choose and audit the mechanical characteristics of the layered soil material, by specifying the density of the soil specimen, **Figure 6**. This procedure is cold sand pluviation.

To achieve the desired density during the pluviation procedure (in this experimental series 80%), every time before starting the procedure the height above the bottom, the aperture of the device and its velocity are defined. The choice of the suitable values of these three parameters of the pluviation device is in accordance with **Figure 6c**, which synopsizes the results of an experimental series to calibrate this particular device.

The layering of the sand takes place in layers of approximately 5.5 cm. At the end of each layer tangent to the transparent borders of the FRB painted blue sand is added, in order to create a pattern to capture and identify the propagation of the rupture through the soil, **Figure 7**. This allows for both the observation and monitoring of the phenomenon and enables the image analysis procedure that takes place after the experiment.

In the case of the free field simulation, the procedure is repeated until the total height of 75 cm, where 0 cm is set on the bottom of the FRB, which is equivalent in prototype scale with a sand deposit of 15 m.

In the case that a caisson is also placed in the model, the layering is repeated, as described above, until the height of 25cm from the “zero point”, 5 meters in prototype scale. This is the foundation level of the base of the caisson foundation. The caisson is very slowly and carefully placed vertically in the properly chosen position, utilizing a manual crane, capable of small and slow movements. Thus, the disturbance of the soil under the caisson is avoided. After the caisson is placed the pluviation procedure goes on as before until the total height of 75cm. To efface the influence of the presence of the caisson during the pluviation procedure, a special receptacle with the same plan dimensions as the caisson is placed upon each

caisson; thus the surplus sand is gathered, without actually affecting the density of the sand deposition.

After the model preparation the instrumentation takes place; the laser transducer raw and the digital cameras are set in the suitable position and the measurements for the completely undeformed model – initial conditions are recorded.

The fault rupture displacement is imposed in very small steps - increments, each of the order of 2 to 5mm vertical displacement. Following each increment of the displacement the “new” measurements are recorded and by the repetition of this procedure the evolution of the phenomenon, to the maximum of 4m in prototype scale, is monitored recorded and completed.

# Figures

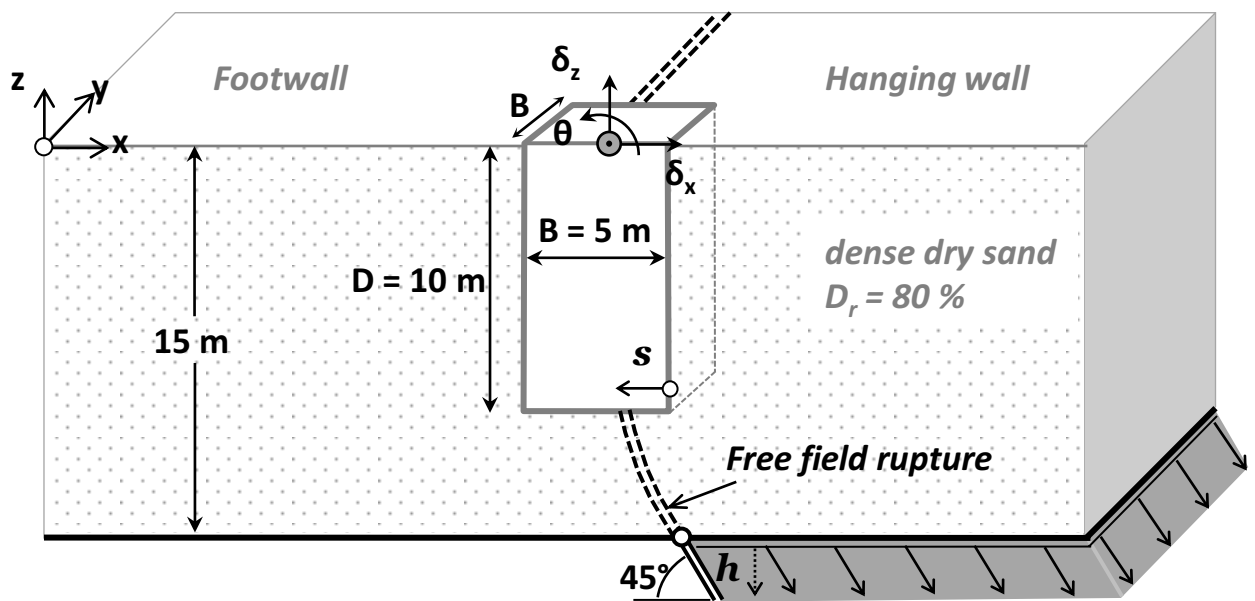
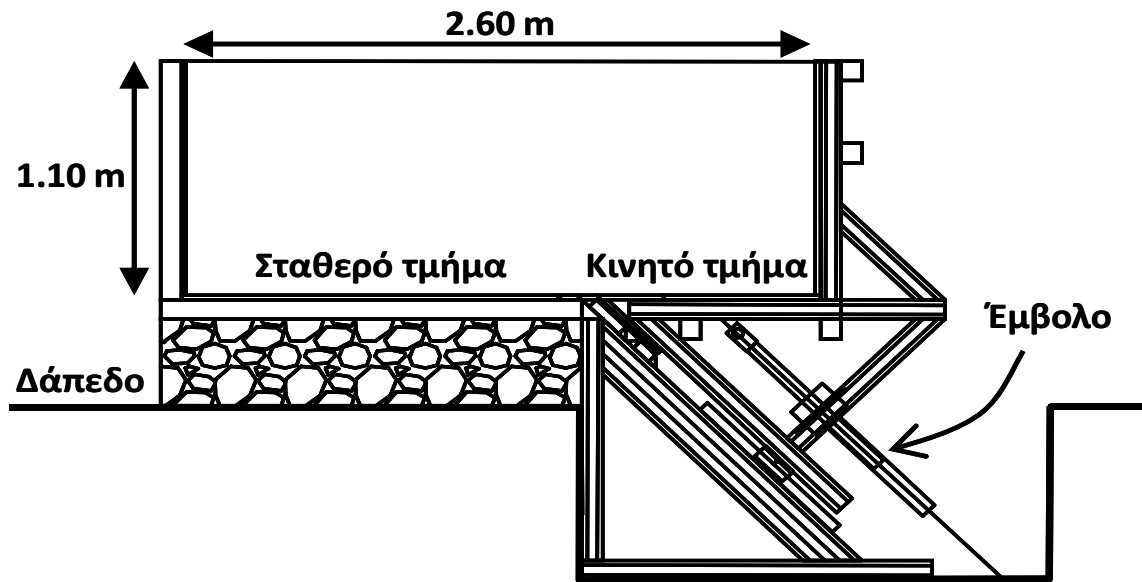


**Figure 3.1.** Schematic Representation – section cut of the examined problem and detection of the basic parameters and dimensions (prototype scale).



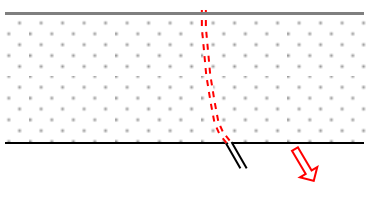
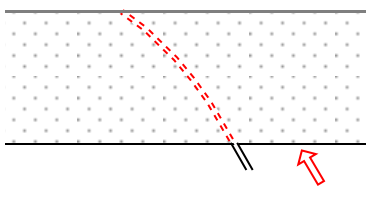
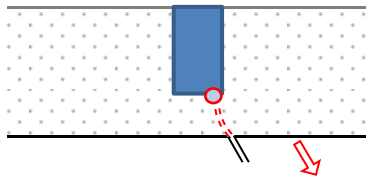
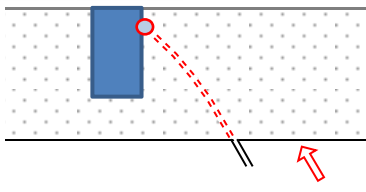
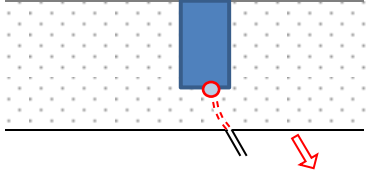
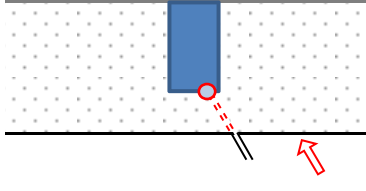
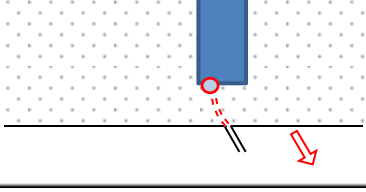
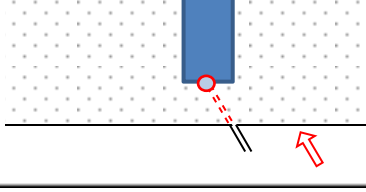
Ηλεκτρονικό Σύστημα  
Ελέγχου



Ηλεκτρομηχανικό Έμβολο  
(Screw-jack)

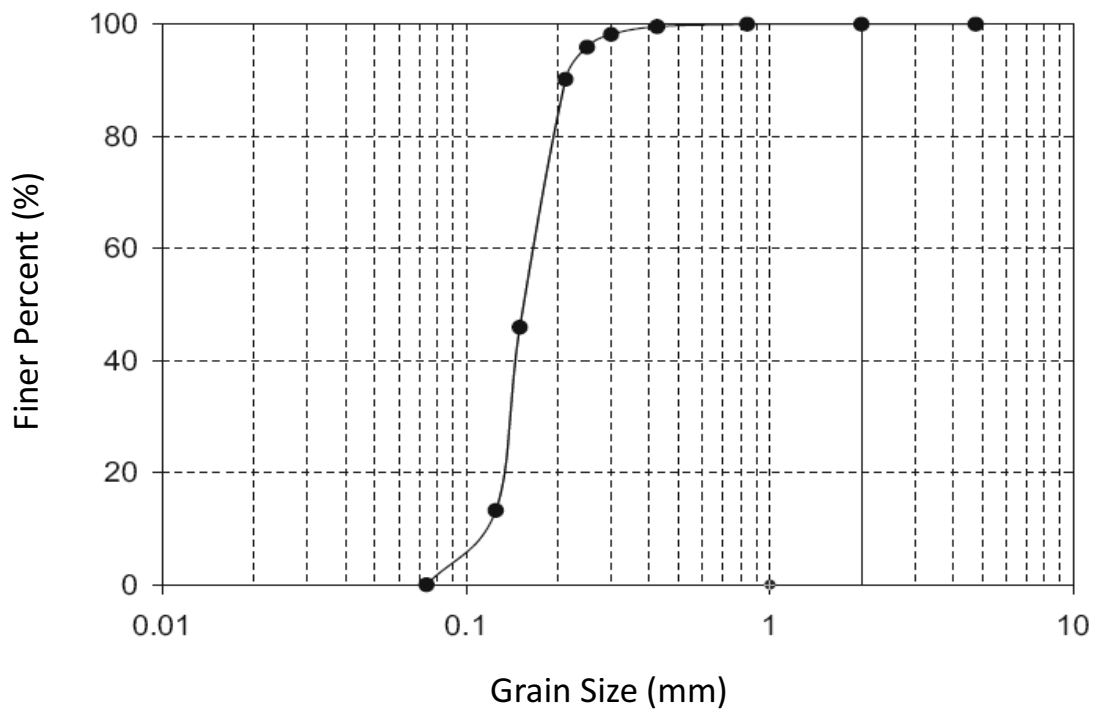
Figure 3.2. Fault rupture box apparatus and control system

**Table 3.1.** Synopsis of the different case examined

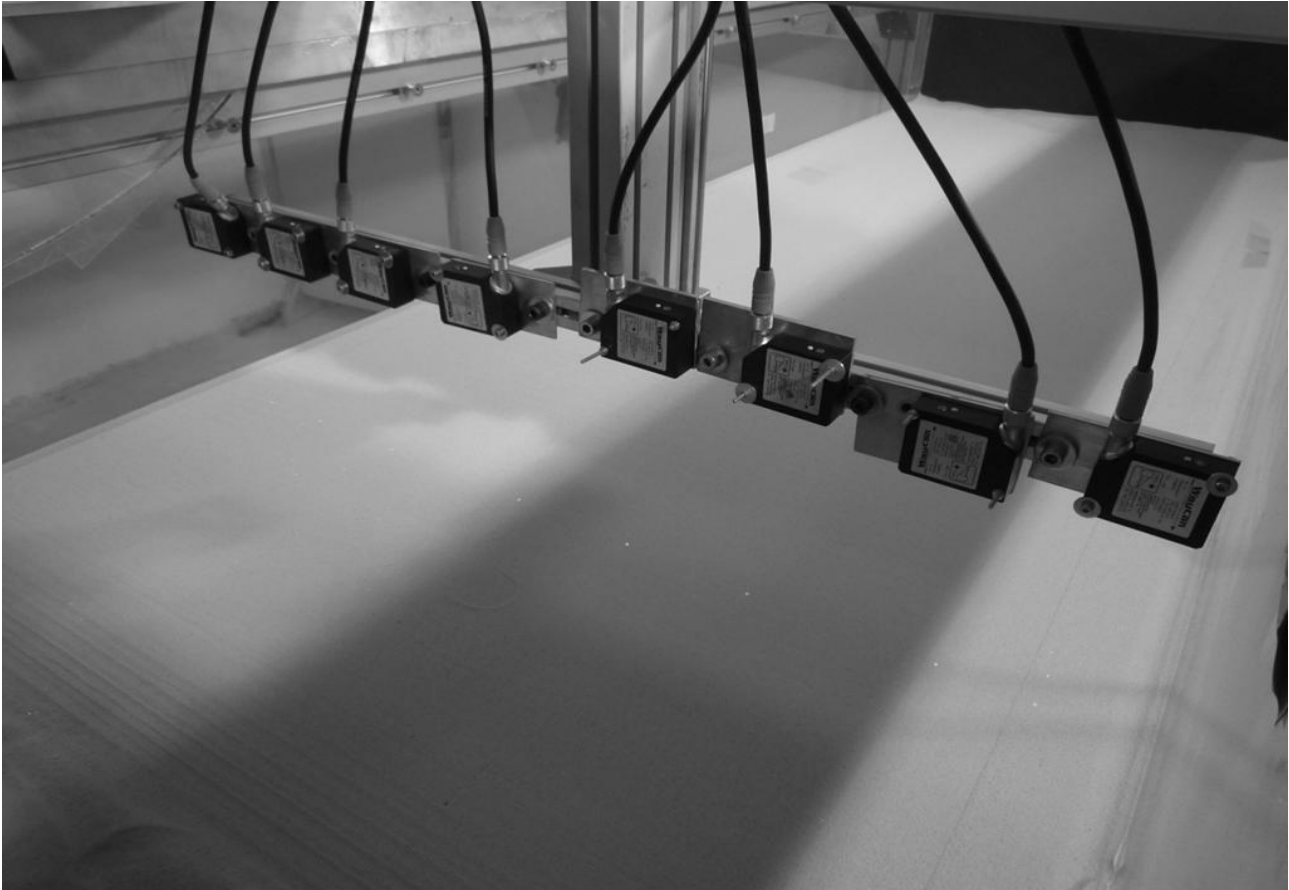
Normal Fault Rupture		Reverse Fault Rupture	
Free Field			
			
Fault Rupture – Soil – Caisson Foundation Interaction			
<p><math>s/B = 0.16</math></p> 	<p><math>s/B = - 0.96</math></p> 		
<p><math>s/B = 0.38</math></p> 	<p><math>s/B = -0.04</math></p> 		
<p><math>s/B = 0.80</math></p> 	<p><math>s/B = 0.66</math></p> 		



**Figure 3.3.** Photographs of the caisson model. The side tangent to the glass is covered with a pattern for image analysis purposes.

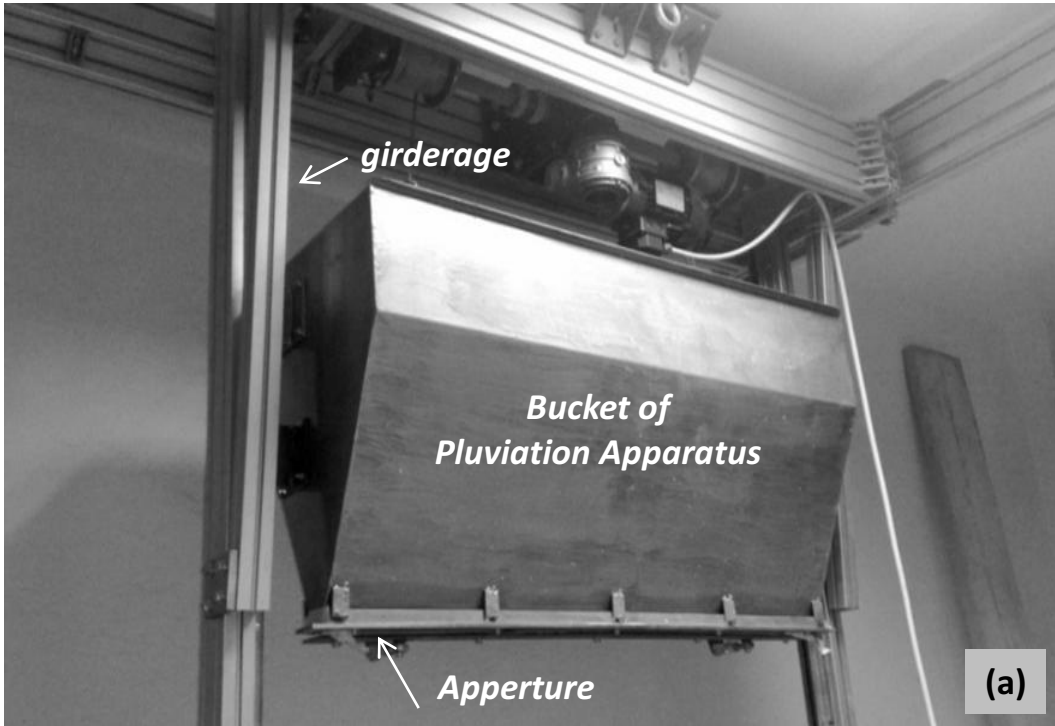


**Figure 3.4.** Grain size distribution curve for the Longstone sand



**Figure 3.5.** Row of laser displacement transducers, set above the surface of the model – scanning procedure of the model and record of the displacement and the deformation of the surface and the caisson foundation.





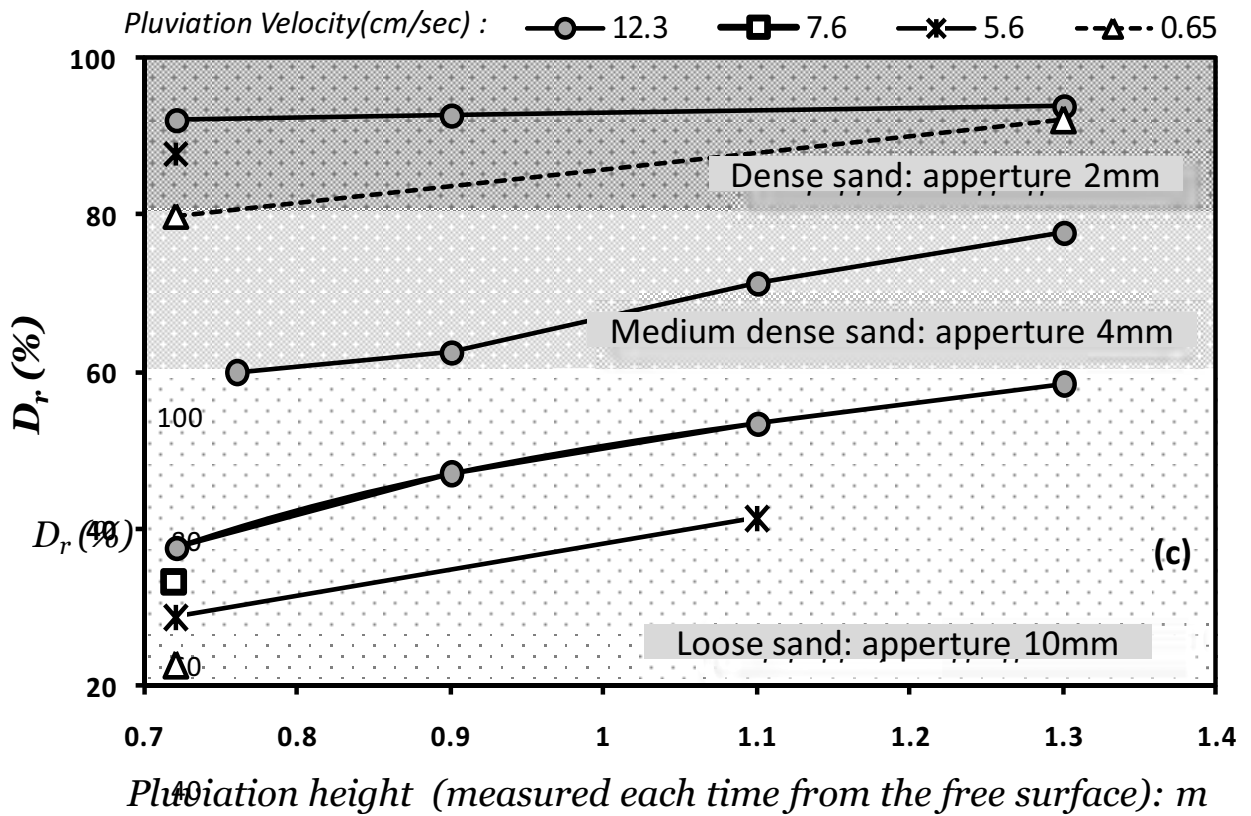


**Figure 3.6.** (a) The Pluviation Apparatus of the LSM-NTUA, (b) the Pluviation Apparatus over the Fault Rupture Box, (c) synopsis of the pluviation apparatus calibration results for the Longstone sand –  $D_r$  (%) vs. pluviation height and pluviation velocity and aperture size.

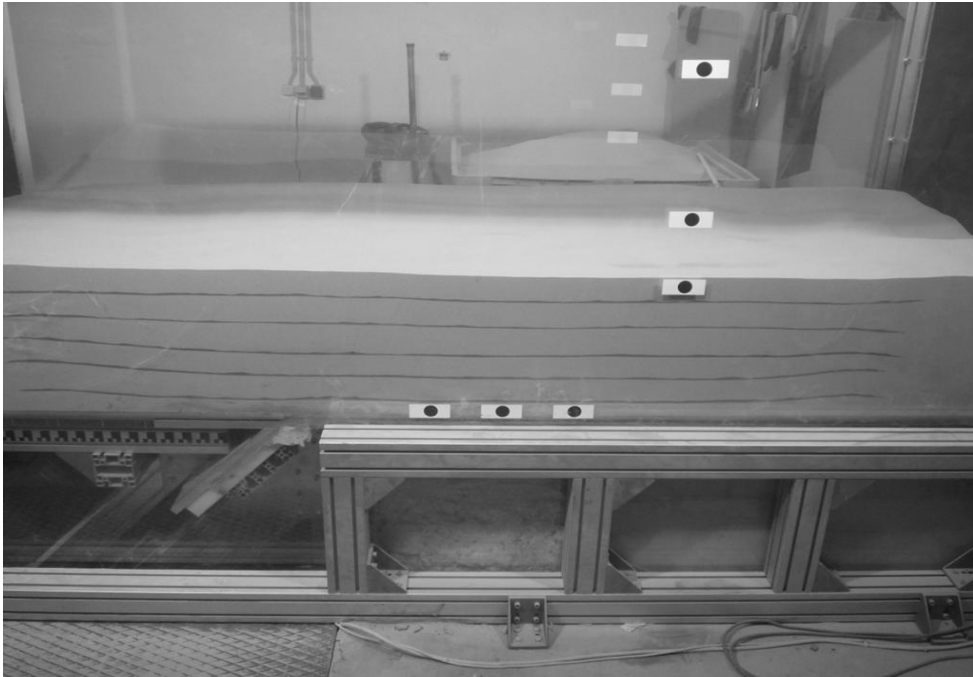


**Figure 3.7.** Model preparation – sand layers of approximately 5.5 cm and blue sand layers



# *Chapter 4*

## **NUMERICAL SIMULATION**

## 4.1 INTRODUCTION

The FEM and the FDM have been utilized for the simulation of fault rupture propagation. Different soil constitutive models have been applied; from the most simplified elastic-perfectly plastic to sophisticated ones.

Researchers have concluded that the simulation of fault-rupture propagation utilizing the FEM is dependent on the type and size of the elements (mesh), as well as the constitutive model (i.e. Scott, 1987). The results of Bray [Bray, 1990; Bray et al, 1994], as well as Duncan & Lefebvre's [1973] showed good agreement, between analysis and experiments, utilizing the FEM and applying a hyperbolic non-linear constitutive model. They proved that the FEM can give realistic results, provided that the soil itself is modeled realistically. Equally successful were the analyses performed by Roth, Sweet, and Goodman [1982] (for reverse faulting), and those by Loukidis & Bouckovalas [2001], utilizing the FDM. The first used an elastoplastic constitutive soil model with Drucker-Prager failure criterion combined with a bi-linear Mohr-Coulomb failure envelope. The later, considering soil softening to be decisive, applied an elastoplastic constitutive model with Mohr-Coulomb failure criterion and softening with the increase of plastic shear strain. The agreement of their results with experiments and real case histories strengthen their belief. In general, **all numerical studies agree on the bending of the rupture over the hanging wall and the dip increase for normal faulting, as well as the opposite (bending over the footwall, dip decrease) in the case of reverse faulting. Although there is no full agreement on the importance of the different parameters, the dilation**

**and the post-failure behavior of the soil are generally acknowledged as decisive.** The influence of the elastic parameters has not been explored since they are generally considered as unimportant. The strength parameters are largely debated: some researchers consider them to be practically unimportant (Lade & Cole, for example), while others tend to believe in their significance (i.e. Loukidis & Boukovalas). According to Bray, the failure strain of the soil material is, perhaps, the most prevailing parameter. **Almost all researchers tend to agree that softer – ductile soil materials tend to widespread the deformation in wider zones, while stiffer – brittle soils tend to localize the deformation in a single distinct rupture.** In the case of normal faulting, the normalized fault displacement to propagate the rupture to the surface ranges from 1% to 30%, depending on the medium and the method of analysis. In general, values in the range of 1% - 6% are considered to be more realistic. Bray, as well as Loukidis & Boukovalas, agrees that increasing  $K_0$  tends to delay rupture propagation and increase the bending over the hanging wall. Moreover, increasing the dilation leads to increasing the dip angle. **Finally, according to Loukidis & Boukovalas only when the dip is smaller than  $45^\circ + \psi/2$  does an antithetic secondary rupture and a gravity graben form, something which agrees with Lade & Cole's experimental results. Increasing the dilation, the width of the graben is decreased.**

### *Cohesionless Soil Materials*

*Walters & Thomas* [1982] conducted small-scale experiments to simulate reverse fault rupture propagation through *cohesionless soil*

materials. These experiments were used to validate a sophisticated non-linear incremental constitutive model - the Drucker-Prager failure criterion, along with a non-associated flow rule, incorporating softening capabilities. **When using an associated flow rule, the material continues dilating even after failure. Contrarily, experiments have shown that the dilation angle  $\psi$  is effectively reduced after failure.** They conducted analyses both using an associated flow rule as well as non-associated alternative. As depicted in **Figure 1**, while the numerical simulation managed to capture the initial propagation path correctly in both cases, the secondary vertically propagating slip line could be reproduced only with the use of the advanced non-associated flow rule. In all cases, a normalized bedrock displacement,  $h/H$ , of only *0.008%* was necessary to propagate the rupture to the surface, not in accordance with their experimental results according to which the required  $h/H$  was in the order of *1.25%*.

*Roth, Sweet, and Goodman [1982]* utilized their centrifuge experiment data [Roth, Scott, and Austin, 1981] to validate a *FD* numerical model. They made use of the *FD* code *SAGE*, utilizing a non-linear constitutive law applying the Drucker-Prager failure criterion and a non-associated flow rule. According to experimental testing the simulated soil material - *Ottawa sand* - did not exhibit significant softening after failure, and therefore the applied constitutive law was considered to be adequate. **Figure 2** depicts characteristics results of the numerical analyses. **The rupture is more localized in dense sand than in loose, while the outcropping dip is steeper for the loose sand.** The increase of the dilation angle  $\psi$  leads to a decrease of the dip as the rupture propagates to the surface. The bending of the rupture near the surface was more



pronounced for the case of fine-grained silty sand. According to the researchers, the comparison between analysis and experiments was encouraging. They concluded that the strength parameters were the ones controlling the behavior, and not the elastic ones.

### *Cohesive Soil Materials*

*Bray* [Bray, 1990 ; Bray et al, 1994] also utilized the FEM to simulate normal and reverse faulting, at different dip angles through *cohesive soil* materials of different depth, using the finite element Code *SSCOMP* [Boulanger et al, 1991]. He applied **Duncan's hyperbolic constitutive model** [Duncan et al, 1980] which, despite its simplicity, is capable of controlling the failure strain of the clayey soil material. Something, which has been shown to play an important role in fault rupture propagation, according to Bray's experiments. He supposed that both the undrained shear strength  $S_u$  and the deformation modulus  $E$  were linearly increasing with depth. The failure strain was taken from the experiments, ranging from 6.5% to 15%. According to Bray, a ratio of model **width to height in the range of 4:1** was adequate for **the boundaries not to affect the results**. Typical results of his analyses are presented in **Figure 3**. Initially, normal faults were propagating with no change in dip. By increasing the imposed displacement, the rupture was bending over the hanging wall, increasing its dip. **According to Bray, at the first deformation stages the strength parameters play the most important role, while for higher displacements the kinematic parameters are prevalent.**

*Loukidis & Bouckovalas* [2001] performed a series of numerical analyses using the *FD* code FLAC. Considering the soil behavior after failure to be decisive, they applied an elastoplastic constitutive model with Mohr-Coulomb failure criterion and softening with the increase of plastic shear strain. Both the friction  $\varphi$  and the dilation  $\psi$  were decreased with the increase of plastic shear strain. The friction angle  $\varphi$  was reduced to a residual strength value for plastic strain of 5%, while  $\psi$  was nullified for the same plastic strain level. Both reverse and normal faulting was simulated for a 20 m deep model soil layer, 80 m in width, i.e. the width to depth ratio was 4:1 following Bray's recommendation. Different soil types were simulated, comprising: sand, sandy clay, silty clay, and saturated clay. The cohesion  $c$  was supposed to be linearly increasing with depth, while the shear modulus  $G$  increased parabolically ( $G \sim z^{1/2}$ ). The dip angles for normal faulting were varied from 45° to 75°. As depicted in **Figure 4**, the deformation was localized in a narrow zone. The normal ruptures increased their dip, while the reverse ones decreased it propagating to the surface. The normalized fault displacement  $h/H$  (fault displacement / soil layer depth) to propagate the rupture to the surface was ranging from 1 % to 2.2 %, increasing with the increase of  $K_0$ . Decreasing the fault dip angle led to the increase of the divergence of the fault trace from its idealized straight projection. This divergence ranged from  $0.4H$  to  $0.6H$ , while for dip angles of lower than  $45^\circ + \psi/2$  a secondary inverted rupture and a gravity graben were consistently formed, which is consistent with Lade & Cole's experimental results. The width of the graben ranged from  $0.7H$  to  $1.6H$ . Increasing  $\psi$  lead to the decrease of the graben's width not formed at all in the clay. They considered the strength parameters to be

important, expecting the rupture to propagate with an equivalent dip  $\vartheta$ :  $45^\circ + \psi/2 \leq \vartheta \leq 45^\circ + \phi/2$ , disagreeing with Lade & Cole's allegation that the only significant parameter is the dilation.

More recently it has been shown that the finite element method can quite satisfyingly simulate the phenomenon of fault rupture propagation in the free field (Anastasopoulos et al., 2007) and the FRSFSI (e.g. Anastasopoulos et al., 2009, Loli et al., 2009). Having conducted an innovative experimental work to probe the mechanisms of fault rupture interaction with embedded – caisson foundations gave the opportunity to question if the particular problem can also be adequately fitted in the limits of an unavoidably simplified numerical method. To this end, the methodology of Anastasopoulos et al., 2009 was appropriately adapted to the features of the studied problem. Therefore the aim of the numerical analysis, besides validating the finite element methodology, is to extend the parametric study of the foundation position role, time constrains and other limitations associated with the experimental modeling hinder the conduction of experimental parametric investigations.

## **4.2 FINITE ELEMENT MODEL**

Many of the research conducted so far has been using 2-D modeling, mostly because of time limitations and the lack of strong computational tools. Nowadays, it is possible to realistically simulate the response of the foundation and the surrounding, using 3-D modeling of the problem, which in any case can be more accurate.

For this purpose the FE code ABAQUS is used, as has been so far by other researchers (Anastasopoulos et al, 2005; Loli et al, 2009). The FE model dimensions are chosen to be the same with the dimensions of the physical model at prototype scale, thus 52m length, 15m depth of the soil stratum and 12m width. It should be noted that the exact simulation of the experiment, with scale 1:20, is not chosen mainly because the time required for analysis to run is enormous and so prohibited both for research and practical implementation. As a result some discrepancies between the analytical and the experimental results are expected. In any case, both the experiment and the analysis aim at the understanding of the real scale problem. It should be noted that only the half of the model was analyzed, taking advantage of the symmetry along the axis. Note that the geometry of the model fulfils the requirement of  $Z = 4 H$ , which was suggested by Bray et al., (1994b) in order to avoid boundary effects. That is applied both for the longitudinal and the transverse direction, on the plan view. The analysis model is shown in **Figure 5** and some important dimensions are also depicted.

The analysis was carried out in several steps: The first two steps involved the modeling of stresses into the soil profile. First, the geostatic stresses due to the soil weight were applied (the vertical effective stress ranged from zero on the surface to 240 kPa at 15m depth, where the bedrock is assigned). The static stresses, induced by the weight of the caisson, were added in the second step. The fault rupture was then applied through consecutive static steps via controlled displacements of the hanging wall base nodes. At first the incremental implemented deformation is chosen to be small, 10cm, in order to be able to note the incremental differentiations, and at the final steps, when the formation

of the most important and complementary mechanisms is completed, the increment of the imposed deformation can become up to 0.5m. The geometric nonlinearity of the problem was taken into account during all loading stages. The material and structural components of the problem were modeled as follows:

#### *The Soil*

The soil layer is modeled using hexahedral (8 – node) continuum elements C3D8 of minimum dimension  $d_{FE} = 0.4$  m to a maximum of about 1.8m. The soil unit weight was set equal to a representative value for dense Longstone sand  $\gamma = 16$  kN/m<sup>3</sup>. The stress – strain soil behavior was modeled with a Mohr Coulomb elastoplastic relationship with isotropic strain softening, which is described in the following section.

#### *The Caisson*

0.5 m wide C3D8 elements are used to represent the caisson material also. The caisson elements were given the elastic properties and unit weight of steel.

### **4.3 CONSTITUTIVE MODELLING OF SOIL BEHAVIOUR**

A series of direct shear tests were carried out in order to investigate the stress–strain behavior of the soil used in the centrifuge experiments and determine the parameters of the constitutive soil model used in the numerical analysis. Soil samples were prepared in the same way as the soil specimen for the 1-g experimental model. Because of the large enough inner dimensions of the Fault Rupture Box Apparatus, the density in most areas is approximately the same. This is not the case for the regions close to the two “blind” faces of the box, the one being

vertical barrier on the moving part and the other being the vertical barrier on the steady part of the box. These areas, as also discussed in Chapter 3 and the Appendix A, do not affect the problem simulation, due to the distance from the area of interest. As a result this “problem”, not having the same density 80% (+/- 4%), can be ignored in the numerical simulation. In this particular experimental series it is chosen to be about 80% (for details, look at the Appendix A).

Soil behavior was modeled numerically using the results of the shear box tests with reference to the validated methodology of Anastasopoulos et al., 2007a. According to this methodology, an elastoplastic constitutive relationship with a Mohr Coulomb failure criterion and isotropic strain softening was used. The applied strain softening rule assumed that the friction and dilation angles were linear decreasing functions of the octahedral plastic strain, until they reach their residual-critical state values. They attempted to eliminate the shortcoming of finite element methods in modeling the width of failure surfaces, which arises from inadequate mesh refinement. Their simplified methodology involved the application of a scale factor to the post-peak shear strain values incorporated in the constitutive model to make them compatible to the actual values. The ability of the developed constitutive model to adequately represent the stress – strain behavior of dry sands was verified by the satisfactory agreement with published direct shear test data. A FORTRAN subroutine was encoded to model the strain softening behavior, which was introduced by the linear degradation of the soil friction angle ( $\phi$ ) and dilation angle ( $\psi$ ) with plastic strain as shown schematically in **Figure 6**. The soil behavior is approximated as being divided in the following four phases:

- *Quasielastic behavior* up to the point that the yield strain ( $\gamma_y$ ) is reached.
- *Plastic behavior* from the point that the soil yields to the point that the peak strength is reached (at shear strain  $\gamma_{\text{peak}}$ ).
- *Softening behavior* from the peak point to the point that critical state is reached and the soil is sheared at constant volume (at shear strain  $\gamma_{\text{res}}$ ).
- *Residual behavior* for shear strain values larger than  $\gamma_{\text{res}}$ .

Additionally, in comparison to prior research work where the methodology of Anastasopoulos et al, 2009, was used, the FORTRAN subroutine is modified to take into account the octahedral stress level at each iteration, as the stress level can be an important parameter that defines the soil behavior as the fault rupture propagates through the soil and interacts with the foundation, **Figure 7**. As can be easily understood the internal friction angle of the soil material decreases as the stress level increases and as the shear strain increases. Thus, the constitutive model takes into account the calculated shear strain and the independent parameter of stress level, so as to calculate the friction angle and the dilation angle. Recall, that theoretically the difference between the friction angle at peak and the residual one should be equal to the dilation angle. From the shear test experiments it was found for that for relative density of about 80% and for the stress range in which the experiment is conducted the dilation angle can be considered constant, approximately 13 degrees. Although, the numerical analysis is conducted for the real scale problem, the experimental results are used

to validate the model and so the values taken for the soil material and the conditions during the experiment are used. This simplification is not expected to lead to qualitative errors, but only to quantitative deviation; according to initial numerical tests conducted using the same FEM program and the constitutive model, the model is only little sensitive to the small range of the dilation angle, whereas the most important parameter is the shear strain at which the soil behavior changes from plastic to softening and residual.

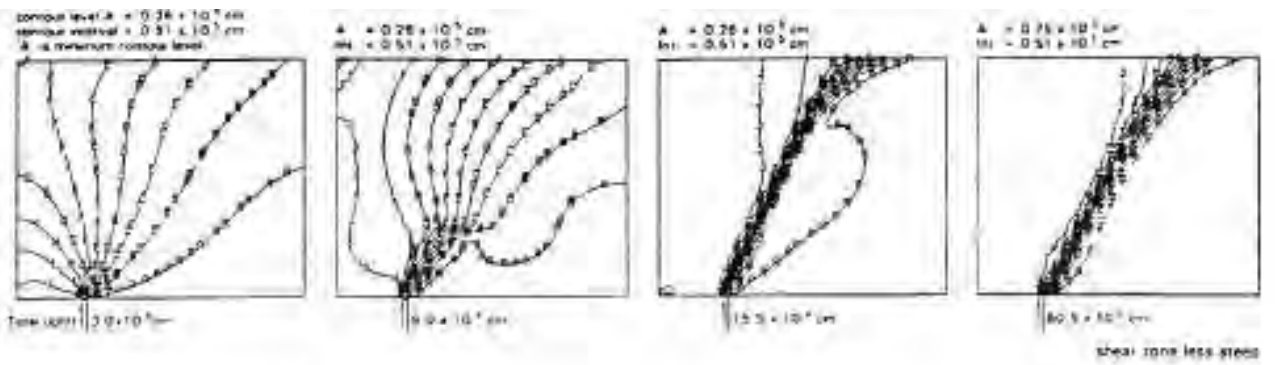
The constitutive model parameters that define the aforementioned phases of soil behavior are calculated with reference to the methodology of Anastasopoulos et al., 2007 and are presented in the Table 4.

#### **4.4 SOIL – CAISSON INTERFACE**

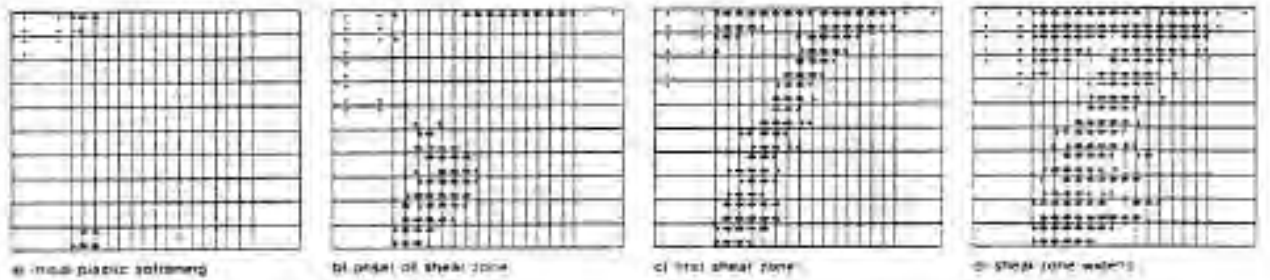
In order to realistically model the soil – foundation interfaces are used, which allow sliding, uplifting and separation (loss of contact with the soil) to occur. Aiming to simulate the 1-g experiments, where sandpaper is used in the contact faces of the caisson with the surrounding sand, the interfaces are given the frictional properties of the experimental interfaces. The friction angle chosen is 0.7 is chosen after shear tests of the sand with the sand paper.



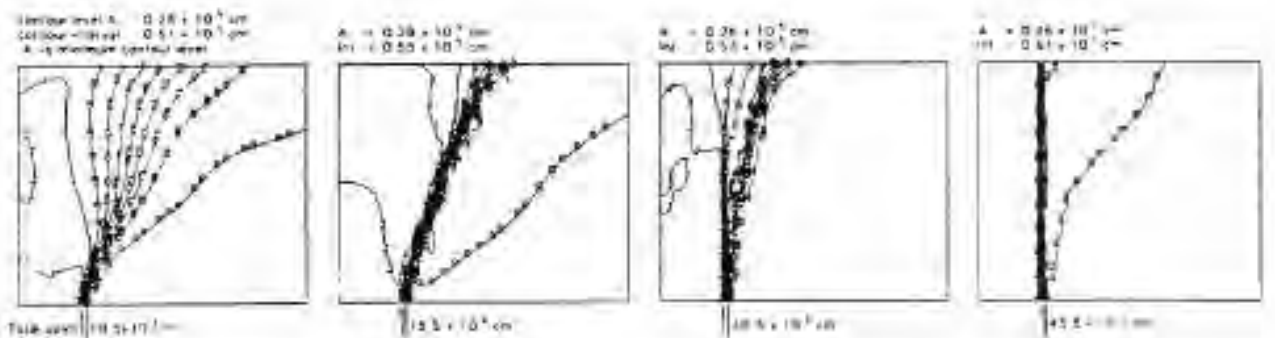
# Figures



plasticity at surface due to softening



(a) Associated flow rule

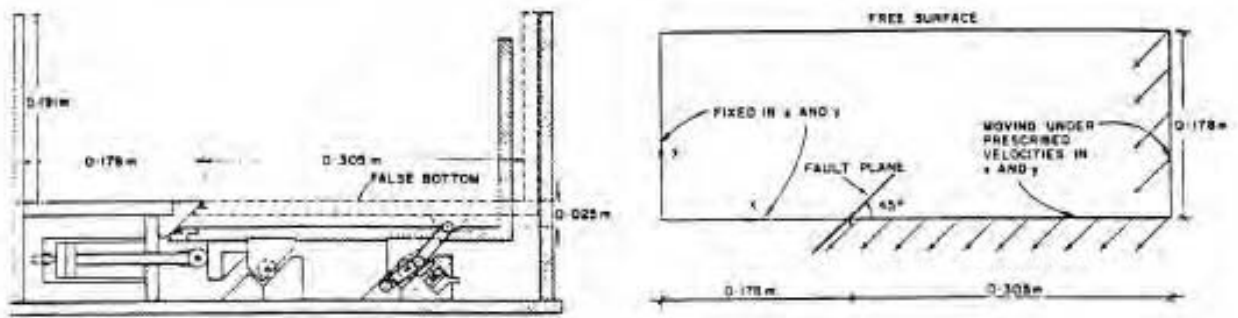


well developed plastic hardening zone

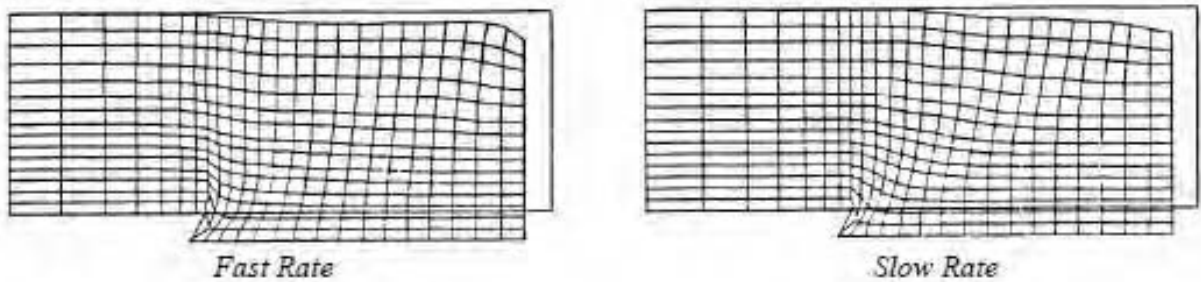


(b) Non-associated flow rule

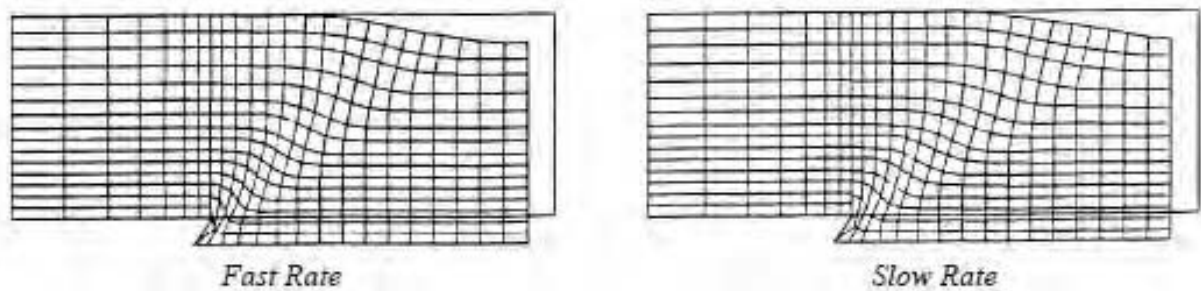
Figure 1. Finite Element analysis results of reverse fault rupture propagation through sand [Walters & Thomas, 1982]



(a) Centrifuge Apparatus Setup

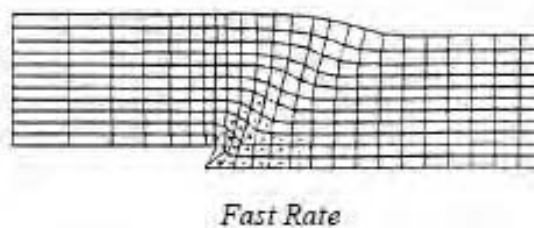


(b) Loose Sand ( $\gamma_d = 14.1 \text{ kN/m}^3$ )



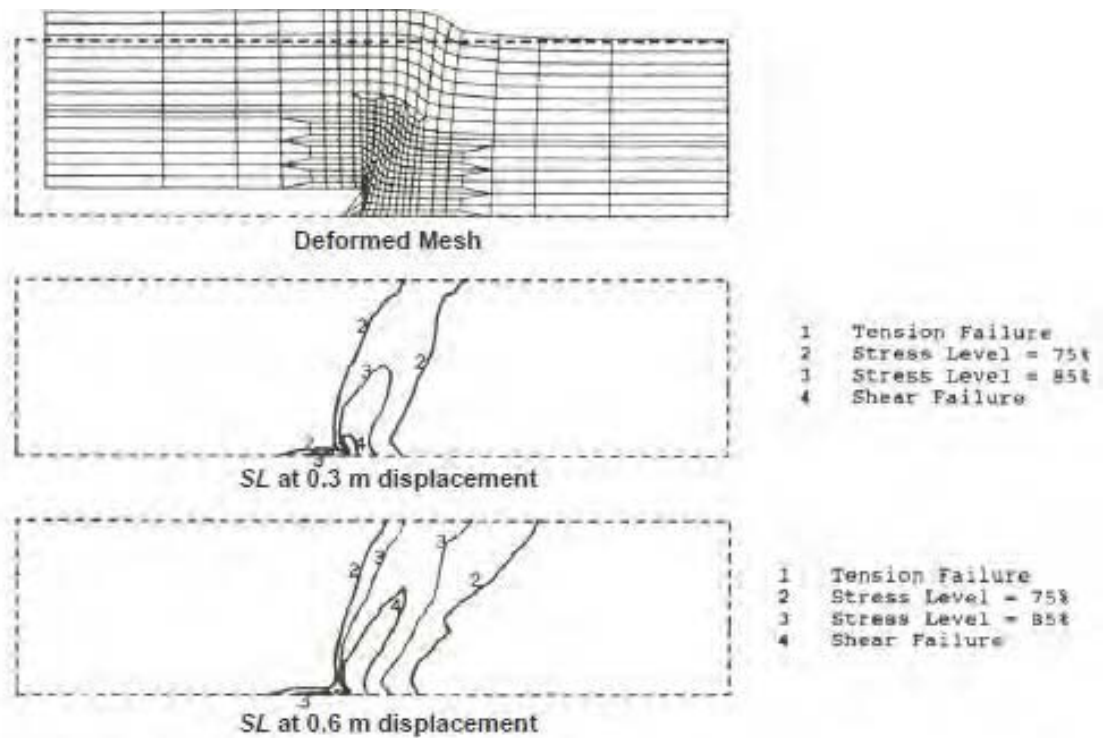
(c) Dense Sand ( $\gamma_d = 17.3 \text{ kN/m}^3$ )  
 $\Psi = 0^\circ$

(d) Dense Sand ( $\gamma_d = 17.3 \text{ kN/m}^3$ )  
 $\Psi = 10^\circ$

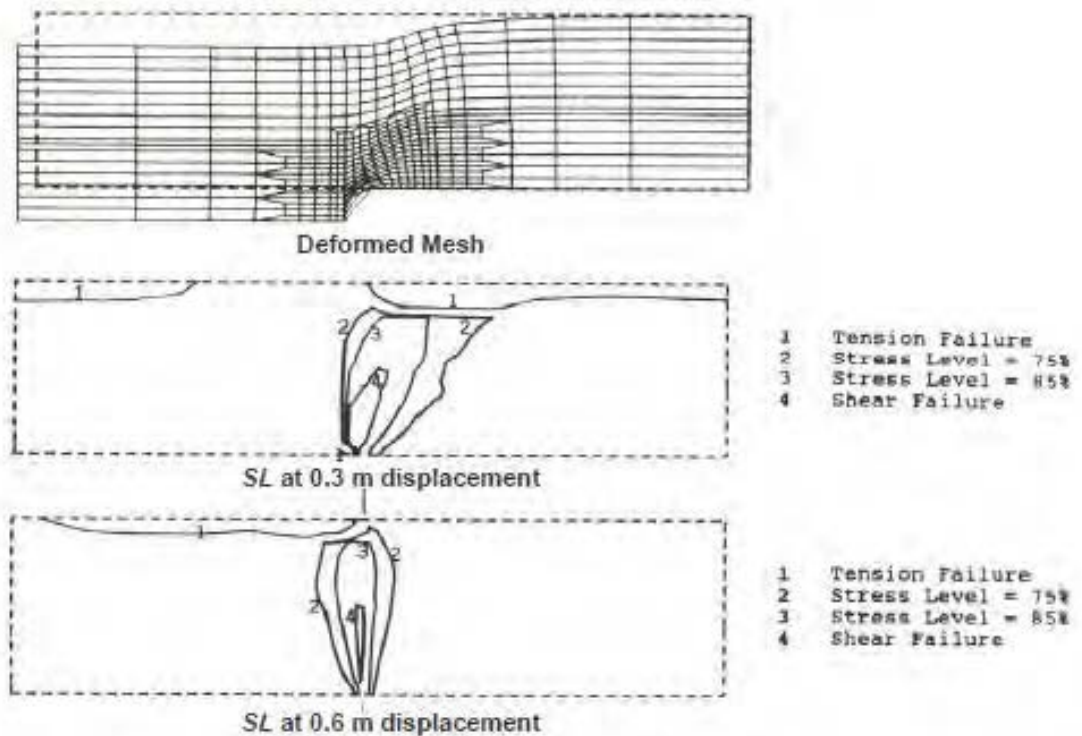


(e) Fine grained silty sand ( $c = 50 \text{ kPa}$ ,  $\phi = 32^\circ$ )

Figure 2. Finite Difference analysis results of reverse fault rupture propagation through sandy materials [Roth, Scott, & Austin, 1982].

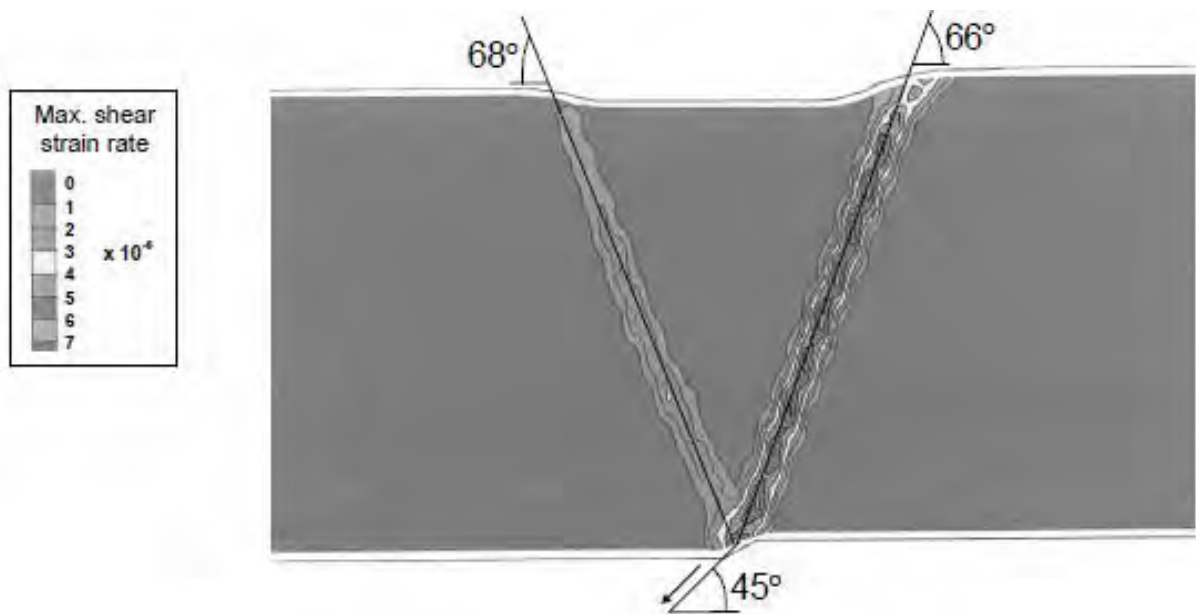


(a) Reverse fault rupture at 45° through a 24 m deep soil layer

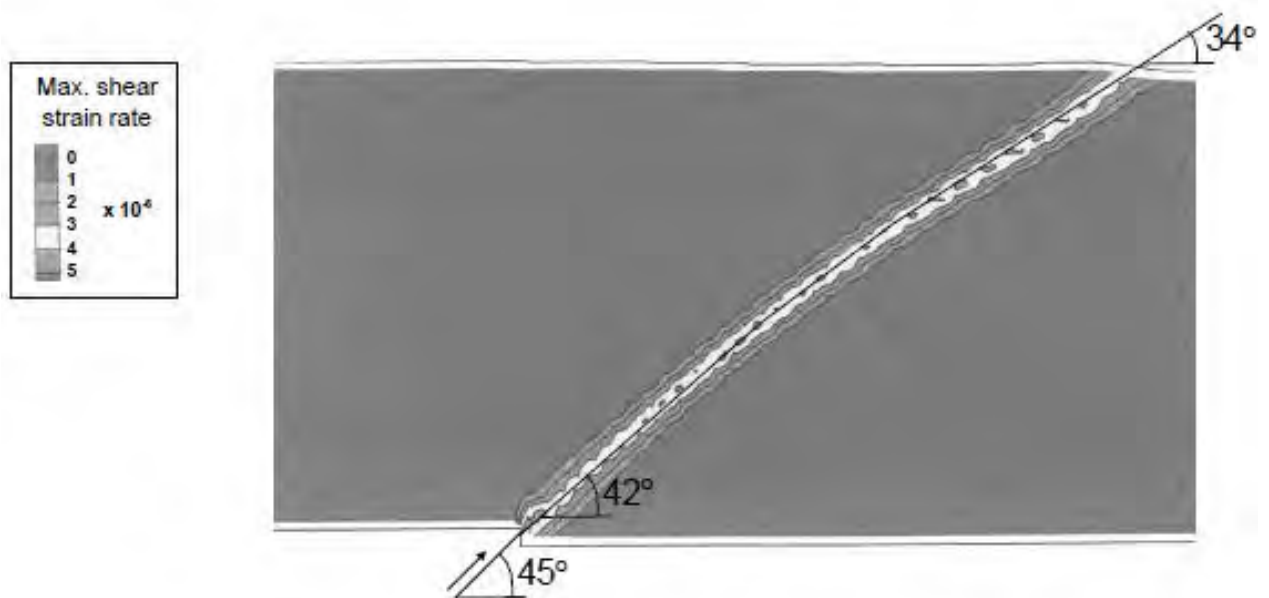


(b) Normal fault rupture at 60° through a 24 m deep soil layer

Figure 3. Finite Element analysis results of normal and reverse fault rupture propagation through clay [Bray, 1990 ; Bray et al, 1994]



(a) Normal fault rupture propagation through sand ( $\psi = 20^\circ$ ) at  $45^\circ$  dip



(b) Reverse fault rupture propagation through sand ( $\psi = 15^\circ$ ) at  $45^\circ$  dip

Figure 4. Finite Difference analysis results of normal and reverse fault rupture propagation [Loukidis & Bouckovalas, 2001; Loukidis 1999]

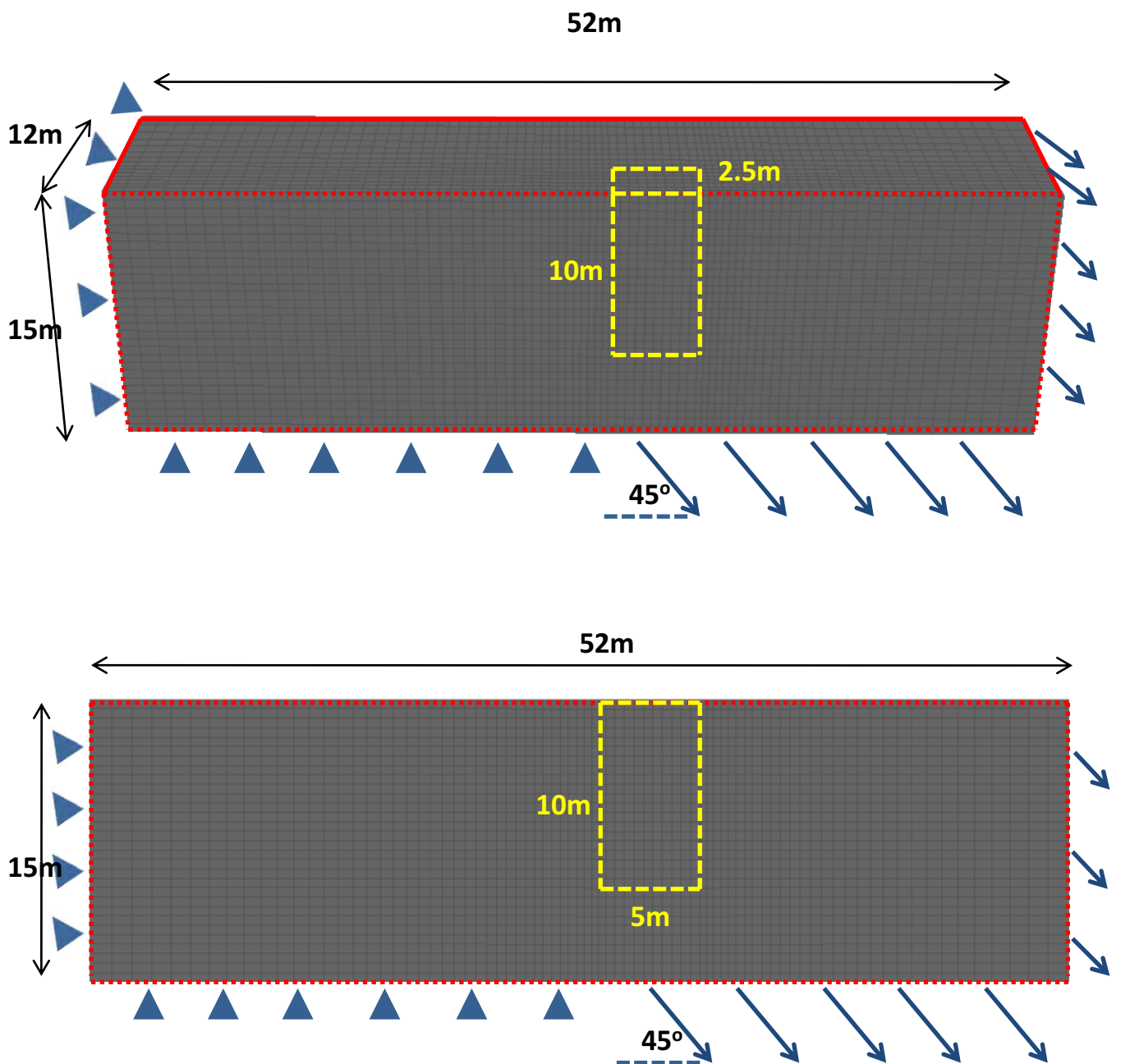


Figure 5. Finite Element model for the case with the caisson system: (a) 3-D view of the model; (b) plan view of the model, indicating the boundary conditions (case of normal fault). With the red dashed line the plane of symmetry is indicated, while with the yellow the caisson.

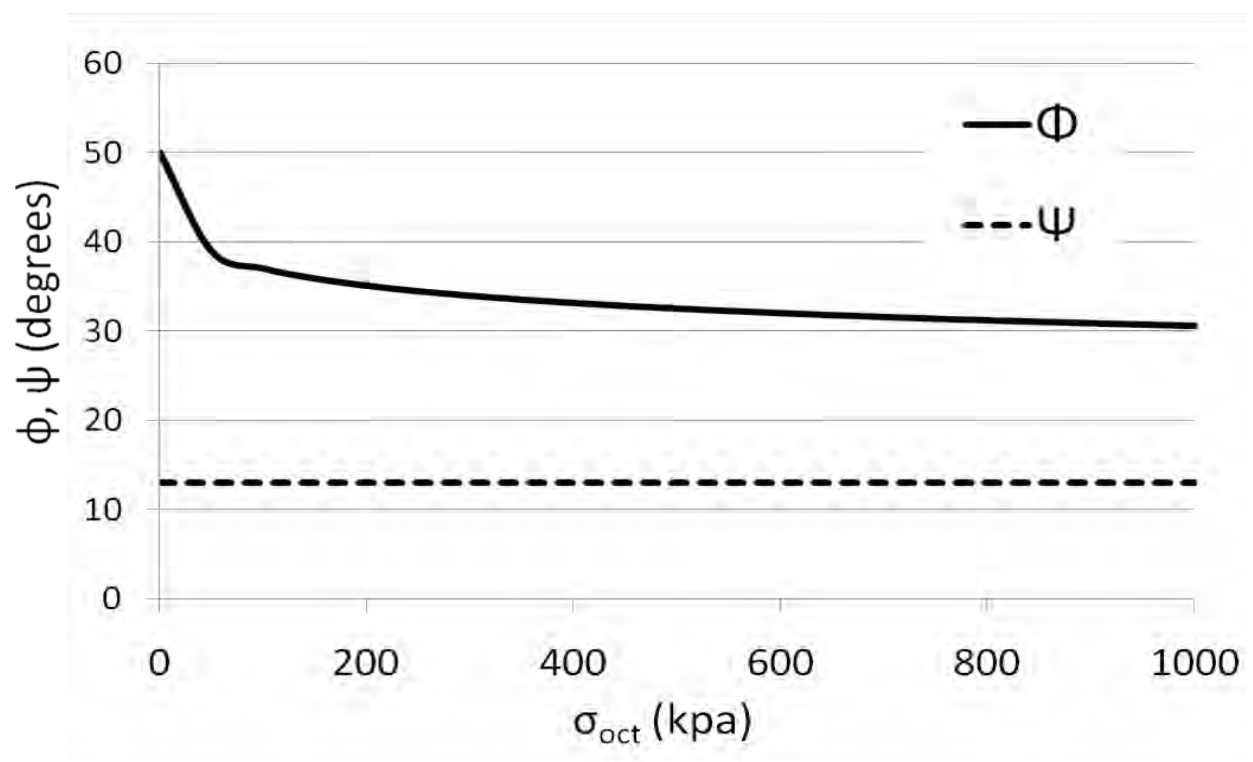
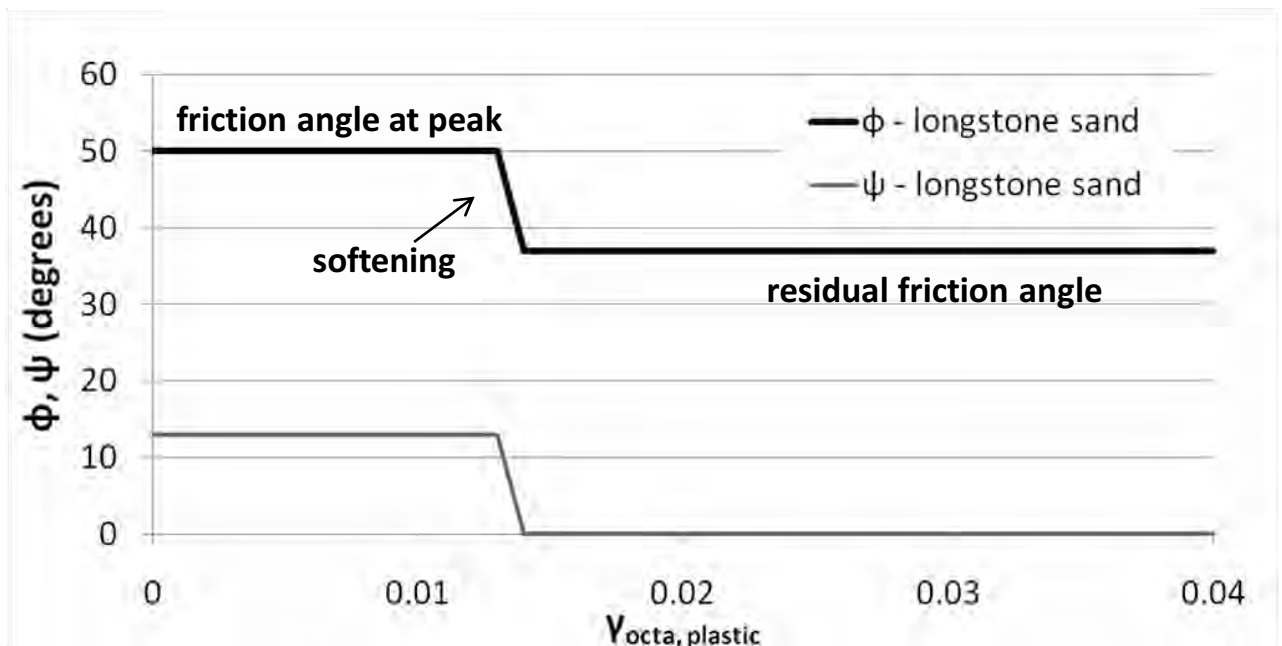


Figure 6. Constitutive modeling of soil behavior after the methodology suggested by Anastasopoulos et al., 2007, complemented by the stress level dependency of the friction and dilation angle: schematic of the linear strain softening relationship used in the analysis and the stress softening relationship.





# *Chapter 5*

## **NORMAL FAULTING**

## 5.1 INTRODUCTION

In this chapter is presented the case of normal fault rupture propagation (downwards movement of the hanging wall) both in the free field case and the scenarios of three different positions of the caisson foundation relative to the fault outcropping. The results are given for the four reverse fault 1-g tests in terms of: (i) deformations and strain localizations within the soil body (i.e. failure mechanisms), (ii) surface displacement profiles and (ii) foundation displacements ( $u$ ,  $v$ ,  $\theta$ ). Moreover, the results of the equivalent numerical analyses are juxtaposed and compared side by side, demonstrating the similarities and some diversions and proofing the effectiveness of the numerical method in capturing the different components of fault rupture propagation in the free field and the FR-SFSI.

The parameter examined is the effect of the foundation position relative to the fault ( $s/B$  and  $x/B$ ), as all other soil and geometric parameters are kept constant, and therefore it was considered essential to study the evolution of the phenomenon in the free field before proceeding to the study of the FRSFSI mechanisms.

The results of the four normal fault 1-g scaled (1:20) tests are presented and emphasis is put on the fault rupture – foundation interaction mechanisms (FRSFSI) and their effect on the foundation performance. As for the reverse faults, the experimental results are compared to the results of numerical simulations of the tests.

## 5.2 FREE FIELD

The results of the free field case for the following interaction tests are presented first. A selection of images captured during the test at different stages of fault propagation is presented in **Figure 5.1a**.

The first to observe that normal faults propagate to the surface more quickly (for smaller values of fault dislocation) compared to reverse faults, were Cole and Lade (1984). Indeed, this seems to be also the case and as shown in **Figure 5.1a** a very steep localization has been formed after just 0.20 m of fault dislocation and the shear strain plane has travelled 13m from the initial point of the outcrop, covering more than 80% of the distance before outcropping. Only 10cm afterwards a second less steep failure surface appears and has already reached the surface, while the former stays inactive till more than 1m of fault throw. As will be seen in the next chapter, for the case of reverse faulting there is a much larger, three to four times, fault displacement needed to propagate the fault to the surface. The fault deformation is localized on this distinct plane that first outcrops and a quite sharp scarp is formatted on the soil surface at a horizontal distance of about 2.5 m from the fault initiation point. When the fault throw is 0.4m an opposite secondary rupture makes its quick entrance into the scene. Across the plane that has been formed by the steep ascendance of the initial fault propagation to the surface, the soil of the hanging wall slides across this plane. As the deformation on the model base increases another reverse secondary rupture paths appear. Nevertheless, the mechanism does not experience any change, except from the fact that the localization zone both primary and secondary becomes wider. Between the two family

paths, the primary that have the same general direction as the dip angle and the secondary that has the opposite direction, a wedge shaped soil mass is forced to subside. It can be seen that after the full formation of the primary and secondary paths the subsidence is of the same order as the fault throw. The experiment was stopped due to loss of sand for  $h > 1.2\text{m}$ , and as the soil specimen was tampered the results are unsuitable for conclusive remarks.

This primary fault emerged on the surface at a distance of about 3 m from the base discontinuity having an almost constant dip angle along its path, more than  $70^\circ$  (by  $25^\circ$  steeper than the base rupture) This enormous difference can be attributed to the stress conditions that are not properly simulated due to the scale and the 1-g gravity conditions.

The above described results are in agreement with former experimental results (e.g. Cole and Lade, 1984; Bransby et al, 2008b, Loli et al, 2009) and field observations of normal fault rupture patterns (see Bray et al., 1994a). Normal faults tend to refract on the soil – bedrock interface and propagate to the surface at increased dip angles; nonetheless the writer believes that the results are overestimated.

Unfortunately, due to lack of targets that would complement the process of the photographic data, the conclusions are presumably limited to be drawn only from the image observation.

**Figure 5.1b** presents the results of the equivalent numerical analysis with regard to the mesh deformations and the associated shear strains taking place at different stages of fault displacement. A very steep, failure plane appears in the numerical analysis, although not so steep as in the experiment. Moreover, the analysis is in accordance with the 1-g

test as far as the steps (level of fault throw) and the evolution of the phenomenon is concerned. This is the case for both the primary and secondary localization planes. Even the width of the zone that increases with the increase of the fault throw agrees with the remarks from the experiment. The aforementioned are supported by Figure 6.2, which illustrates the comparison of the experiment and analysis with reference to the vertical displacements.

### 5.3 NORMAL FAULT RUPTURE – CAISSON INTERACTION

Aiming to examine the mechanisms of the caisson – normal type rupture interaction, three characteristic cases of the possible foundation position with reference to the fault were examined. The results from the three tests are presented herein and compared with the results of the equivalent numerical simulations. It should be remarked that in the last two tests N\_03 and N\_04 connection with the side camera was lost during centrifuge spinning at the early stages of fault loading (at fault displacements  $h = 0.3$  and  $0.5$  m respectively). In order to regain connection with the camera the centrifuge was stopped and spun up again. Although this didn't have any evident effect on the model, it doubts the validity of these two tests. Time restraints in the availability of the centrifuge didn't allow the repetition of the tests.

#### 5.3.1 Test 1 - NFR: $s/b=0.16$

In this test the caisson was positioned so that the free field rupture would cross its base in the vicinity of its right corner as shown in **Figure**

**5.3a.** Images captured during the six steps of the experiment are also shown in **Figure 5.3a** demonstrating a particularly vivid interplay of different failure mechanisms. For 0.2 m of fault displacement it is shown that general deformation occurs on the hanging wall and underneath the right corner of the caisson, without evident localization almost parallel to the interface of the foundation with the surrounding soil. This is indicative of the fact that the already steep fault rupture plane becomes even steeper, almost vertical, due to the divergence of the fault path by the caisson. Note that, at the same amount of fault displacement, there was a localization observed in the free field, extending about 13m from the base of the model, Figure 5.1a).

**Figures 5.3 – 5.6** depict that, the rigid caisson acts as a kinematic constraint that forces the rupture to deviate towards its right edge. The fault induced displacement is concentrated on a diffused zone which connects the base discontinuity with the caisson's right corner and right side. As the deformation increases, another shear strain localization appears, diverting from the left corner reaching the surface, at  $h=0.4\text{m}$ , while also the first observed path to the right side of the foundation outcrops. The area near both sides of the caisson enveloped by the outcropping shear zones is remarkably disturbed. At this point the rotation of the foundation to the right is becoming noticeable and the causative mechanism is the subsidence of the soil under the caisson, due to the base dislocating of the hanging wall. The caisson rotating towards the hanging wall creates active type lateral pressures in the soil of the footwall (imagine the caisson acting as a rotating retaining wall).

The evolution of the phenomenon results in the formation of other additional shear strain zones and the more extensive disturbance of the soil around the caisson, as well as in some sliding of the soil in the interface with the caisson. Moreover, the soil underneath the caisson base is evidently subjected to significant straining due to the rotation of the caisson. The soil failure on the footwall side “facilitates” the diversion of the fault rupture to the left. At larger than 0.7m fault displacements the left mechanism becomes the main active fault. At  $h=1.2\text{m}$  the caissons rotation has forced the soil to its right to fail in a complex combination of shearing, due to fault propagation and a type of bearing capacity failure mechanism.

**Figure 5.3b** presents indicative results of the numerical simulation of test focusing on the failure mechanisms developed at different stages of faulting. It demonstrates that the analysis is in agreement with the experiment and captures the development and the evolution of the previously described mechanisms. Although the slope formed on the surface during normal fault rupture doesn't allow tracking of the surface rupture path with great accuracy, the figure clearly shows the similarity between analysis and experiment regarding the FRSFSI mechanisms.

Comparing the side views shows that the numerical analysis captures the mobilization of the three failure mechanisms, which have been described above. The numerically predicted value of the active failure mechanism angle is in accordance with the experiment, while the mechanism in the right side of the caisson is bit wider in the experiment. Nevertheless, general pattern of behavior is very similar. Moreover, both analysis and experiment show the formation of a gap (loss of contact

between the soil and the caisson) on the footwall and back side of the caisson. However, the extent of this gap is underestimated in the analysis. This is also shown by the displacement profiles along the model surface in **Figure 5.8**. It is indicated that the numerical analysis slightly underestimates the steepness of the surface discontinuity and the extent of the gap formatted at the soil –caisson interface for fault throws larger than 0.5 m. This discrepancy is related to the underestimation of the fault localization in the analysis, which leads also to the disagreement between analysis and experiment regarding the fault outcropping point.

Despite the aforementioned discrepancies, the numerical analysis captures the overall mechanistic behavior of the fault – caisson interaction. This is demonstrated by **Figure 5.7**, which shows that the analytical results are in accord with the experimental results in view of the caisson performance (rotation and translational displacements) for all stages of fault loading.

### 5.3.2 Test 2 - NFR: $s/B = 0.38$

**Figure 5.9a** portrays a set of images of the experimental model captured at different stages of the test. The relative to the fault caisson position in this case is shown, which refers to the initial condition ( $h = 0m$ ). As in the previous test the free field fault rupture interacts with the caisson base. However, in this case the interaction point is almost exactly in the middle of the caisson base (2.7m to the left of the previous test's interaction point).



For small fault displacements,  $h = 0.2\text{m}$ , the figure indicates a general deformation pattern taking place around the caisson base that is similar with the previous scenario. But in this case the diverted in two distinguished rupture paths localization happens simultaneously. Moreover, the width of the disturb zone around the caisson is significantly larger and from the beginning the main fault rupture is the one to the left of the caisson, thus the localization is steeper, in both sides. This can be also seen by the incremental displacement plots in **Figure 5.10**. On additional fault throw, when  $h = 0.3\text{ m}$ , the main fault outcrops; crossing its bottom left corner it propagates towards the soil surface with a dip angle approximately  $75^\circ$ , as is the dip angle of the free field rupture. In addition, due to the component that propagates parallel to the soil-foundation interface some sliding is evident. The incremental displacement plots in **Figure 5.10** also show the localization of strains on this steep plane, indicating the deviation of the fault rupture to the left of the caisson. It is believed that the strain field on the left of the caisson is aggravated by the development of active type conditions in the area due to the clockwise rotation of the caisson. The localization, which emerges at the surface for  $0.3\text{ m}$  of fault throw is probably the result of an interplay between the fault rupture being diverted to the left of the caisson and the active type failure of the soil because of the associated caisson displacements (i.e. the fault diversion at the corner of the caisson causes it to rotate towards the hanging wall and active failure mechanisms to take place on its footwall side – these mechanisms on their turn facilitate the propagation of the rupture to the surface).

A distinct failure surface is formed for fault throw  $h = 0.3\text{ m}$  as shown and thereafter the fault induced shear deformation is concentrated on

that plane. As the fault throw increases the clockwise rotation of the caisson creates as in the previous test a complex mechanism, result of passive failure and localization due to the right diverted component. This time the disturbed area is narrower. Although the fault induced deformations are concentrated on the aforementioned failure plane, the rotation of the caisson causes additional shear localizations to mobilize. Namely, a diffused shear zone develops around the bottom right corner, which can be observed by the vector plots for  $h = 0.7$  m. The shearing deformation on this area cumulates due to the progressive increase in the foundation displacement and forms an evident shear plane along the caisson's right side wall for  $h = 1.0$  m (Figures 5.10).

The aforementioned failure mechanisms (i.e. the main fault rupture plane and the secondary localizations caused by the caisson rotation) are schematically indicated in **Figure 5.9b**, and presents the results of the numerical analysis in terms of plastic strains developed in the deformed FE mesh at different levels of fault displacement. The figure demonstrates the qualitative agreement between analysis and experiment with respect to the FRSFSI mechanisms. The main failure plane appears for fault throw  $h = 0.2$  m, at the same level of fault throw compared to the experiment. Analysis and experiment go side by side for almost every step during the evolution of the phenomenon. In accordance with the test, there is a diffused shear deformation zone underneath the caisson base which takes the form of a more localized failure plane as it propagates from the left caisson corner to the soil surface. The analysis agrees with the experiment on the amount of fault throw needed to propagate the localization to the surface.

Moreover, the analysis captures the mobilization of the aforementioned secondary localizations on the hanging wall due to the caisson rotation (shearing along the caisson right sidewall and passive type wedge on the top right corner). The displacement profiles in **Figure 5.14** show that as it was also the case previously, the analysis does capture the localization of the fault resulting in a wider and more evenly distributed failure compared to the experiment, although there is a small difference in the location of the fault outcrop, but the general mechanism of the fault diversion is similar. The main discrepancy between analysis and experiment however, refers to the extent of the gap developed on the top part of the caisson's left sidewall. The extent of the gap is underestimated by the analysis and this was the case in the previous test too. However, this disagreement doesn't necessarily indicate a limitation of the numerical methodology and could be probably attributed to 1-g conditions during the scaled test.

The latter figure demonstrated a reasonable agreement between analysis and experiment regarding the soil displacements, which is also the case for the caisson displacements, for smaller and for larger values of fault throw; analysis and experiment agree in the evolution of the translational displacements ( $\delta x$ ,  $\delta y$ ) of the caisson.

### 5.3.3 Test 6: $s/B = 0.80$

**Figure 5.19** shows a selection of images captured during test with  $s/B$  ratio equal to 0.80. In this test the caisson was placed in a way that the middle of its base was at the same horizontal position with the fault initiation point and the free field fault rupture would interact with the

left side of the caisson base as shown in **Figure 5.15a**. Very quickly after the fault loading had started, for a fault displacement = 0.2m a localization is mobilized. Initiating from the fault base application point the rupture plane intersects with the caisson base and propagates towards the surface increasing significantly in dip. The corresponding incremental displacement plot proves the diversion of the fault to the left of the caisson base. The localization has just emerged at the soil surface approximately 1.5 m to the left of the caisson's top left corner. The incremental displacement plots for the same faulting suggest that there is no deformation occurring outside the distinct plane and prove its very steep orientation. The caisson and the soil on the hanging wall seem to translate rigidly without being evidently distressed. At  $h=0.7$  when a second localization appears, having propagated almost to the surface (during the additional 0.2m of fault throw). It is interesting to notice the similarity in response between this test and the free field test. Not only are the two fault mechanisms observed herein similar in shape with the main faulting mechanisms in the free, but also they develop and evolve concurrently. This observation indicates that the caisson's presence in this case has a less dramatic effect on the fault propagation compared to the two previous interaction tests. In particular, the presence of the caisson in this test has caused no extreme alteration of the failure planes' pattern, but only a 1.5 m deviation of the two mechanisms to the left. Nevertheless, the caisson experiences rotation as the wedge shaped between the right and left rupture paths subsides.

**Figure 5.15b** illustrates the numerically computed failure mechanisms for different stages of fault loading. The analysis agrees with the experiment showing that the fault is diverted on the left base corner of

the caisson and then propagates towards the surface in a steep gradient. Although there is no second mechanism developed next to the first fault, the analysis predicts the change in the rupturing dip angle and the formation of a shallower failure plane for fault throw values exceeding 0.5m. The argument that the analysis agrees reasonably well with the experiment in terms of the FRSFSI mechanisms taking place is also supported by the comparison of the surface displacements in **Figure 5.20**.

**Figure 5.21** displays the performance of the caisson with respect to the applied fault throw in terms of displacements and compares the numerical results against the experiment. First, it is important to notice that in this case the caisson experiences far smaller rotations compared to the two previous tests. This verifies the previous argument regarding the limited interaction of the caisson with the fault planes. Although the numerical analysis agrees with the experiment in view of the horizontal and vertical displacements for all stages of faulting, this is not the case for the caisson's rotational movement. Although the numerically derived relationship between fault throw and consequent caisson rotation follows the same trend with the experimental curve, the numerical analysis gives significantly lower rotation values for all fault throw levels.

## 6.4 SUMMARY

Normal fault rupture propagation was first studied in free field conditions and the results are in qualitative agreement with previous research studies and field observations. Normal faults create steeper and more localized failure surfaces, compared to reverse faults, which

are mobilized for lower values of fault displacement and propagate faster to the soil surface. A progressive type of failure is demonstrated which involves the mobilization of more than one localizations, progressively shallower ones, taking action at different stages of faulting. As with reverse faults, three fault – caisson interaction cases were studied referring to three different caisson positions. Again, the presence of the rigid caisson body caused the rupture to divert from its free field path. The mechanism of fault diversion and its consequences to the foundation's response varied dramatically depending on the caisson's position relative to the fault:

- When the free field rupture interacted with the caisson base near its left corner the FRSFSI mechanism was relatively simple and involved just the diversion and deviation of the main fault to the one left and one right component, relatively to the caisson. The caisson suffered mainly subsidence and only small rotation the imposed loading.

- The test where the caisson base was crossed by the fault rupture near its left corner was certainly more intriguing in terms of the FRSFSI mechanisms taking place. The free field rupture first deviated impressively from its bedrock path, actually changed orientation, and was directed towards the right edge of the caisson base. The shear stresses developed along the right sidewall of the caisson and its consequent clockwise rotation caused the formation of significant active type lateral pressures on the other (left) side of the foundation. Thereafter, a quite subtle interaction mechanism was observed, involving the formation of active and passive failure wedges on the left and right side of the caisson respectively and the fault

propagation on both sides concurrently. The extensive soil failure around the caisson (on its both sides) caused it to experience unavoidably large displacements. In particular, the rotation of the caisson after this test was more than two times larger than the rotation in the previously mentioned test for the same fault throw.

- Quite similar was the case when the free field rupture crossed the caisson base near its middle point. Although there was also a failure zone developed on the right side of the caisson along the depth of its sidewall, the consequences were mitigated and a rupture path component was again diverted to the left. The caisson rotation was in this case smaller probably because of the limited soil failure on its right.

To conclude, the comparison between the 1-g experimental series test and equivalent numerical simulations revealed the effectiveness of the numerical methodology in capturing the mechanisms of fault rupture–caisson interaction. Even quantitative agreement has been succeeded in many scenarios. With respect to the foundation's performance, the analysis was in agreement with the experiments as far as the translational displacements are concerned. The numerical method captures the translational behavior of the foundation. The agreement was in some cases less satisfactory in terms of rotational displacements, yet the analysis captured the general pattern of behavior regarding the foundation rotation with respect to fault throw. The main discrepancy between experiment and analysis refers to the shortcoming of the numerical method to appropriately model the localized failure surfaces occurring during normal fault rupture. As mentioned before, the localization of failure surfaces in FE modeling is dependent on the

elements' width. Hence, in order to improve the performance of the numerical method, especially for normal faults, a finer FE mesh would be required.

It is important to note that the stress conditions during the experiment are not even close to the real scale problem and this can have lead to some miss-prediction of the actual mechanisms; nonetheless both the analysis and the experimental procedure can be judged as important simulation tools for the real scale problem. After all, both numerical and experimental results highlighted the determinative effect of the foundation position on the response of the soil–caisson system.



# Figures

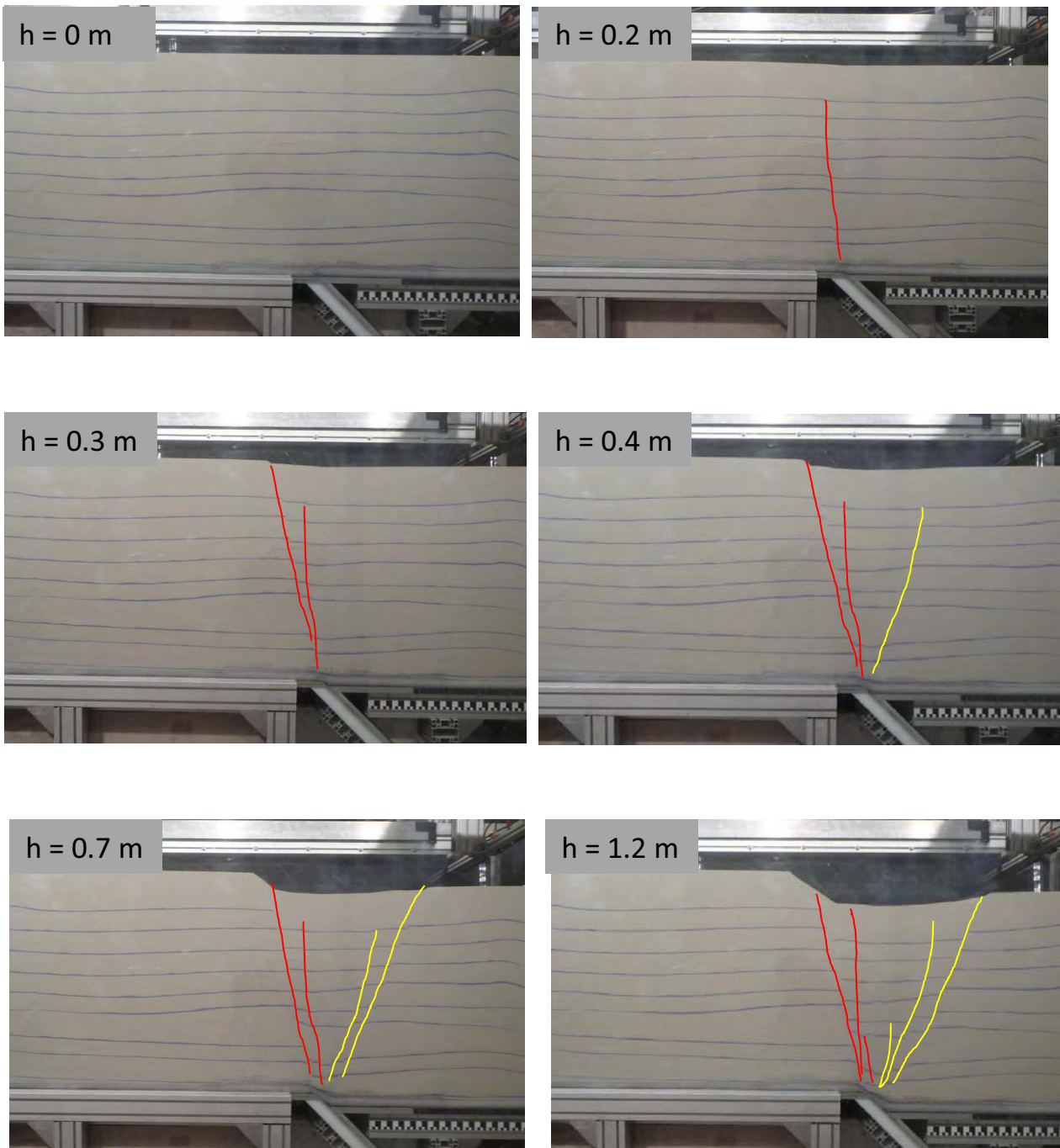


**Figure 5.1a Experiment** – Normal Fault rupture propagation in the free field: Images of the deformed soil model, at six characteristic different deformation steps, indicating the evolution of the fault rupture propagation and the mechanisms that appear.

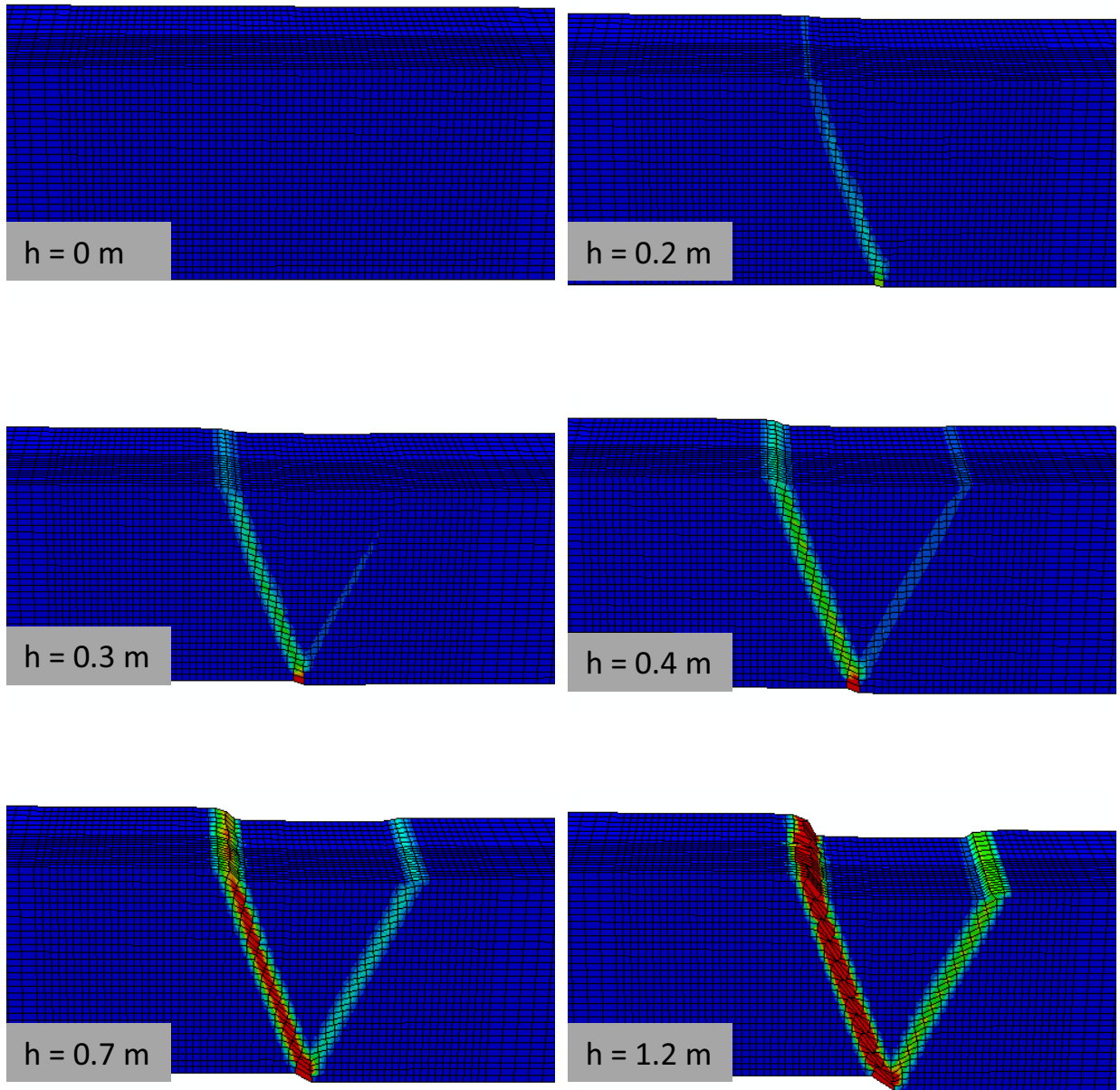


**Figure 5.1b. Analysis** – Reverse Fault rupture propagation in the free field: Images of the deformed soil model, at six characteristic different deformation steps, indicating the evolution of the fault rupture propagation and the mechanisms appeared.

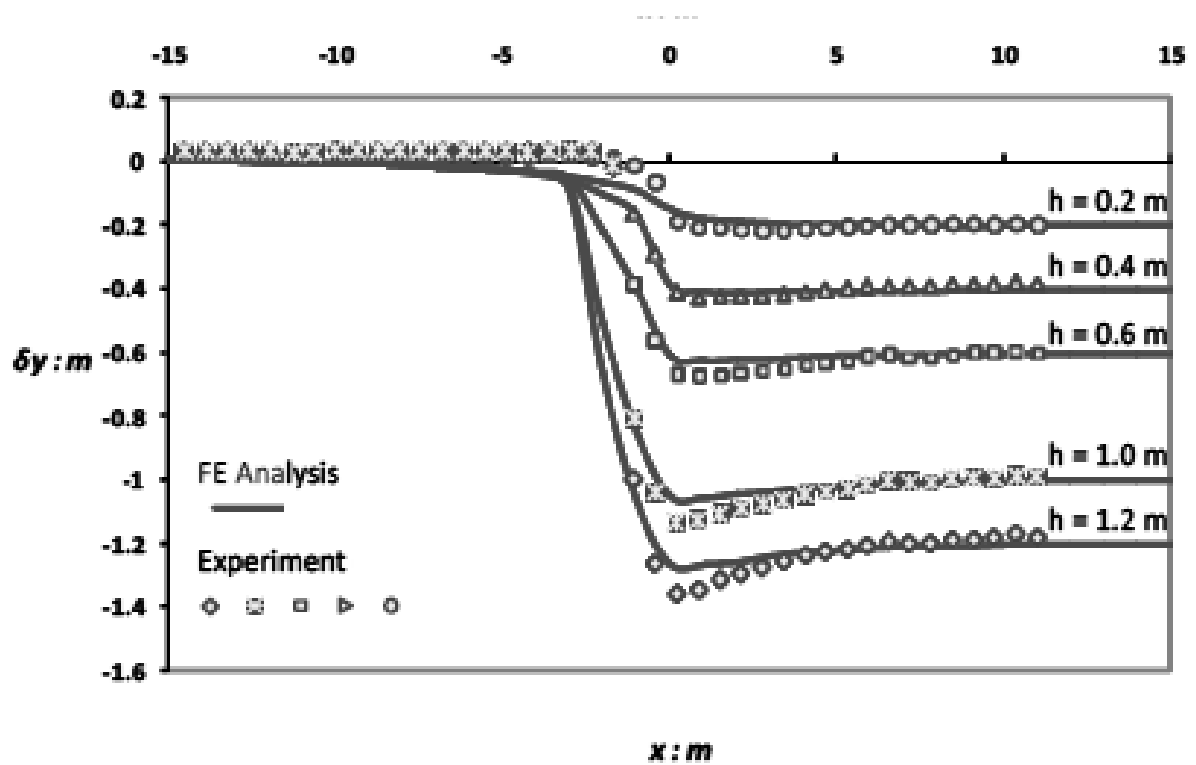


**Figure 5.2.** Comparison between numerical analysis and experimental results referring to the reverse FR propagation in free field: vertical displacements of the model surface with respect to the horizontal position for different fault throw values.

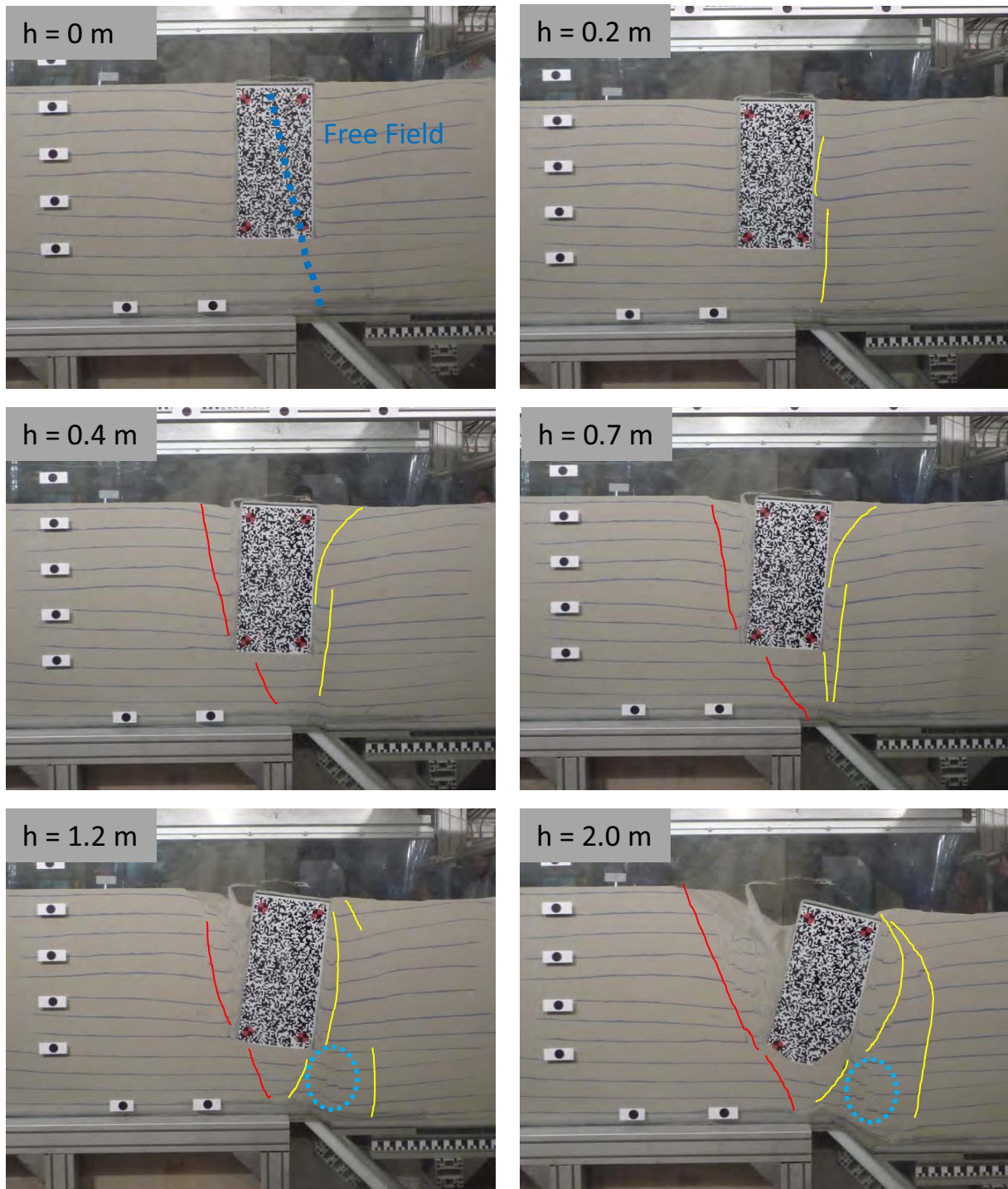


**Figure 5.3a. Experiment** - Snap-shots of soil and caisson deformation at characteristic values of the induced fault rupture displacement  $h$  (prototype scale), for the normal fault rupture scenario with the caisson -  $s/B = 0.16$ . With red denoted the main fault rupture propagation through the soil and with yellow the secondary and the failure mechanisms, due to the displacement of the caisson.

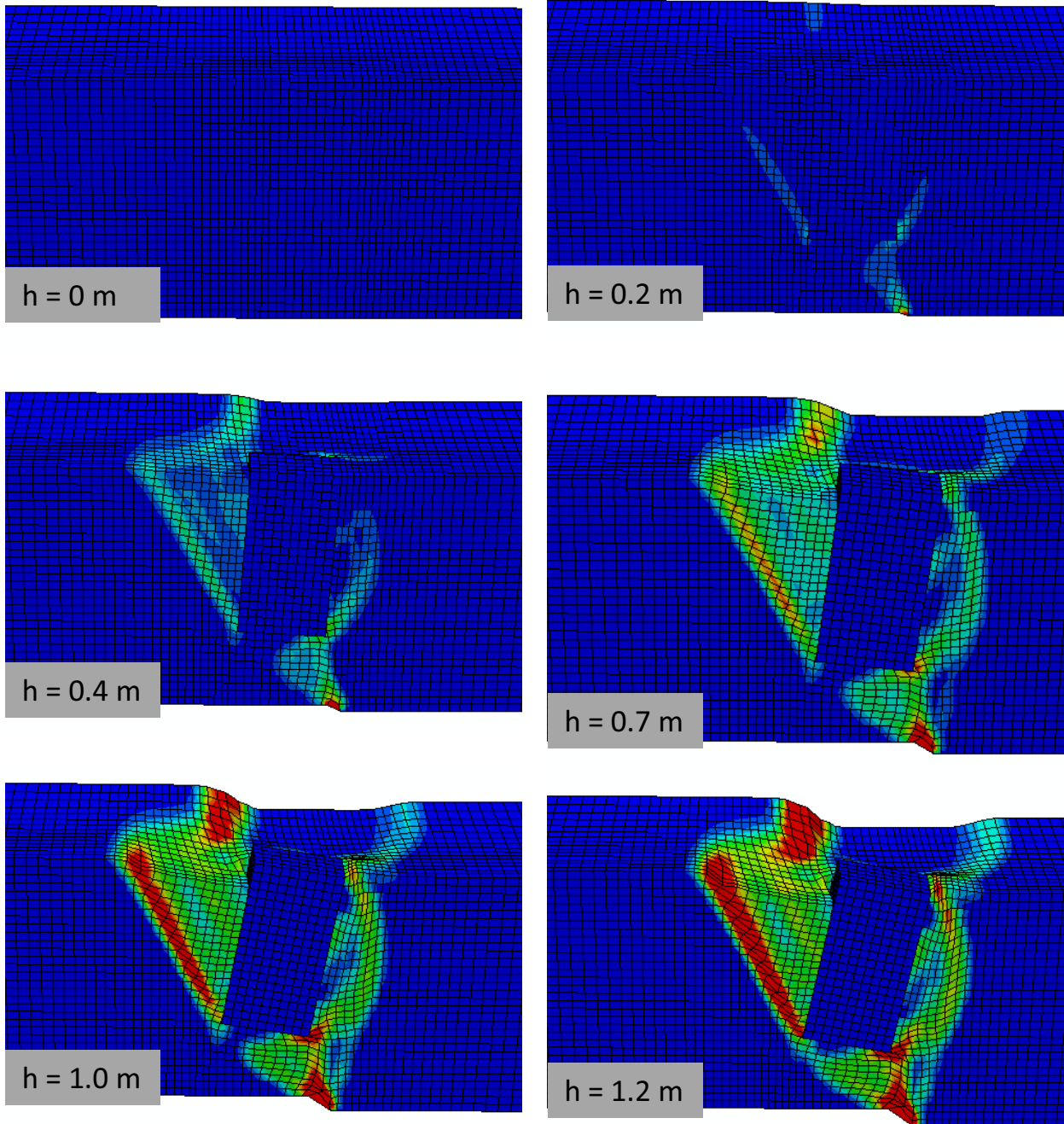


**Figure 5.3b. Analysis** - Snap-shots of soil and caisson deformation at characteristic values of the induced fault rupture displacement  $h$  (prototype scale), for the normal fault rupture scenario with the caisson -  $s/B = 0.16$ .

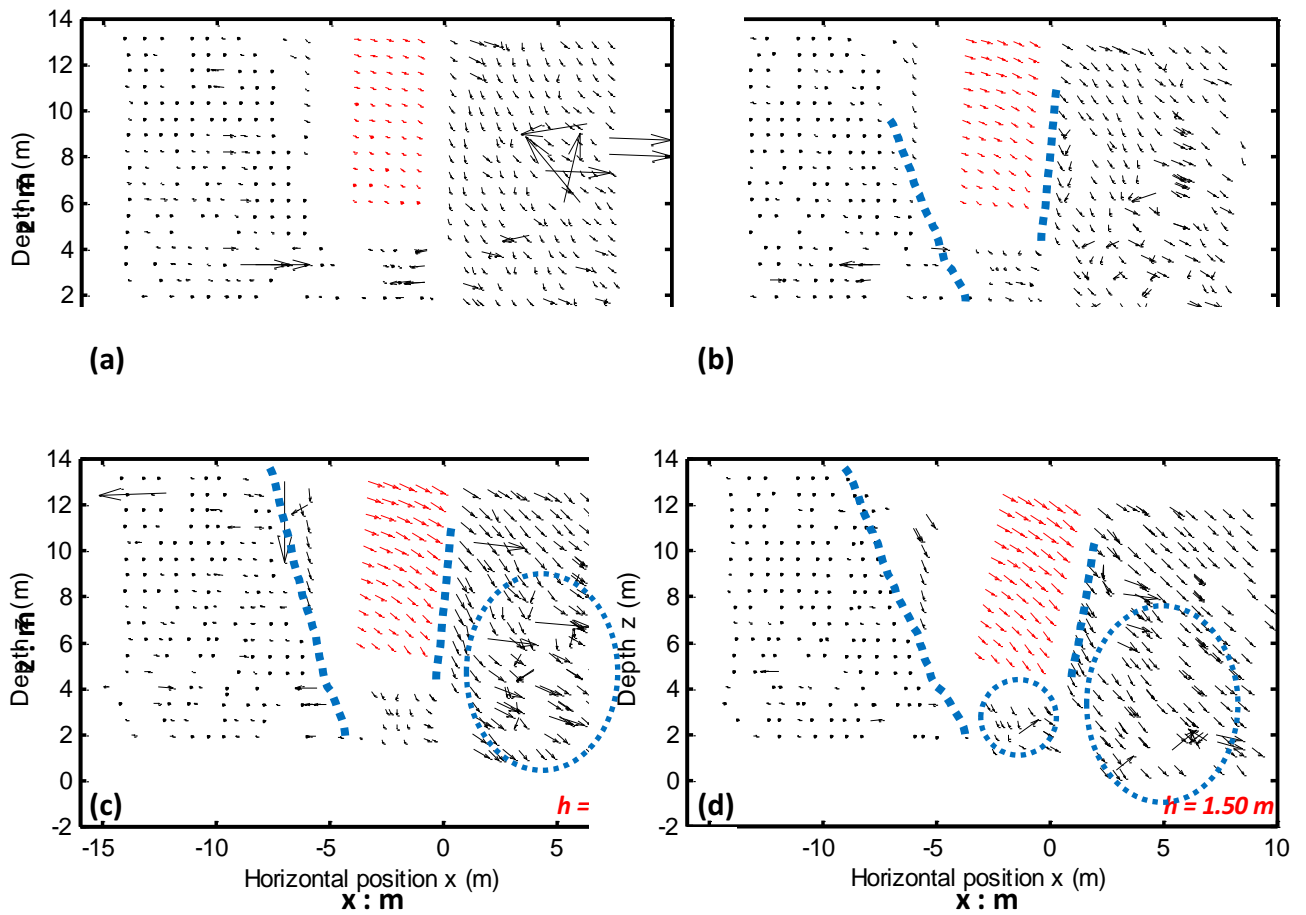


**Figure 5.4. Experiment** -Plot of the incremental displacement of the soil (black vectors) and the caisson (red vectors) in the  $x-z$  plane for different fault through levels, for the normal fault rupture scenario with the caisson -  $s/B = 0.16$ .

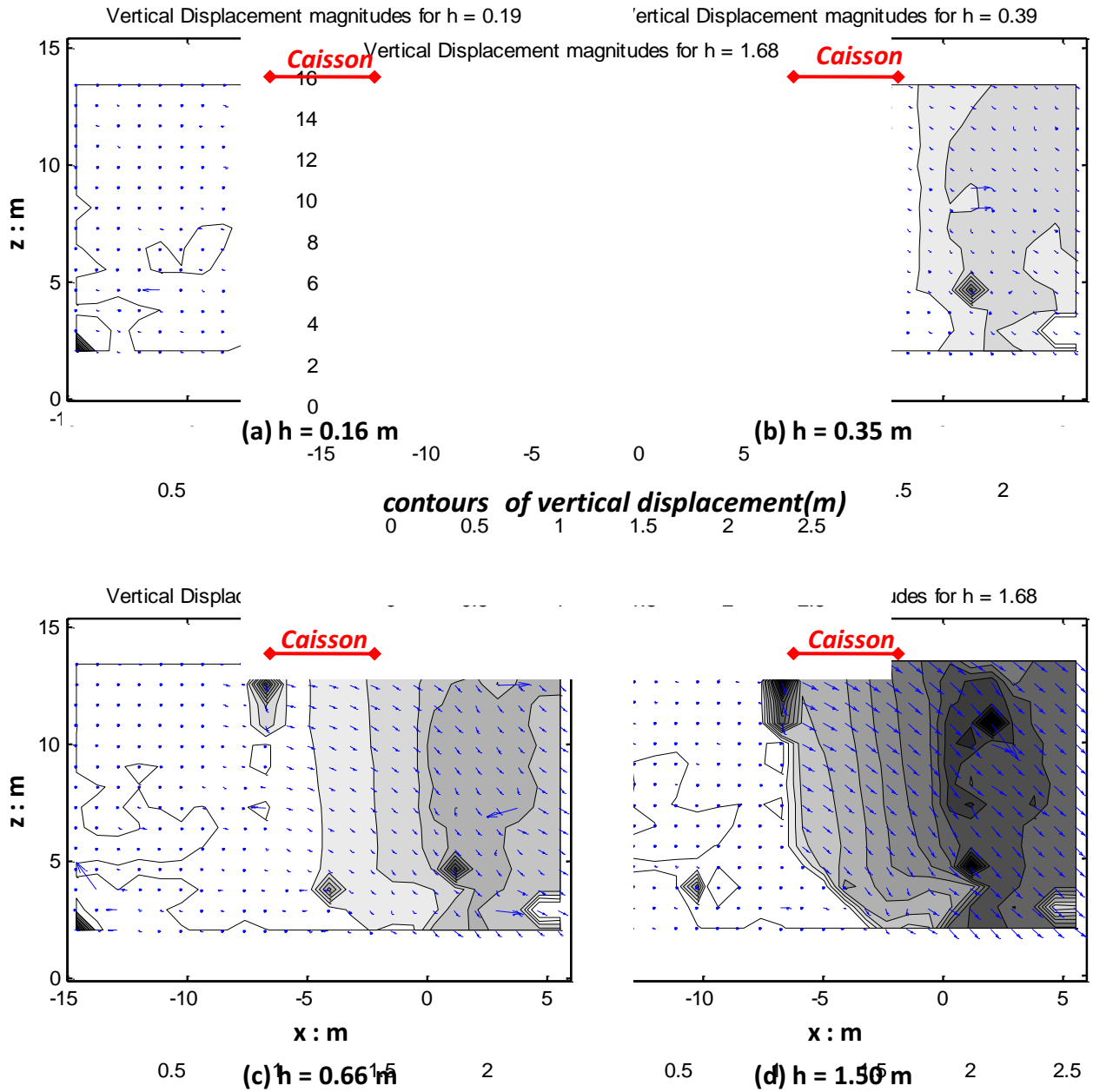


**Figure 5.5. Experiment** - Plot of the incremental displacement of the soil (black vectors) and the caisson (red vectors) in the  $x-z$  plane for different fault through levels, for the normal fault rupture scenario with the caisson  $s/B = 0.16$ .



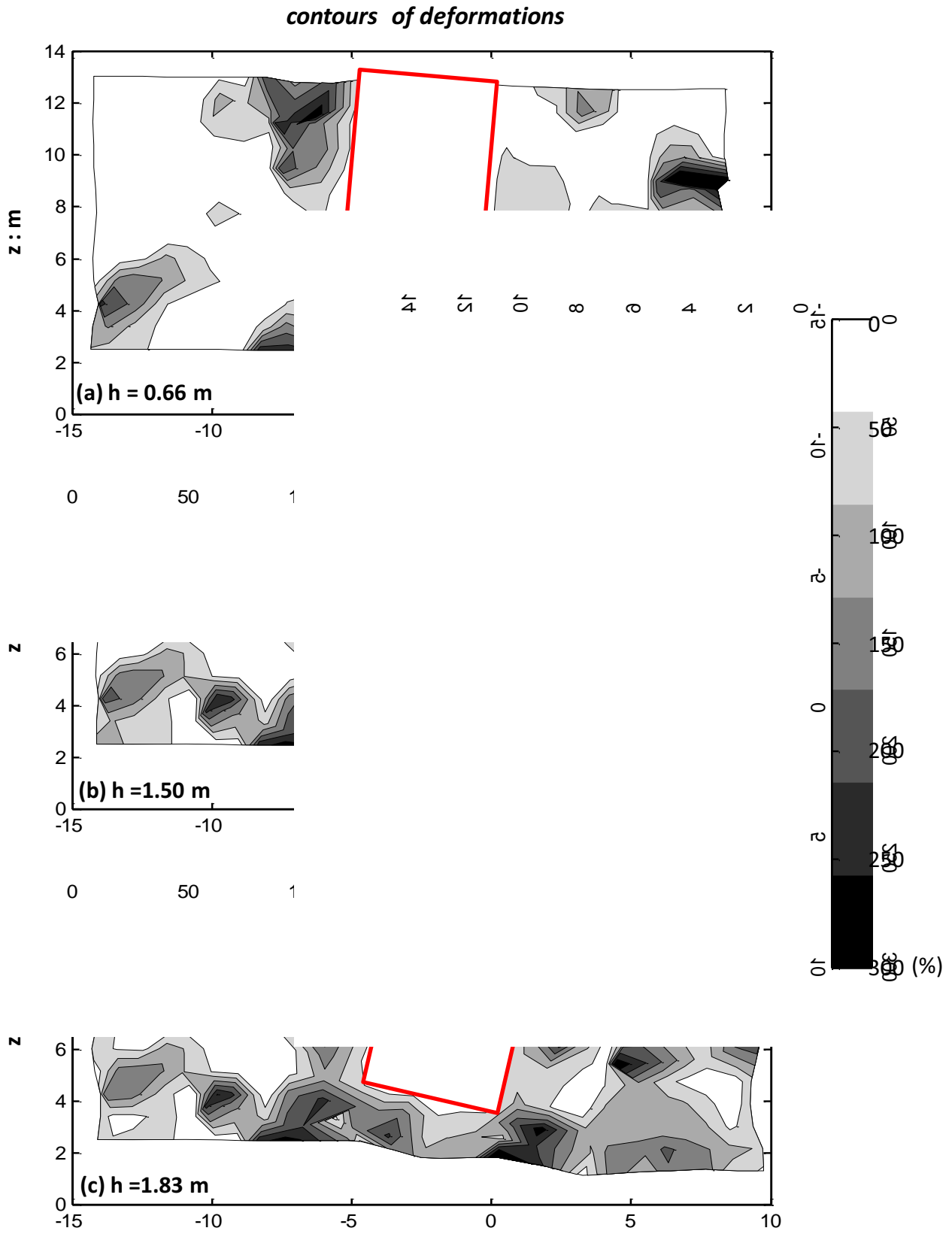


**Figure 5.6. Experiment** - Contours of the deformations in the deformed plane for characteristic values of the fault throw level. Normal fault rupture scenario with the caisson -  $s/B = 0.16$ .

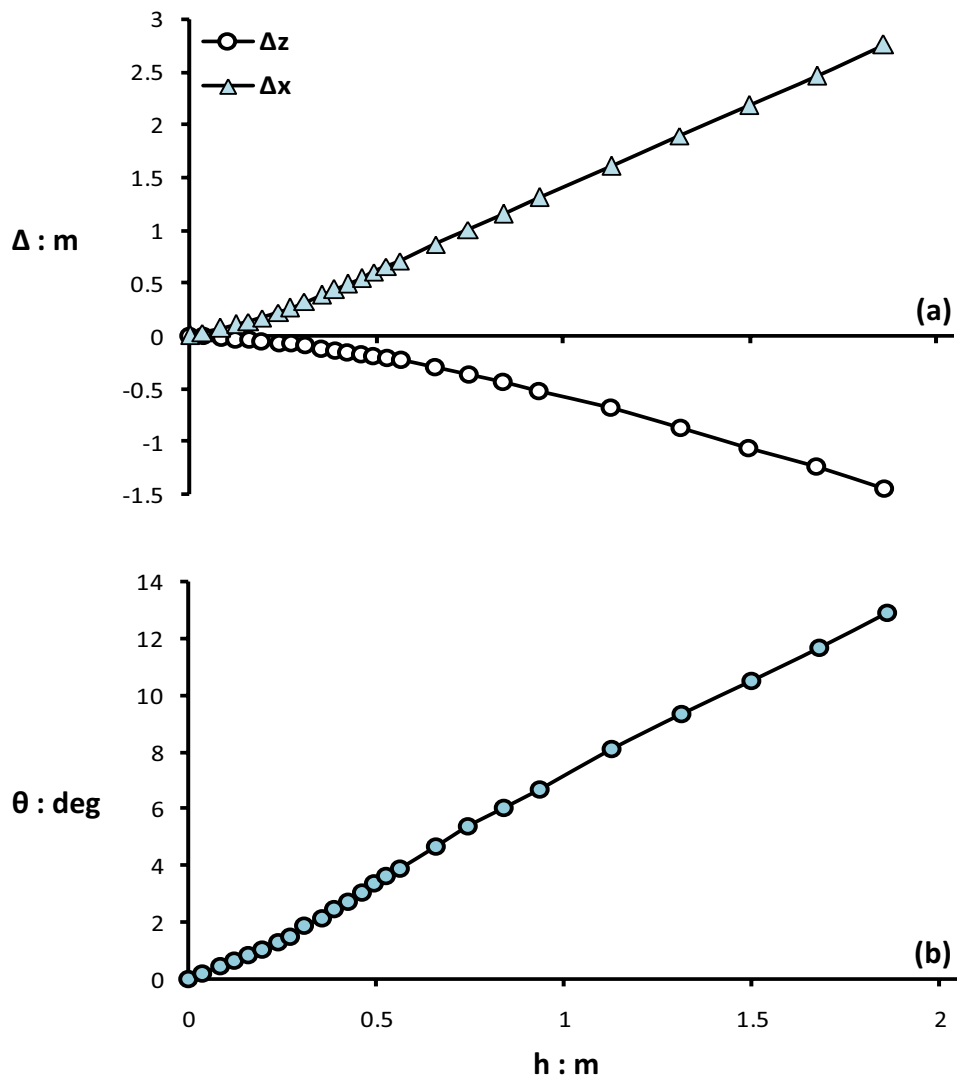


**Figure 5.7.** Evolution of (a) the Displacement and (b) the rotation of the caisson with respect to the normal fault rupture displacement,  $h$ . Reverse fault rupture scenario with the caisson -  $s/B = 0.16$ .

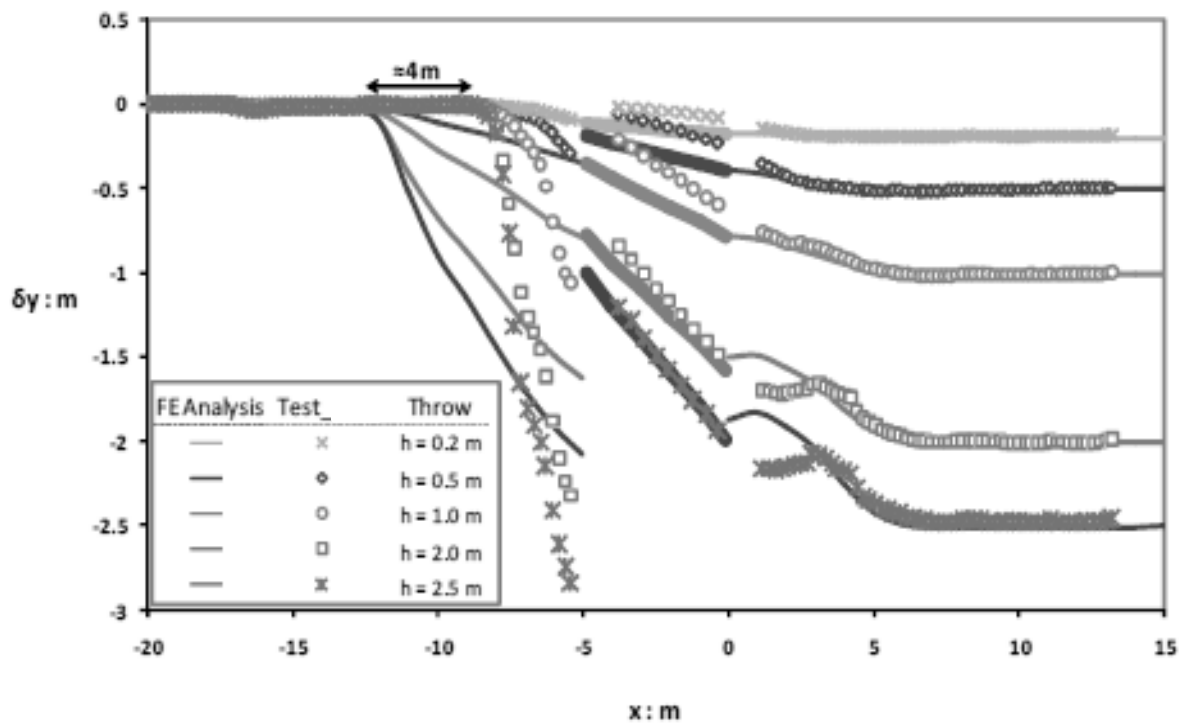


**Figure 5.8.** Comparison between numerical analysis and experimental results referring to the normal FR propagation in the scenario of  $s/B=0.16$ : vertical displacements of the model surface with respect to the horizontal position for different fault throw values.

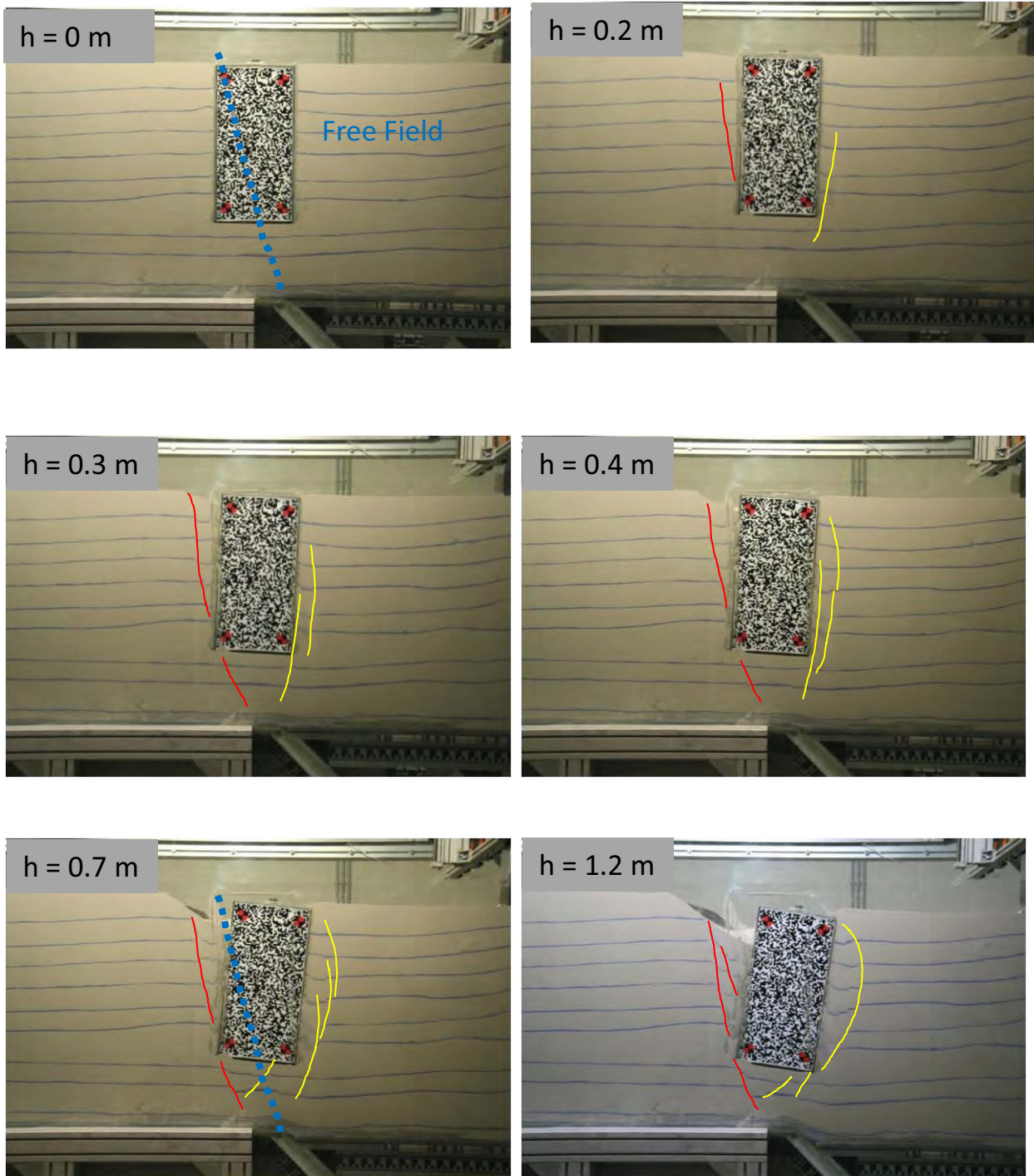


**Figure 5.9a. Experiment** - Snap-shots of soil and caisson deformation at characteristic values of the induced fault rupture displacement  $h$  (prototype scale), for the normal fault rupture scenario with the caisson -  $s/B = 0.38$ . With red denoted the main fault rupture propagation through the soil and with yellow the secondary and the failure mechanisms, due to the displacement of the caisson.

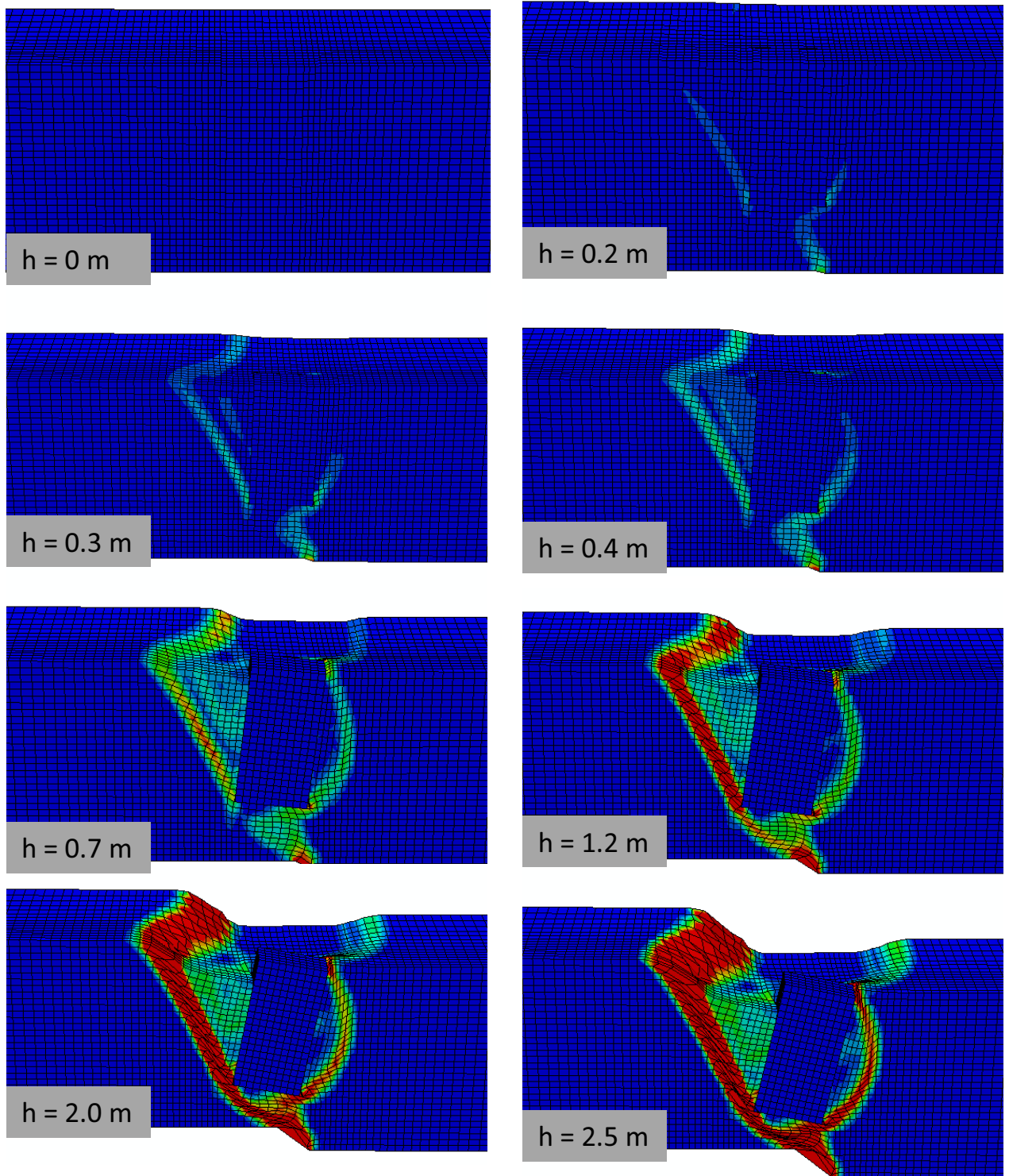


**Figure 5.9b. Analysis** - Snap-shots of soil and caisson deformation at characteristic values of the induced fault rupture displacement  $h$  (prototype scale), for the normal fault rupture scenario with the caisson -  $s/B = 0.38$ .

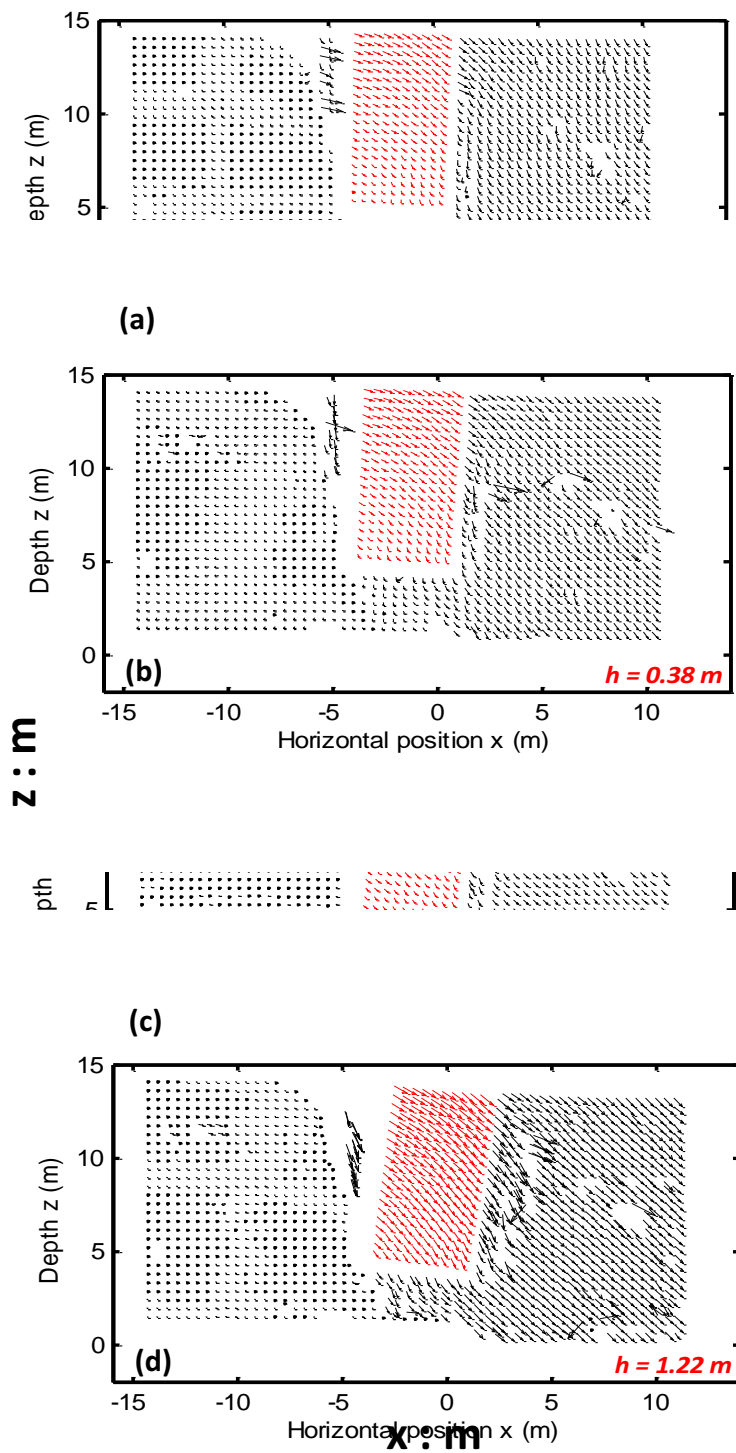


**Figure 5.10.** of the soil (black vectors) and the caisson (red vectors) in the  $x - z$  plane for different fault through levels, for the normal fault rupture scenario with the caisson  $s/B = 0.38$ .

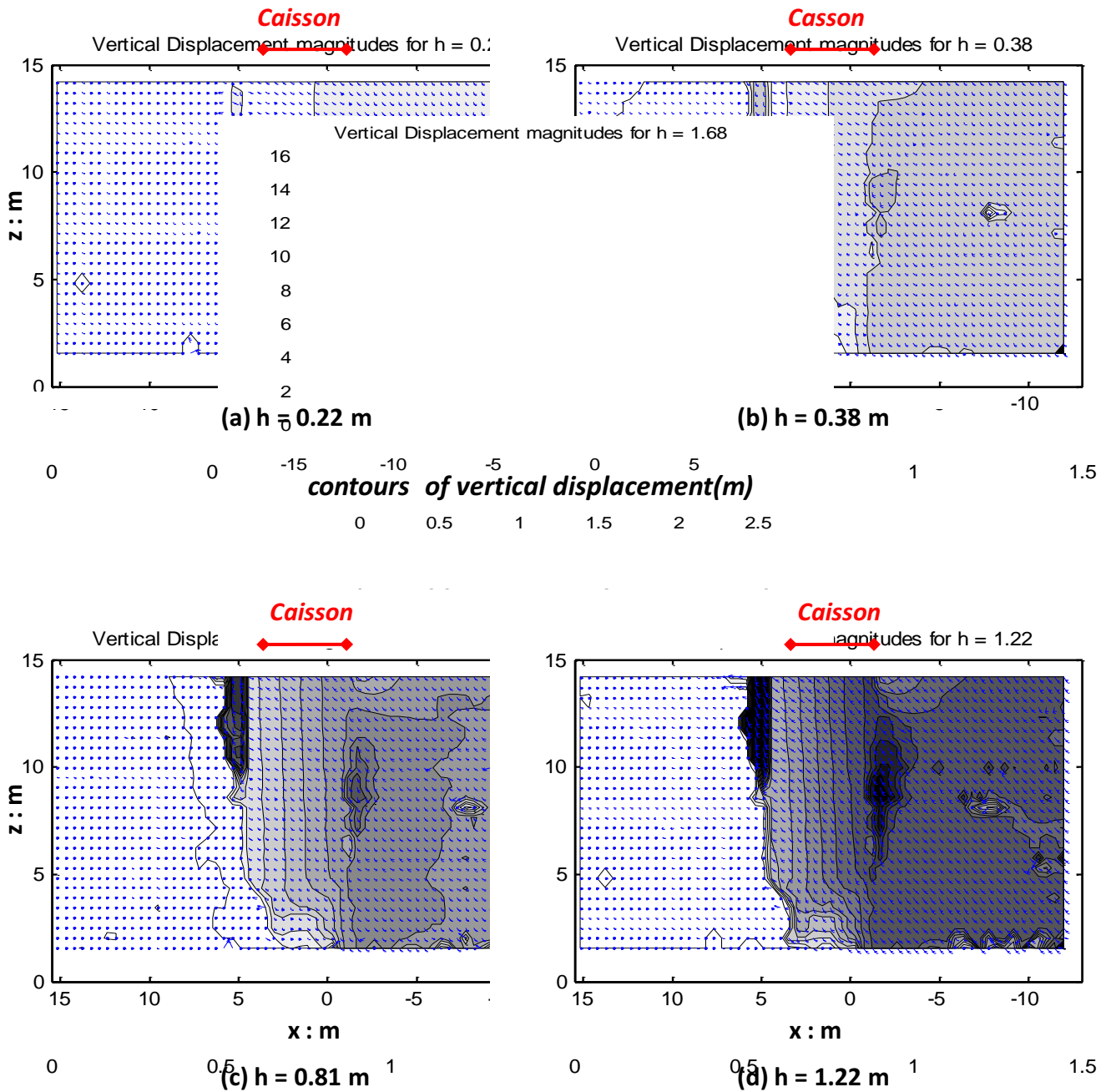


**Figure 5.11. Experiment** - Plot of the incremental displacement of the soil (black vectors) and the caisson (red vectors) in the  $x-z$  plane for different fault through levels, for the normal fault rupture scenario with the caisson  $s/B = 0.38$ .

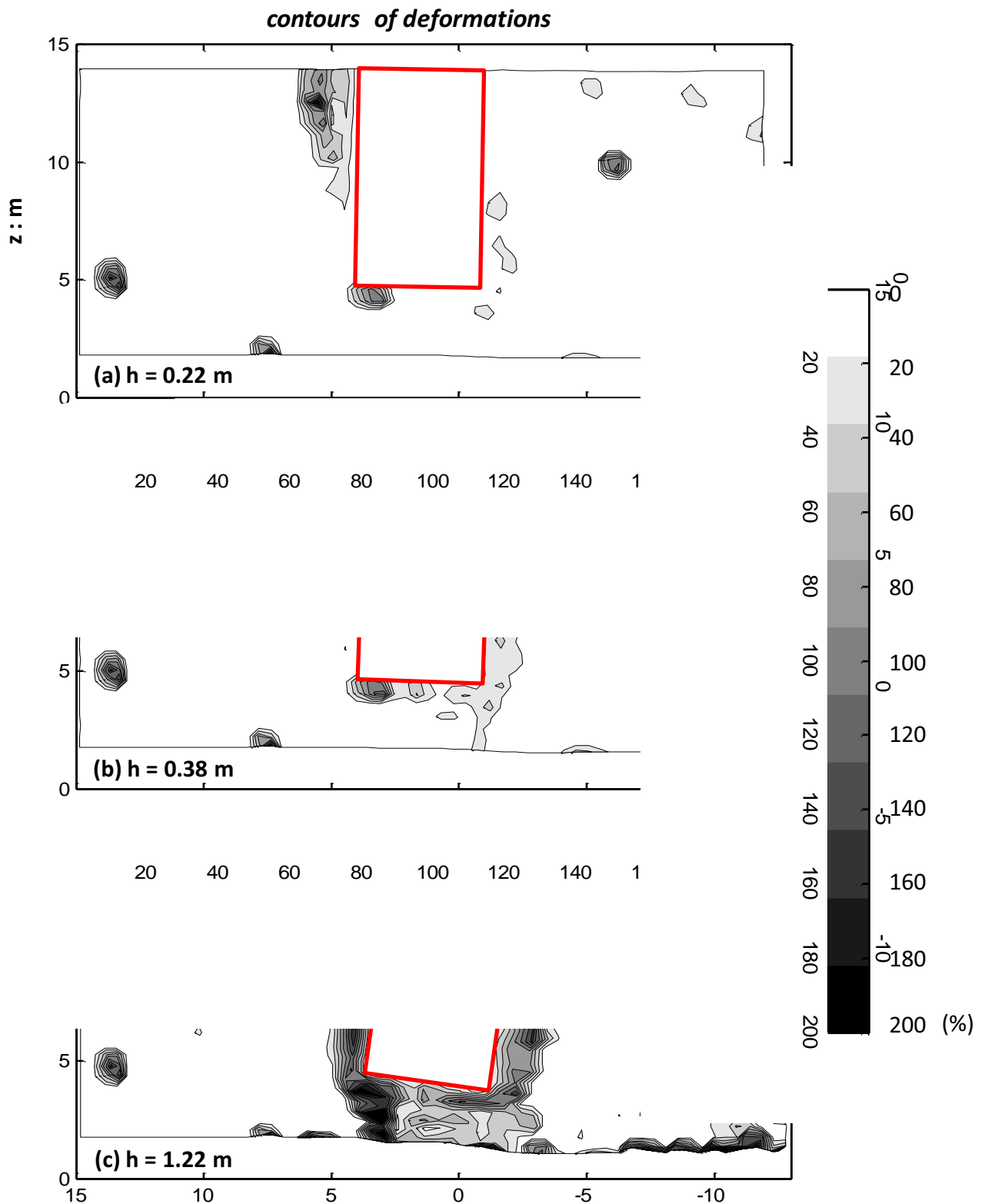


**Figure 5.12. Experiment** - Contours of the deformations in the deformed plane for characteristic values of the fault throw level. Normal fault rupture scenario with the caisson -  $s/B = 0.38$ .



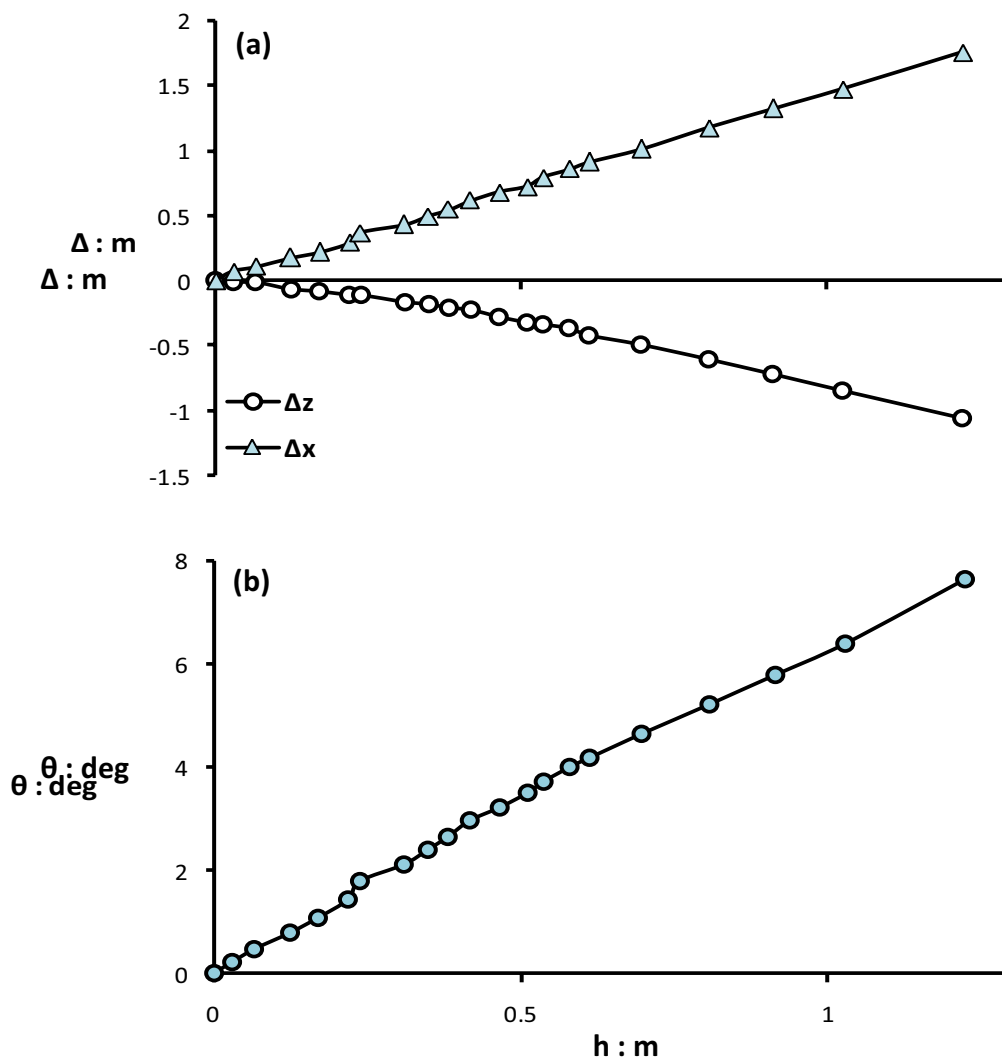


**Figure 5.13.** Evolution of (a) the Displacement and (b) the rotation of the caisson with respect to the normal fault rupture displacement,  $h$ . Reverse fault rupture scenario with the caisson -  $s/B = 0.38$ .

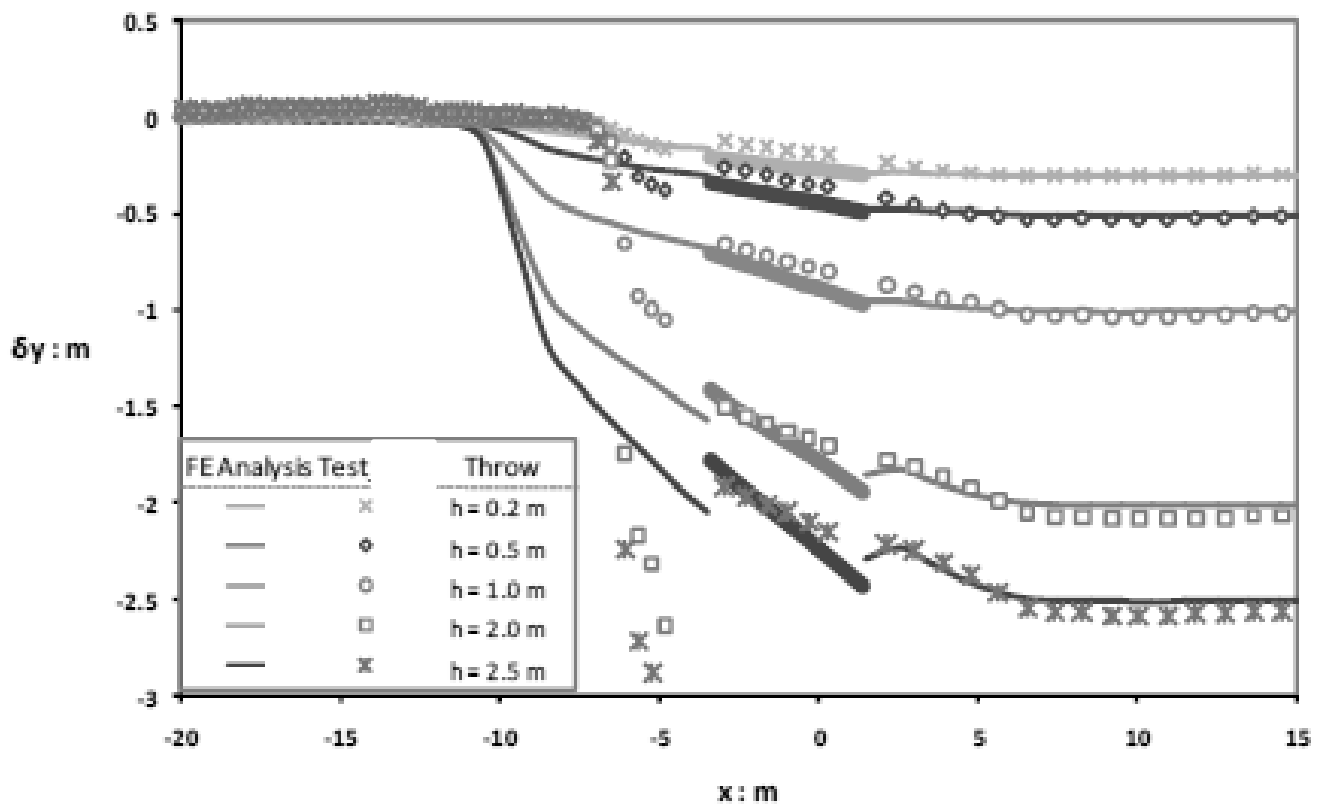


**Figure 5.14.** Comparison between numerical analysis and experimental results referring to the normal FR propagation in the scenario of  $s/B=0.38$ : vertical displacements of the model surface with respect to the horizontal position for different fault throw values.

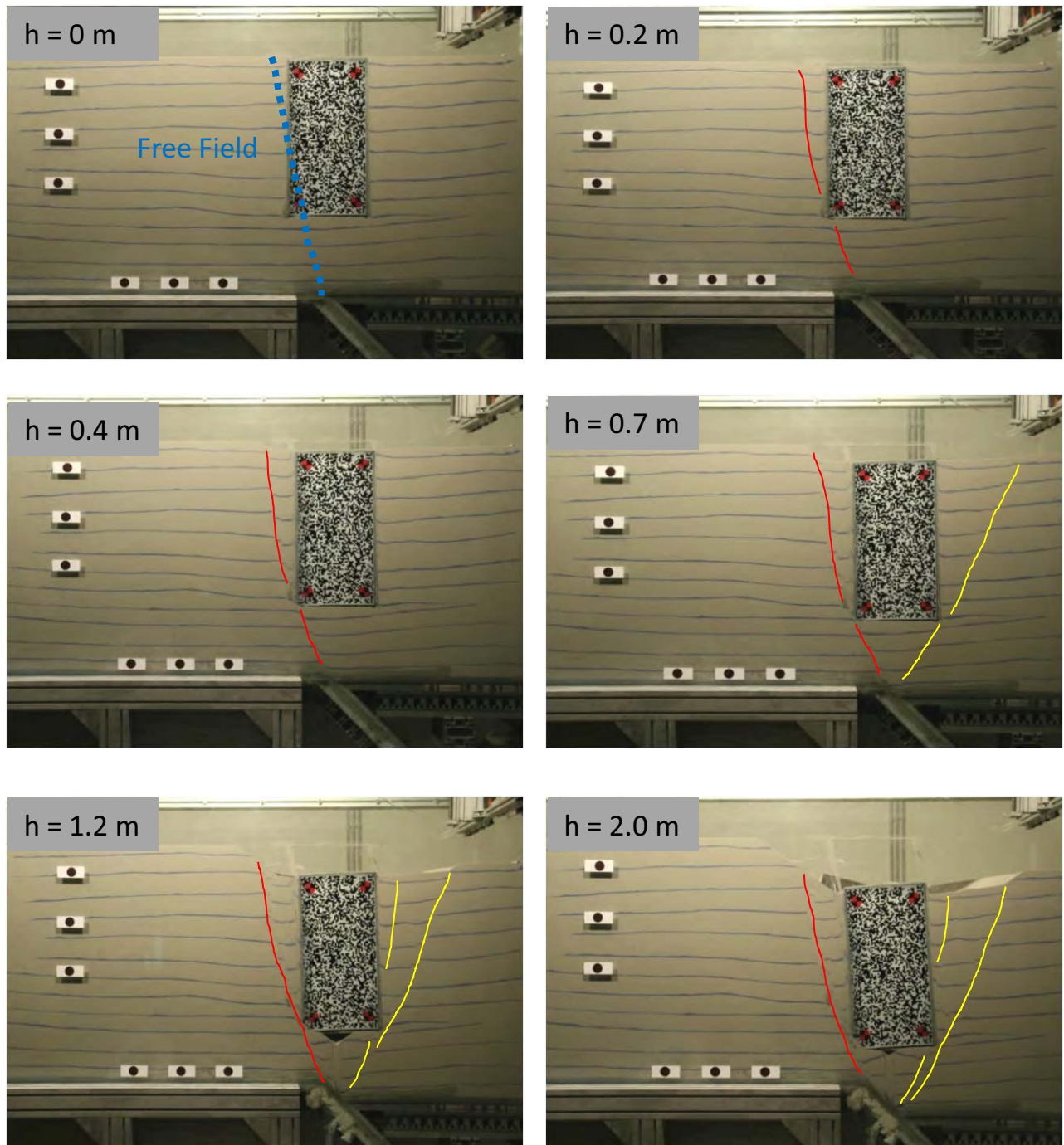


**Figure 5.15a. Experiment** - Snap-shots of soil and caisson deformation at characteristic values of the induced fault rupture displacement  $h$  (prototype scale), for the normal fault rupture scenario with the caisson -  $s/B = 0.80$ . With red denoted the main fault rupture propagation through the soil and with yellow the secondary and the failure mechanisms, due to the displacement of the caisson.

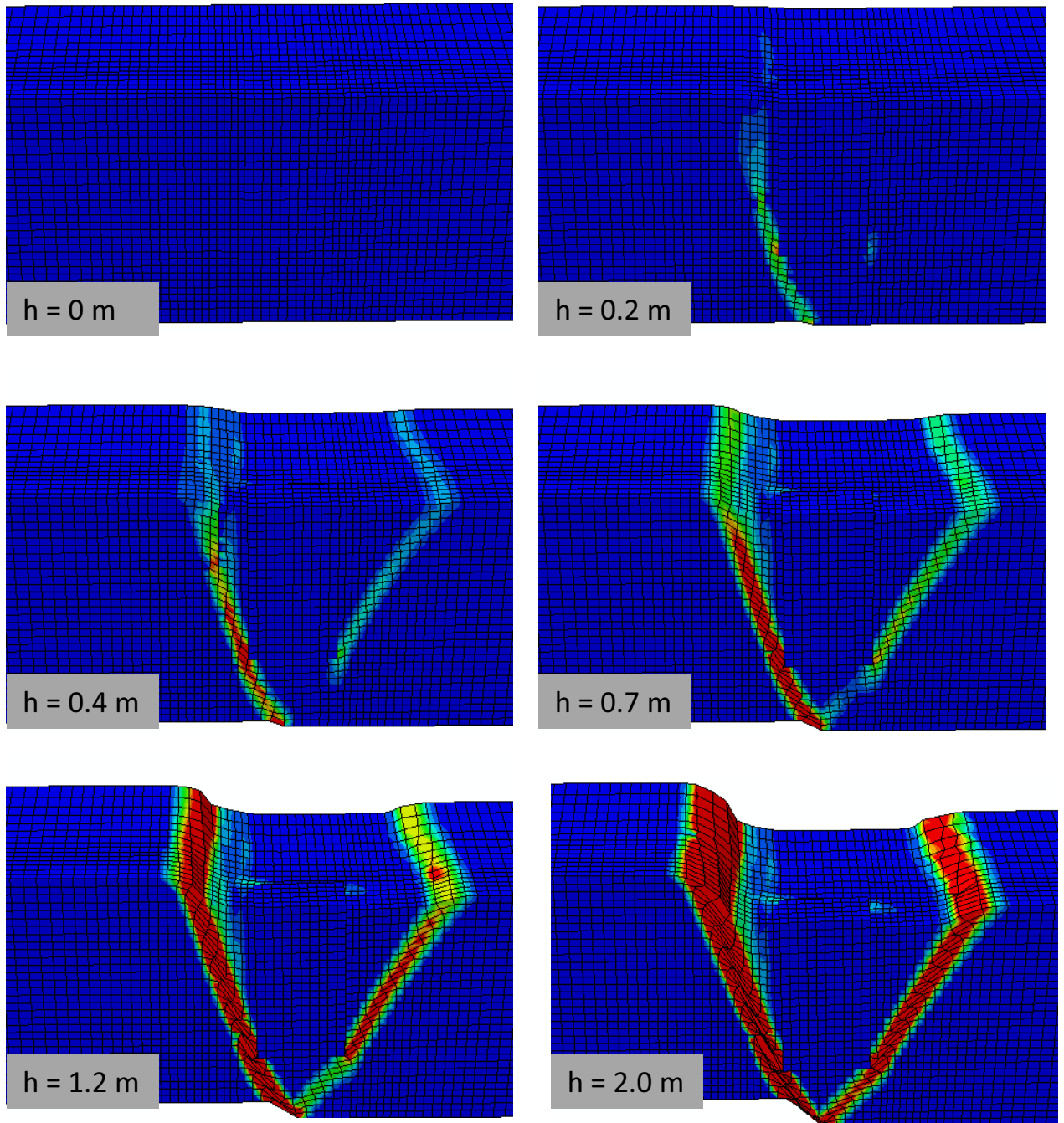


**Figure 5.15b. Analysis** - Snap-shots of soil and caisson deformation at characteristic values of the induced fault rupture displacement  $h$  (prototype scale), for the normal fault rupture scenario with the caisson -  $s/B = 0.80$ .

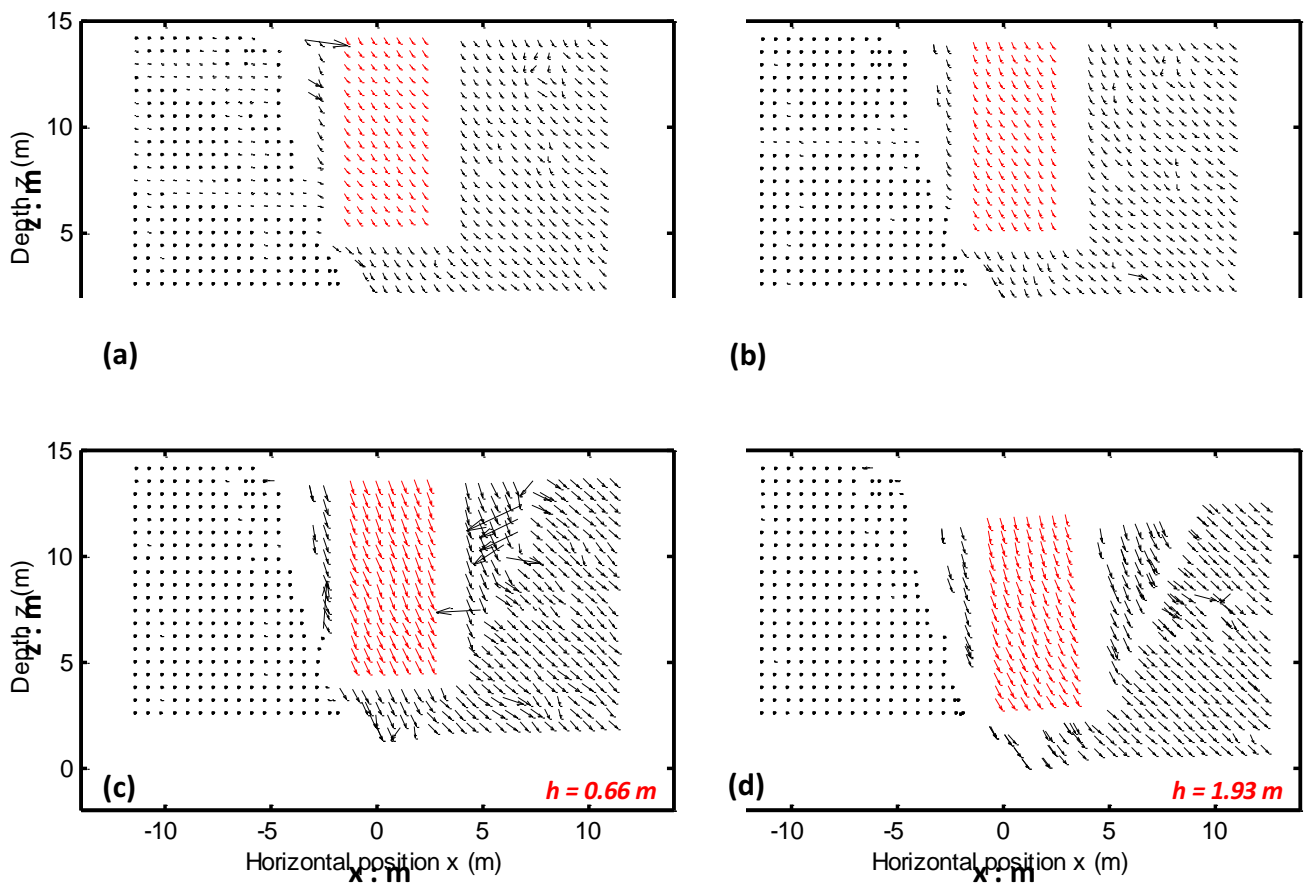


**Figure 5.16. Experiment** -Plot of the incremental displacement of the soil (black vectors) and the caisson (red vectors) in the  $x - z$  plane for different fault through levels, for the normal fault rupture scenario with the caisson -  $s/B = 0.80$ .

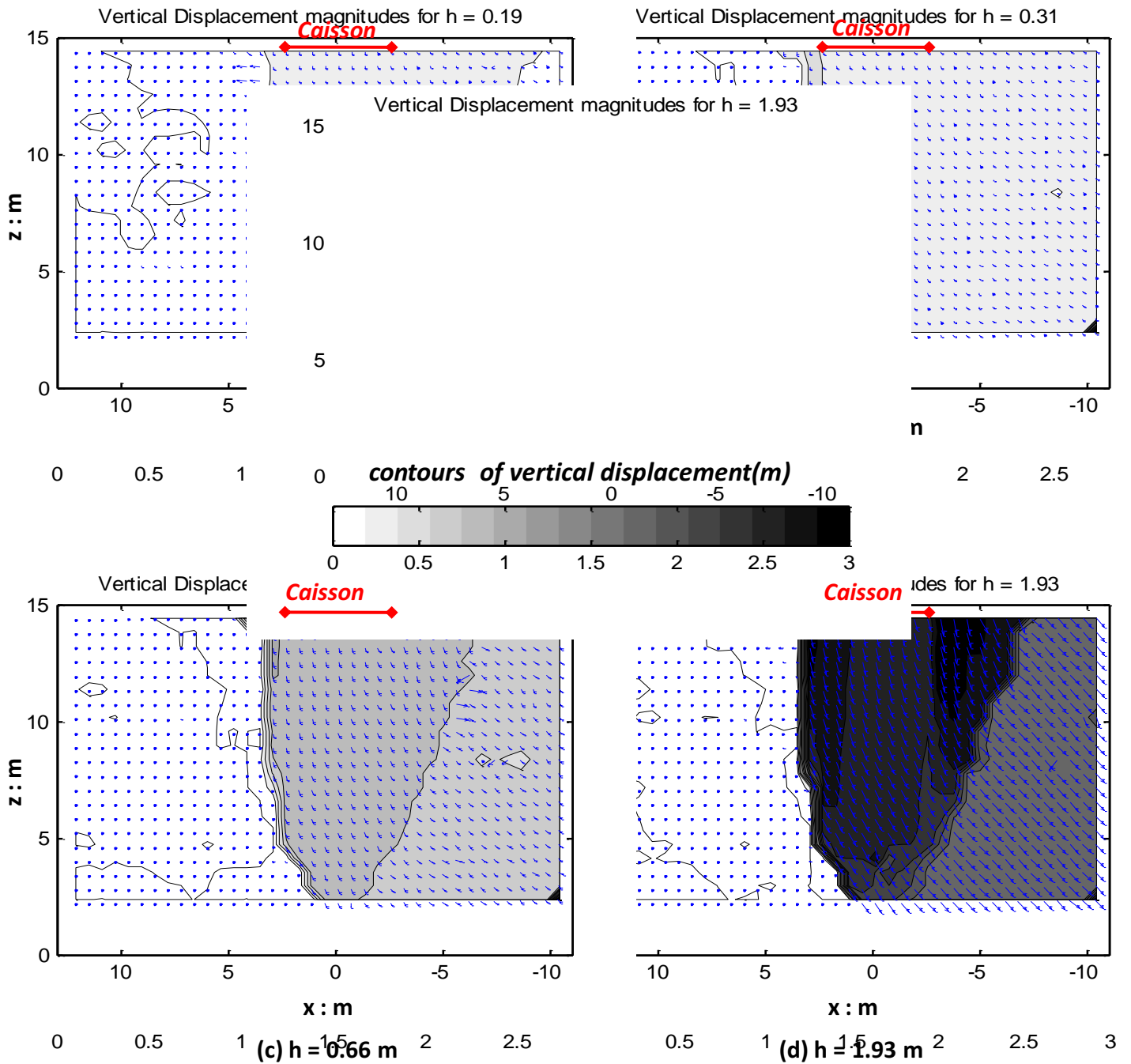


**Figure 5.17. Experiment** - Plot of the incremental displacement of the soil (black vectors) and the caisson (red vectors) in the  $x-z$  plane for different fault through levels, for the normal fault rupture scenario with the caisson -  $s/B = 0.16$ .

**contours of deformations**

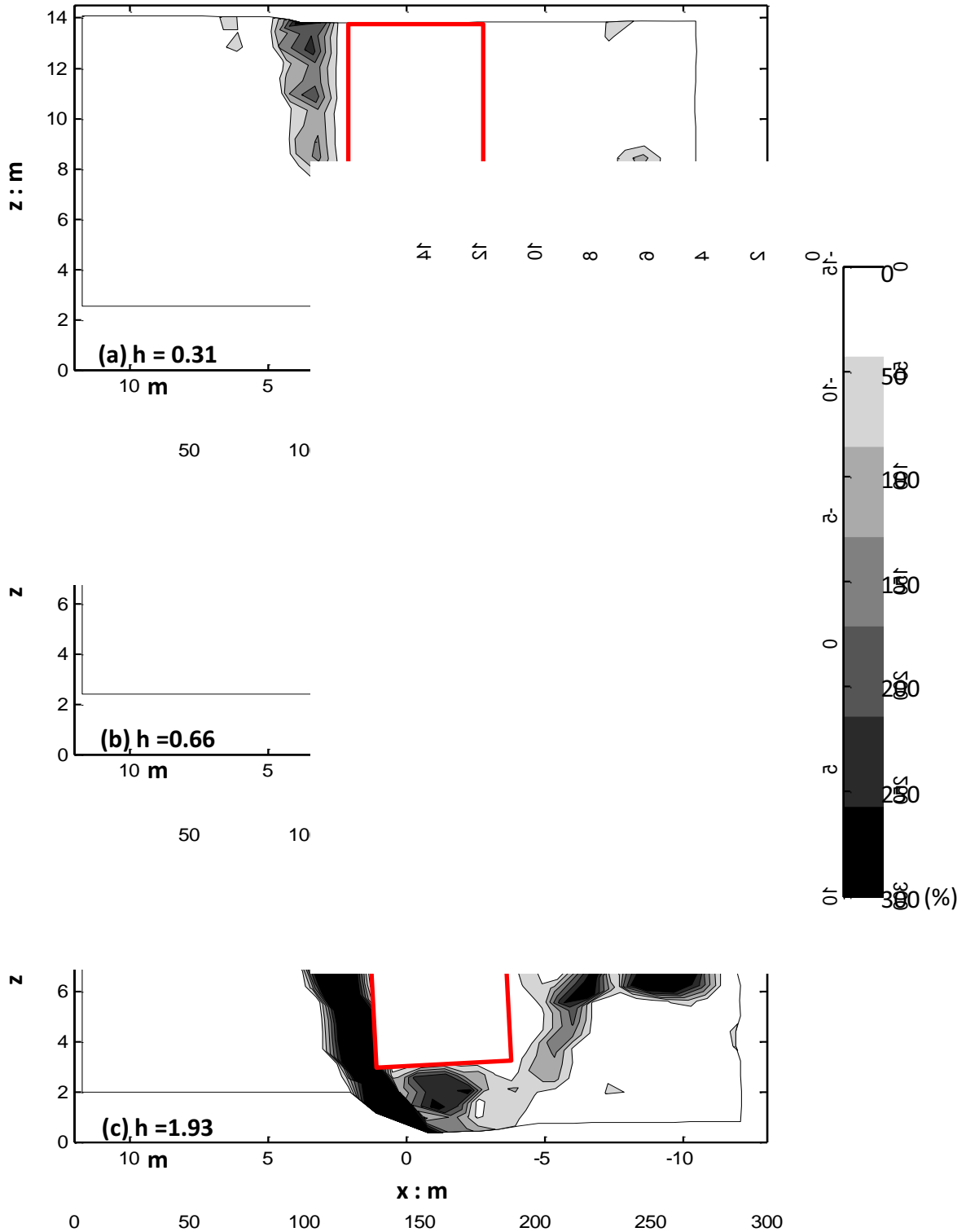


**Figure 5.18. Experiment** - Contours of the deformations in the deformed plane for characteristic values of the fault throw level. Normal fault rupture scenario with the caisson -  $s/B = 0.80$ .

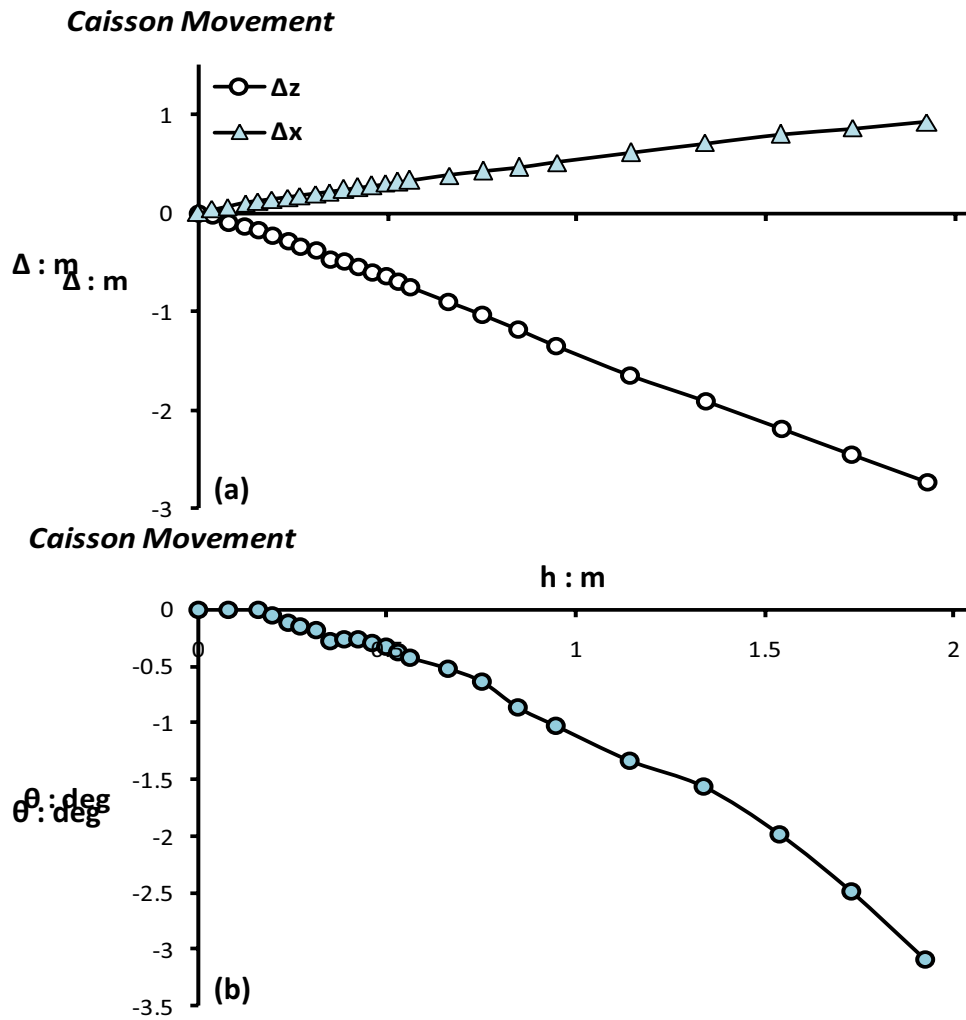


**Figure 5.19.** Evolution of (a) the Displacement and (b) the rotation of the caisson with respect to the normal fault rupture displacement,  $h$ . Reverse fault rupture scenario with the caisson -  $s/B = 0.80$ .



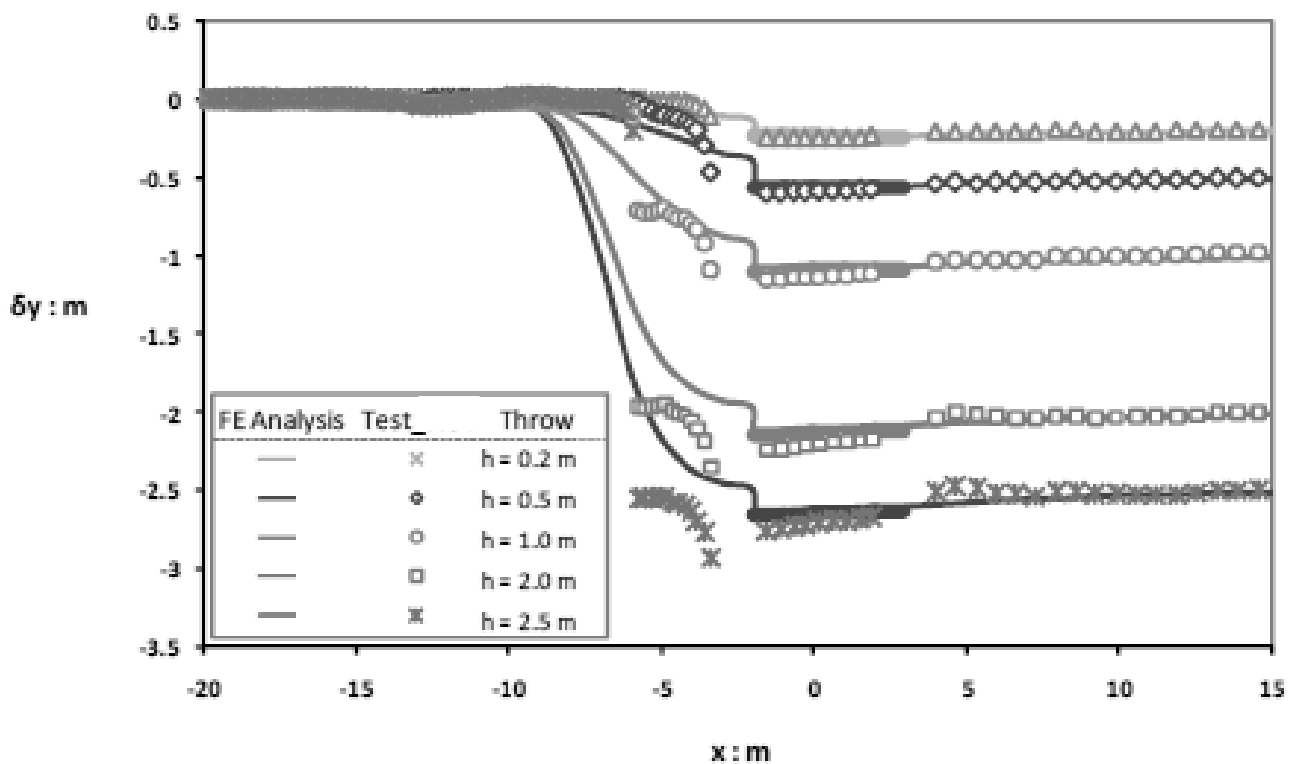


**Figure 5.20.** Comparison between numerical analysis and experimental results referring to the normal FR propagation in the scenario of  $s/B=0.80$ : vertical displacements of the model surface with respect to the horizontal position for different fault throw values.



# *Chapter 6*

## REVERSE FAULTING

## 5.1 INTRODUCTION

As in the previous chapter, but in this one for the reverse fault case, here are presented the case of reverse fault rupture propagation both in the free field case and the scenarios of three different positions of the caisson foundation relative to the fault outcropping. The results are given for the four reverse fault 1-g tests in terms of: (i) deformations and strain localizations within the soil body (i.e. failure mechanisms), (ii) surface displacement profiles and (ii) foundation displacements ( $u$ ,  $v$ ,  $\theta$ ). Moreover, the results of the equivalent numerical analyses are juxtaposed and compared side by side, demonstrating the similarities and some diversions and proofing the effectiveness of the numerical method in capturing the different components of fault rupture propagation in the free field and the FR-SFSI.

The parameter examined is the effect of the foundation position relative to the fault ( $s/B$  and  $x/B$ ), as all other soil and geometric parameters are kept constant, and therefore it was considered essential to study the evolution of the phenomenon in the free field before proceeding to the study of the FRSFSI mechanisms.

## 5.2 FREE FIELD

**Figure 6.1a** shows images of the soil model captured during the free field reverse fault test at different levels of base offset (throw). The soil response in every case is indicated through plots of incremental displacements and contours of shear strain, which are displayed in the following figures, **Figure 6.2 – 6.4**. It should be noted that for all graphs

presented in this chapter, the horizontal position axis ( $x$ ) is plotted in such way that zero point represents the position of the fault initiation at the “bedrock”.

For fault throw  $h = 0.6$  m there is a quite obvious gradual deformation of the soil surface on the side of the hanging wall. Although there is no visible strain localization, a wider failure zone can be identified in the image, which starts from the fault application point and propagates towards the soil surface within approximately the  $1/3$  of the soil specimen. This is also indicated by the strain contours, which show a low strain shear zone propagating towards the soil surface but not a distinguishable failure plane. After 0.4 m of additional fault throw ( $h = 1.0$  m) a displacement discontinuity (scarp) appears on the surface at a horizontal distance of about 16 m from the fault initiation point and the shear failure zone is visible throughout the soil layer. The shear failure is again distributed to a soil zone rather than a distinct surface. On further fault displacement ( $h = 1.4$  m) the shear failure zone localizes forming a second distinct failure plane which is indicated by the yellow lines. As the deformation continues the failure planes become more distinct; the shear failure is localized and the zone in between the two clearly shaped shear failure planes experiences smaller shear deformation (until  $h=2$ m). After  $h= 2.0$ m the zone appears to have smaller shear failure zones, but at this point the imposed deformation is very important and the failure zone is enveloped inside the two initial failure planes; the zone tends to widen up as the imposed deformation increases, but the failure pattern does not change.

The above described results agree with field observations of reverse fault rupture and its “typical failure patterns” reported in the literature (e.g. Bray et al., 1994a). The dip of a reverse fault rupture is expected to decrease as the failure propagates towards the soil surface and indeed this seems to be the case for the presented test. The rupture plane follows the bedrock dip angle ( $45^\circ$ ) for the first approximately 6 m of soil and then decreases progressively as it propagates towards the surface.

Very similar, at least qualitatively, is the behavior of the soil model in the numerical analysis. **Figure 6.2b** illustrates the numerically derived soil response for the same problem, in order to facilitate the comparison between numerical and experimental results. The response is shown in terms of mesh deformations and associated plastic strains. In accordance to what was the case earlier, there is no plastic deformation reaching the soil surface for less than 0.5m of fault displacement. The fault reaches the surface for  $h = 0.8$  m and a distinct failure plane is formatted when the fault throw doubles ( $h = 1.5$  m). In this case the first and the second failure planes are not easily separated, but it is encouraging that the shear deformation zone is of the same order in width. The reader can also, once more, recognize the tendency of the failure plane to bend over the footwall. Moreover, there is a difference in the horizontal distance that the fault outcrops (in the numerical analysis the fault emerges about 1.5 m further away to the left than in the 1-g test) the numerical analysis agrees with the experiment regarding the general failure pattern and evolution.

This argument is supported by Figures comparing **Figures 6.1 -6.3**. The shape of the numerically derived failure plane agrees very well with the

observed failure surface from the experiment. Also, the same behavior in terms of developed plastic strains can be noted. Indeed, the numerical analysis captures the general features (shape and width) of the failure mechanism for medium to large fault displacements. The agreement is less satisfactory for lower fault displacements (for example for  $h = 0.6$  m) where the experimentally derived shear failure zone seems to be more diffused. Even the results of the PIV analysis are very satisfying in terms of accuracy and localization of the failure planes and the mechanisms in general, despite the sensitivity of the results to the shortcomings of the experimental model and the quality of the captured images.

Although the comparison is satisfactory in terms of the failure surface shape and the evolution, some differences can be noted; the numerical analysis seems to underestimate the magnitude of shear deformations and localization, but the experiment due to the insufficiently simulated stress conditions allows for spread of the shearing zone in a wider area. This is a rather expected outcome, as unavoidable limitation of the numerical analysis in modeling the post peak soil behavior. The shear band width (developed during the post peak – softening – soil behavior) is overestimated due to the relatively large finite element width resulting in lower strain values. The comparison between numerical analysis and experiment in terms of vertical displacements ( $\delta y$ ) along the soil surface and the surface gradient ( $\beta$ ) occurring at different levels of fault throw is illustrated in **Figure 6.4**. The numerical analysis seems to capture the general trend of behavior. Although there is an offset of the displacement curves to the left, the position of maximum gradient and hence the point of maximum relative vertical displacement is approximately the same. The numerically predicted surface gradient is

higher, while there is a more scattered displacement profile especially in the case of large fault throw values (over 0.5 m). This is related to the previously discussed shortcomings in modeling the shear band zone width and the consequent underestimation of the localization of displacement discontinuities. That is why the comparison is better for small fault displacements (see curves for  $h = 0.2$  m) when most of the soil deforms elastically.

It should be noted that as the depth increases the shorter rupturing path (only 5 m above the fault application point), is going to favorably affect the discrepancies between the analysis and the experiment, although the same pattern will be followed.

### 5.3 REVERSE FAULT RUPTURE – CAISSON INTERACTION

As it has been well reported in the literature introducing the caisson – system is expected to modify the fault rupture path within the soil and the response is controlled by the parameter  $s$ , which indicates the caisson position relative to the fault. In the case of the embedded foundation it is considered more appropriate to determine the parameter  $s$  with reference to the fault induced displacements at the foundation base level ( $z = -10$  m). The distance  $s$  is calculated with reference to **Figure 3.1** and **table 3.1**. The relative to the fault caisson position is in each case indicated with reference to the aforementioned parameter ( $s$ ). It is important to notice that there is a difference in  $s$  of the order of 0.2m in some case between the experiment and the analysis. This is quite likely to cause some differences in the comparison



of the equivalent numerical analysis results with the three 1-g tests, but will not affect at all the qualitative conclusions.

### 6.3.1 Test 1 - RFR: $s/B = 0.66$

In this test the caisson foundation was positioned so that its right corner would be 1 m away (to the left) from the fault bedrock application point. In this way the free field fault rupture would cross the caisson base 2 m to the left of its right corner ( $s/B = 0.66$ ), as shown in **Figure 6.5a**. Figure 6.5a shows a set of images captured at different – characteristic time points during faulting. The fault rupture propagation is diverted by more than 8 meters to the left side of the caisson, from where the trace of the rupture on the surface has appeared in the free field scenario. Thus the hanging wall is wider spread as for the case of the free field. Although the shearing has started to localize, well before the imposed deformation reached 0.3m, at which point it hits both the caisson base corners, thereafter large accumulative deformation is required before the rupture trace appears on the surface ( $h=1m$ ). As shows the deformation of the soil is extensive and a narrow shear zone can be seen to propagate almost vertically towards the soil surface on the right of the caisson (on the hanging wall). Nevertheless, this shear strain plane does not reach the surface, rather than it pushes the caisson's bottom right corner up, thus forcing the caisson to rotate. On account of the fact that the main shear strain plane that reaches the surface diverted by the caisson to its left, if it was not for this secondary rupturing path, the caisson foundation would just move upwards with the rest of the hanging wall. Under the foundation base, there is a

wedge shaped, by the base of the caisson and the two characteristic rupturing planes; nonetheless no visible strain localization takes place. Until five meters from the surface the rupture propagates diverted, with almost a constant dip angle of 37 degrees (recall the imposed dip angle at the base of the model is 45 degrees). Afterwards, the dip decreases more ( $\sim 20^\circ$ ) and bends over the footwall (as theoretically anticipated). This mechanism justifies the surface trace being almost 10m (for  $h=3.5\text{m}$ ) more distant from the wall in comparison with the free field case or more than 23m from the fault application point. At the same time a more diffuse shear zone propagates towards the soil surface almost vertically on the right side of the caisson (hanging wall). No significant sliding displacements occur along the soil–caisson interface on this side as can be approximately estimated from the amount of the blue lines dislocation. These remarks are indicative of the determinative effect of FRSFSI. In simple words one could say that the free field rupture seems to have split into two failure planes (bifurcate), one on each side of the caisson, in order to avoid the rigid caisson body. The incremental displacements of the soil and the caisson at different fault throws shown in **Figure 6.6** indicate that the two failure mechanisms described above occur and develop at the same time. The failure mechanisms (identified by the discontinuities of the incremental displacements) agree in general with the above image observations and are highlighted with the blue dotted lines. In accordance with the experimental results, the numerical analysis indicates the development of two failure mechanisms, one on each side of the caisson (fault diverted to the left of the caisson and sliding plane along its right side), as shown by the plastic strain contours in **Figure 6.5b**. The agreement with the experimental results is quite

satisfactory and the numerical method seems to capture the FRSFSI mechanisms taking place. In the numerical analysis the imposed deformation for the rupture to reach surface is even larger,  $h \sim 1.5m$ . The image shown captured at 3.5 m of applied fault throw, reveals the generation of the two failure mechanisms from the free field rupture due to its interaction with the rigid caisson obstacle. The comparison with the numerical analysis for the same fault displacement shows a qualitatively very similar behavior.

The effectiveness of the numerical method in capturing the FRSFSI mechanisms during this test is also demonstrated by the graph of **Figure 6.10**, which plots vertical displacements occurring along the model surface with respect to the horizontal position for different values of fault dislocation. The analysis results coincide with the experiment as far as the emergence point of the fault (on the left of the caisson) is concerned and capture with good accuracy the caisson movement and the heave formation on the right of the caisson. Hence, the surprisingly good agreement between analysis and experiment regarding the foundation rotation and displacements (**Figure 6.9**) comes as a reasonable consequence.

### **6.3.2 Test 2 - RFR: $s/B = -0.04$**

In this second reverse type FRSFSI test the caisson was positioned on the left of the fault initiation point in a way that the free field rupture would hit the right sidewall of the caisson on the lower half part ( $s/B = -0.04$ ). **Figure 6.11a** depicts a set of six images captured during the test at characteristic points for different fault displacements. For noticeable

localization, fault throw of 0.3m is required, at which point the rupture has not even reached the caisson. At 0.7m, the fault throw is more than double as before, the rupture hit the right bottom of the caisson and has been split. Hereafter, there is rupture propagation on the right side of the caisson and another starting from its left bottom corner. The main remark from this experiment is that none of these paths reaches the surface intact, not even after base displacement of 2.0m. The only surface trace is that in the close vicinity of the upper right corner of the foundation, result of sliding between the foundation and the surrounding soil and of the double bifurcated initial rupture. The initial rupture that hit the caisson on its corner, has been forcing it to be displaced and rotate towards the left side. This kinematic behavior of the caisson combined with the fault rupture propagation creates a complex mechanism, hybrid of the shear strain failure due to the rupture and the bearing capacity (on the left side of the caisson – due to its counterclockwise rotation of the caisson and due to its movement to its left) of the soil. That is the case on the left of the caisson. After the first bifurcation, to the right there is another shear strain plane created that hits the caisson at the middle of the right side and then again bifurcates creating a similar rupture path that reaches the surface. It is remarkable that these mechanisms begin to be evident for fault throws larger than 1.5m. The aforementioned are supported by also by the PIV results, **Figures 6.12-6.13**: the first and second bifurcation of the initial rupture, the sliding on the right side of the wall and the complex mechanisms on the left and right sides of the caisson.

As far as the comparison with the numerical analysis' results is concerned, there are both differences and similarities. First of all, the

rupture path reaches again first the bottom right corner and is partitioned in two parts, one to the right and one to the left of the foundation. The left one crosses the bottom left corner before it continues its way to the surface. Another similar feature is that the fault throw required for the aforementioned to take place is the same in both analysis and experiment. Nevertheless, there exists some important diversion from the experimental results, quantitative and qualitative. To the right of the caisson the rupture does not bifurcate and does not reach the surface, although as the fault throw increases the shear strain failure zone becomes respectively wider. To left right the diverted rupture continues its way and finally outcrops about 11m away from the caisson left corner, about double the distance as would be for the free field case. There is no shine of important passive failure, due to the rotation of the foundation. Instead it seems that after the rupture has reached the surface the caisson moves along with the hanging wall.

The same conclusions can be drawn also from studying the rotational and deformation history of the caisson, during either the experiment or the analytical simulation. The Figures 6.15 – 6.16 are most indicative of the comparative results and the differences emphasized above. On account of the fact that the stress level is a decisive factor that can control the evolution of the failure mechanisms, and considering that in the 1-g testing the main disadvantage of the simulation lies on the poor simulation of the stresses, one cannot be completely sure if the analysis' or the experiment's inherent disabilities are to solely is blame for these discrepancies. The true simulation of this, in any case idealized scenario, could lie somewhere in-between.

### 6.3.3 Test 3 - RFR: $s/B = -0.96$

**Figure 6.17** presents a set of images captured during **Test 3:  $s/B = -0.96$** . In this third test the caisson was positioned on the left of the fault initiation point in a way that the free field rupture would hit the right sidewall of the caisson on the top half part, which was taken before fault loading started ( $h = 0$  m). After 0.5 m of fault displacement there appears to be a gradual vertical deformation throughout the hanging wall (to the right of the foundation). There is some visible evidence of strain localization, but only for the first 3m from the level of the initiation of the fault outcropping, and an even shorter plane formed next to the top right corner of the foundation. This displacement discontinuity becomes more distinct on further faulting (0.7m) and a shear deformation zone can be seen to run from the bedrock dislocation point to the top right corner of the caisson. The failure strain is divided and localized in two shear planes, very close to one another. At the same time the caisson is unshakable. For fault throw values exceeding 0.7m the **Figures 6.16 – 6.20** indicate the formation of a shear band on the hanging wall side of the foundation, which propagates from the bedrock dislocation towards the soil surface in a similar to the free field rupture way until it reaches the caisson sidewall (almost to the top right edge). The stiff-rigid border of the caisson wall causes the rupture to divert vertically and emerge next to its right corner, thus sliding on the interface occurs. The width of the shear band is about 1.5m on the base of the soil layer, and as the propagation progresses it continues to have the same width. A distinct vertical sliding plane is eventually formed at

the top 5 m of soil, right next to the caisson. The failure mechanism is indicatively highlighted with the red dotted line in Figure 6.16 (and compared with the free field rupture (yellow dotted line)). Figure 5.9 illustrates the response of the soil and the caisson during the test through vector plots of incremental displacements at different fault loading stages giving proof of the previously identified failure mechanisms. To favor the comparison with the images of Figure 6.16 the vector plots refer to the almost the same values of fault throw. The diversion of the fault rupture to the right seems to “protect” the caisson from significant distress. The figure demonstrates that the caisson displacements are almost absent during all faulting stages and the same is the case for the soil on the footwall (to the left of the foundation). Moreover, not only does the foundation “avoid” the applied fault loading by experiencing very limited distress, but interestingly its incremental displacements are unnoticeable even for very significant deformation of the hanging wall. This is probably because the failure (softening) of the soil at the shearing plane long the caisson sidewall reduces the shear forces applied to the caisson wall compared to the forces at peak strength conditions. After the soil on that plane has reached its critical state there is no change on the magnitude of the applied shear stresses with increasing fault displacement.

The numerical analysis results are shown in Figure 6.16b in terms of plastic deformations occurring at different levels of fault displacement. Although there is a “delay” in the emergence of the localization on the surface (the localization appears on the right of the caisson for 0.7 m of fault dislocation in the experiment but not before the fault throw reaches approximately 1 m in the analysis), the numerical analysis seems

to capture the overall fault rupture – caisson interaction behavior: narrow zone of shear strain localization and almost firm in its initial position for the caisson. It can also be noticed that when the rupture reaches the surface the trace gives irrefutable evidence of rupture diversion. The effect of FRSFSI is highlighted, and the agreement between numerical and experimental results is evident. The effect of FRSFSI is quite significant causing more than 5m deviation of the surface rupture from its free field route towards the hanging wall.

**Figure 6.22** compares the numerical analysis with the experiment in terms of the vertical displacements occurring along the model surface for different values of fault dislocation. The blue lines stand for the numerically calculated displacements and the caisson area is highlighted with the thicker blue lines, whereas the red symbols stand for the experimental results. The agreement between numerical analysis and experiment is quite satisfactory for all fault throw levels. The only divergence between numerical and experimental results involves the slope of the heave emerging on the right of the caisson. The numerical analysis gives a significantly steeper heave because it doesn't allow for the soil on the heave to slide and flow around the foundation, which happens during the experiment. The caisson response is presented in **Figure 6.21** in view of the rotational and translational displacements occurring during the test with respect to fault throw and the results are compared to the numerical analysis. The comparison between the analysis and the experiment is very satisfactory for the case of the horizontal and vertical displacement evolution and for the caisson rotation primarily when large fault dislocations, exceeding 2 m, are



considered, but in general the displacement of the caisson is insignificant.

#### 5.4 SUMMARY

The reverse fault rupture propagation in the free field was studied and both numerical and experimental results regarding the failure surface pattern are in agreement with field observations and former research studies. With reference to the free field test, the mechanism of fault rupture–caisson interaction was investigated for three different cases of the foundation position relative to the fault. The rigid caisson was found to act as a kinematic constrain which caused diversion of the free field rupture. However, the mechanism and the direction of the fault diversion as well as its effect on the performance of the foundation varied impressively depending on the position of the caisson relative to the free field rupture:

- When the free field rupture crossed the upper right sidewall of the caisson the fault was deviated a bit upwards and more to the right, towards the hanging wall, leaving the caisson practically unscathed, with a maximum rotation almost zero at 3.5 m of fault throw. It is expected though that if the caisson was a little closer to the fault rupture initiation point it would have been more affected itself by the interaction, experiencing some more noticeable rotation.
- The fault–caisson interaction mechanism was more distinct in the case that the free field rupture crossed the caisson's base resulting in the generation of two failure planes (one in each side of the foundation) and significantly larger rotations. Equally important in

terms of rotation of the caisson is the case when the free field rupture path would cross the lower part of the right side of the embedded foundation. In both cases the rupture imposes deformation localized near the bottom right corner of the caisson leading to important rotation. Nevertheless, the mechanism in these two cases does not share any other common remark.

- Considering the relative position of the caisson either by taking into account the distance from the fault rupture initiation or the point that the rupture path in the free field would cross the foundation the surface outcropping can be diverted up to more than 20m from the caisson or can only be noticed due to sliding of the caisson as the rupture propagates almost parallel to the soil-foundation interface.

All in all, the comparison between the 1-g experimental series test and equivalent numerical simulations revealed the effectiveness of the numerical methodology in capturing the mechanisms of fault rupture–caisson interaction. Although the limitations regarding the modeling of post peak soil behavior resulted in the underestimation of shear strain localization and amplitude, the numerical simulations predicted more than adequately, in almost every case the general pattern of fault rupture diversion and/or bifurcation due to the presence of the caisson. Even quantitative agreement has been succeeded in many scenarios. With respect to the foundation's performance, the analysis was in agreement with the experiments as far as the translational displacements are concerned. The agreement was in some cases less satisfactory (and in other cases surprisingly good) regarding the foundation rotation with respect to fault throw. Nevertheless, the

numerical method proved capable of capturing the overall response with reasonable accuracy.

Once more, it should be noted that the stress conditions during the experiment are not even close to the real scale problem and this can have lead to some miss-prediction of the actual mechanisms. As the writer has gained experience both by following the traces of the theoretically anticipated results, concerning both analysis and experiment, it is believed that the overall full scale problem is realistically simulated. And although, the research and understanding this problem and it's numerical and experimental reproduction has not reached yet the high point, nonetheless both the analysis and the experimental procedure can be judged as important simulation tools for the real scale problem.

Both numerical and experimental results highlighted the determinative effect of the foundation position on the response of the soil-caisson system.



# Figures

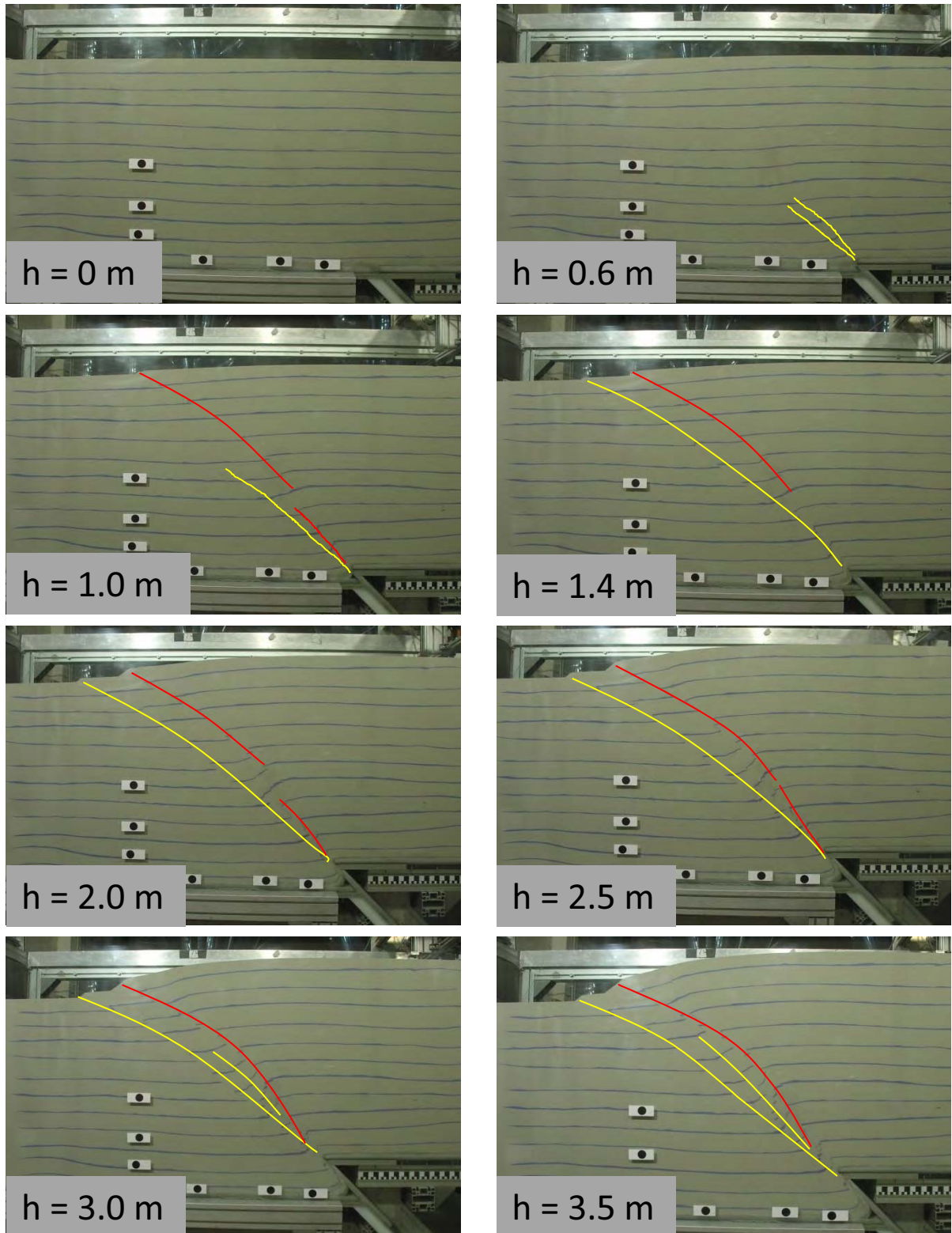


**Figure 6.1a Experiment** – Reverse Fault rupture propagation in the free field: Images of the deformed soil model, at eight characteristic different deformation steps, indicating the evolution of the fault rupture propagation and the mechanisms that appear.

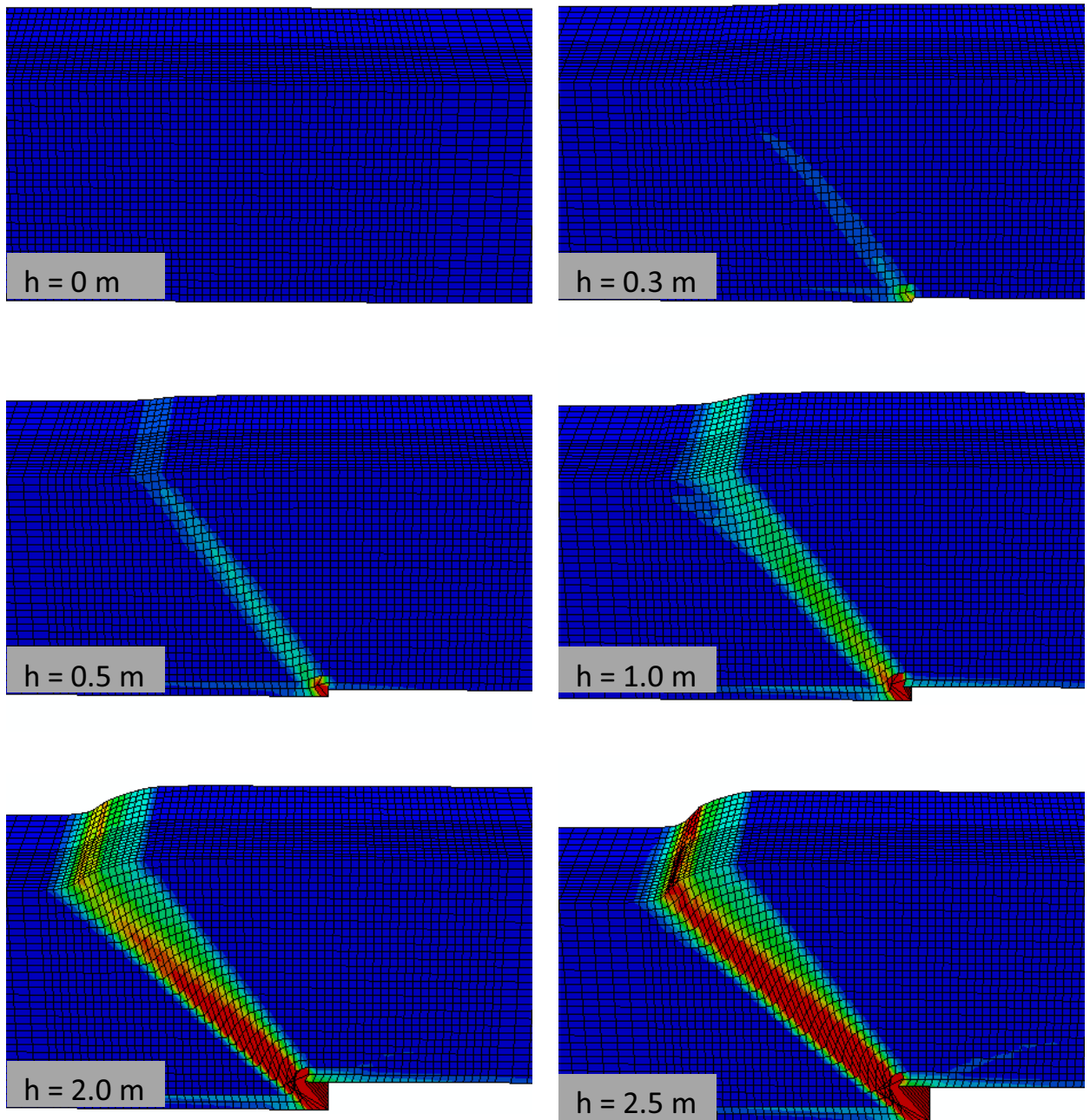


**Figure 6.1b. Analysis** – Reverse Fault rupture propagation in the free field: Images of the deformed soil model, at six characteristic different deformation steps, indicating the evolution of the fault rupture propagation and the mechanisms appeared.

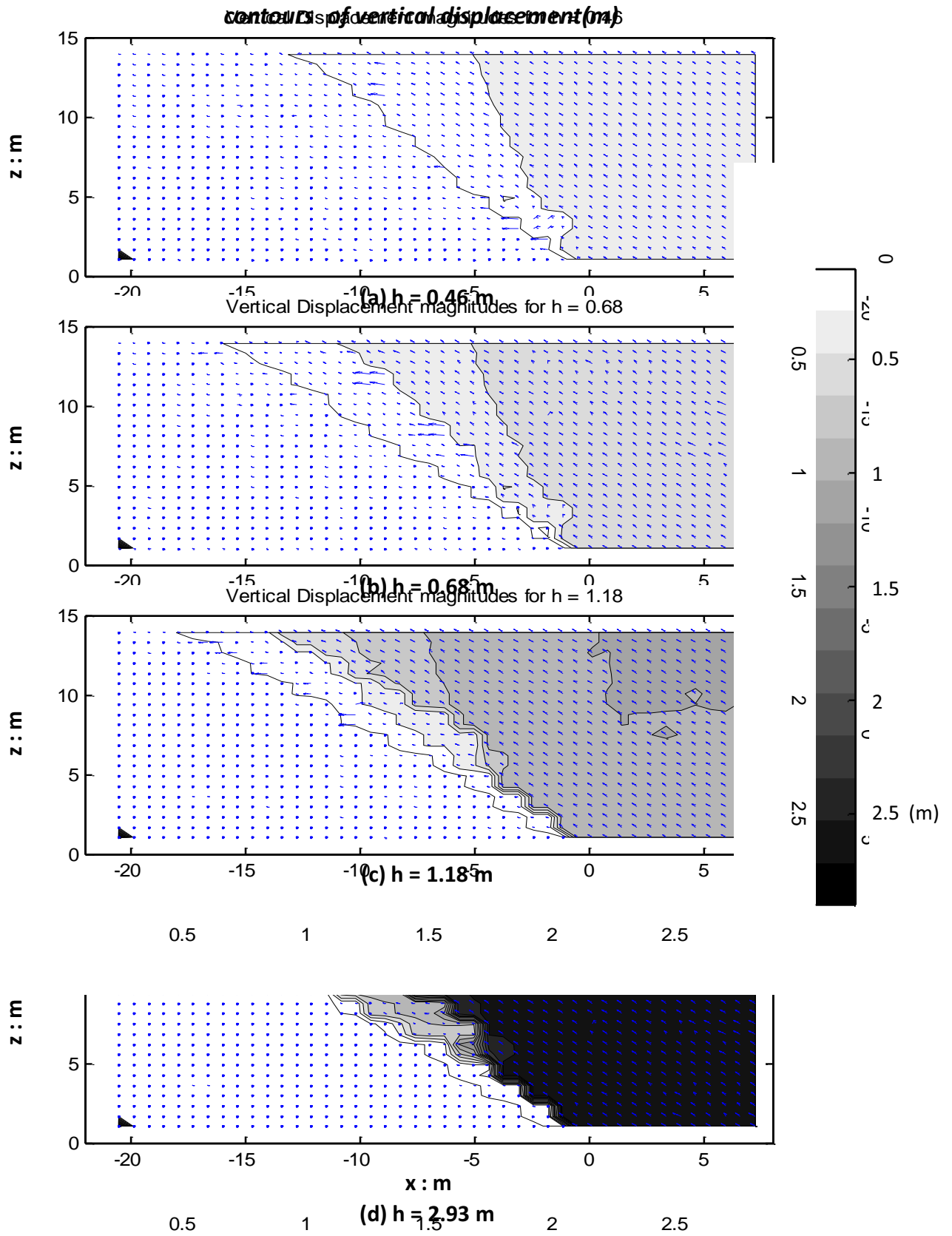


**Figure 6.2. Experiment** – Contours of vertical displacements in the undeformed geometry for characteristic values of the imposed tectonic deformation,  $h$ . Reverse Faulting –Free-Field.



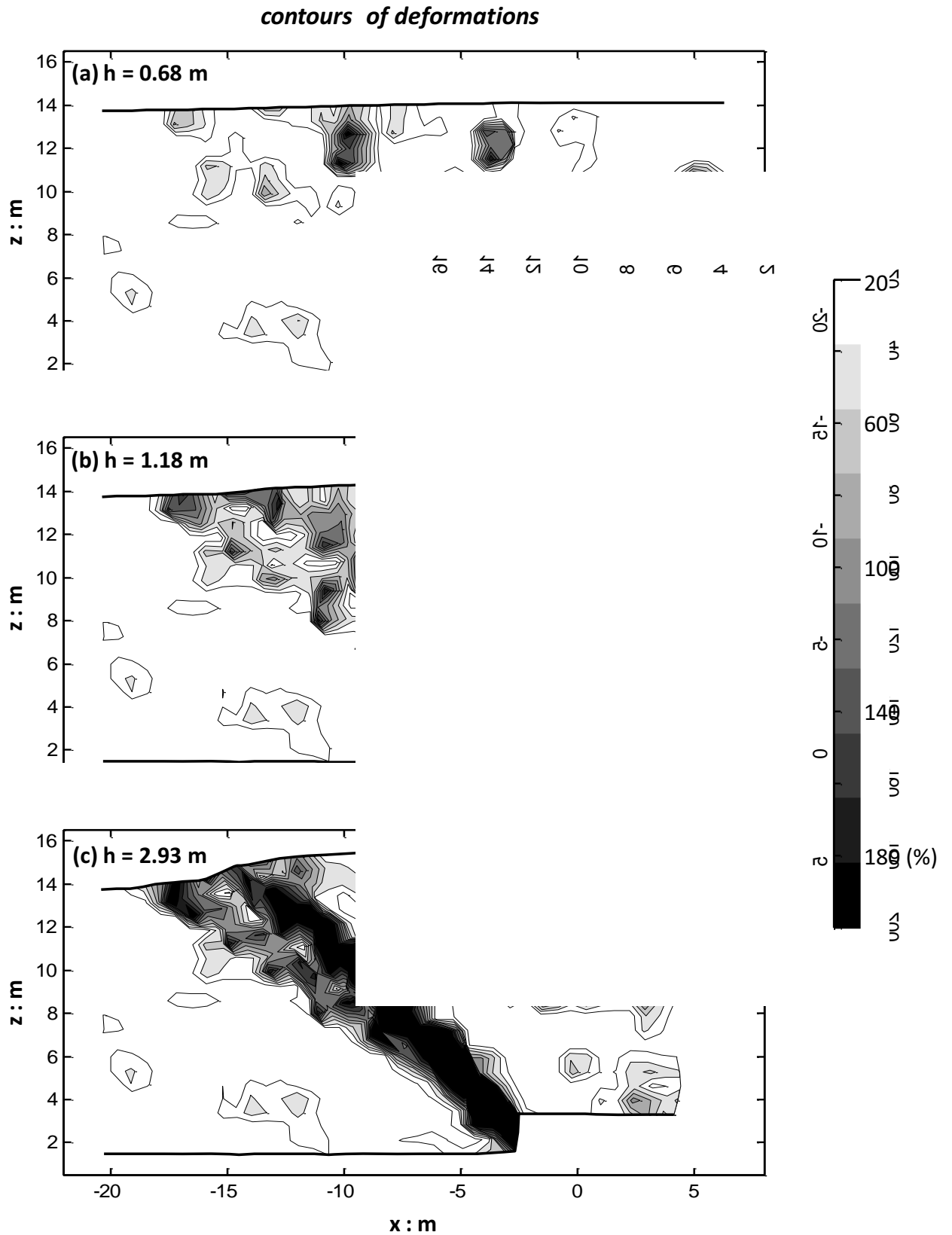


**Figure 6.3. Experiment** – Contours of deformations in the deformed geometry for characteristic values of the imposed tectonic deformation,  $h$ . Reverse Faulting –Free-Field.

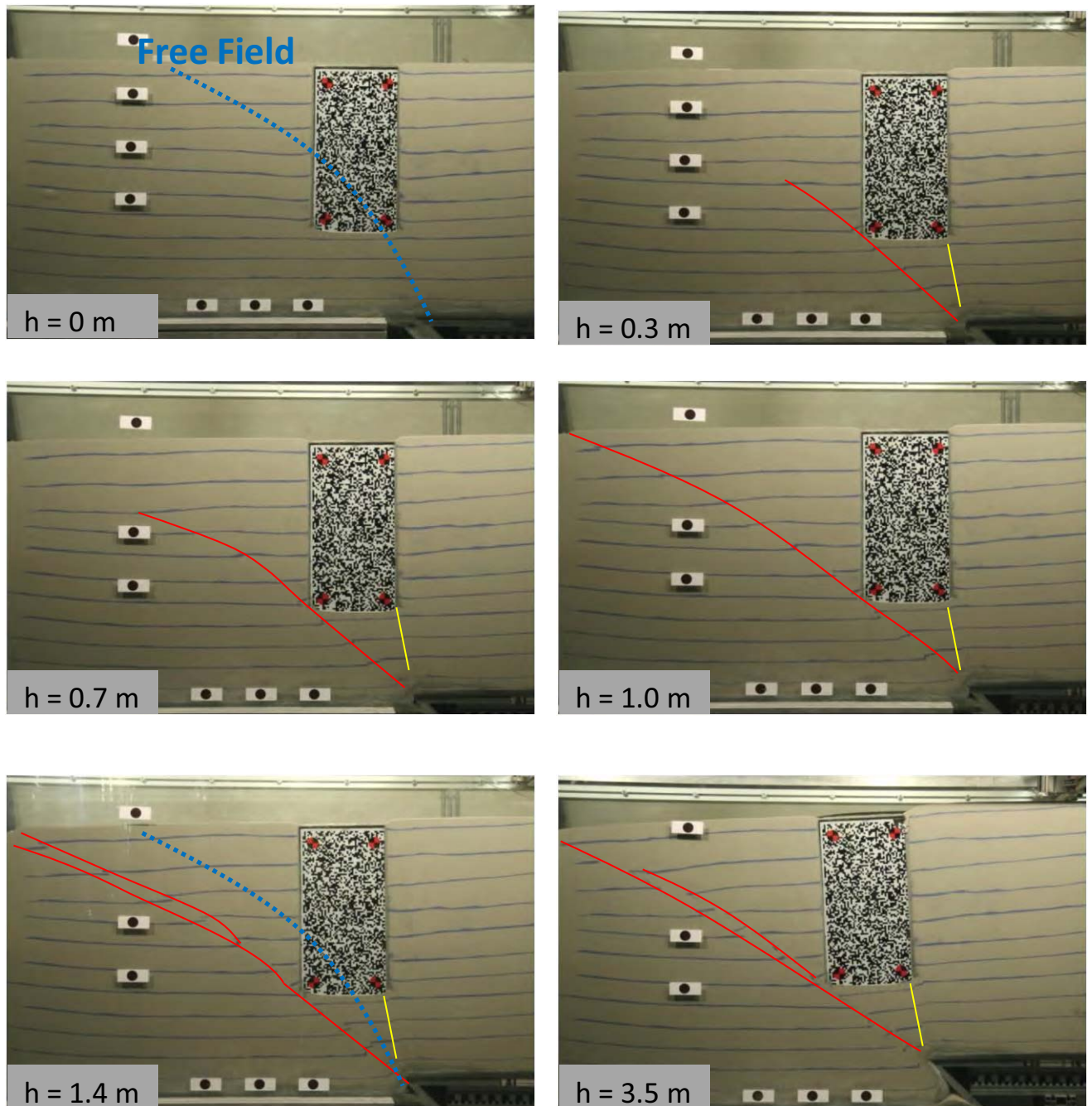


**Figure 6.5a. Experiment** - Snap-shots of soil and caisson deformation at characteristic values of the induced fault rupture displacement  $h$  (prototype scale), for the reverse fault rupture scenario with the caisson -  $s/B = 0.66$ . With red denoted the main fault rupture propagation through the soil and with yellow the secondary.

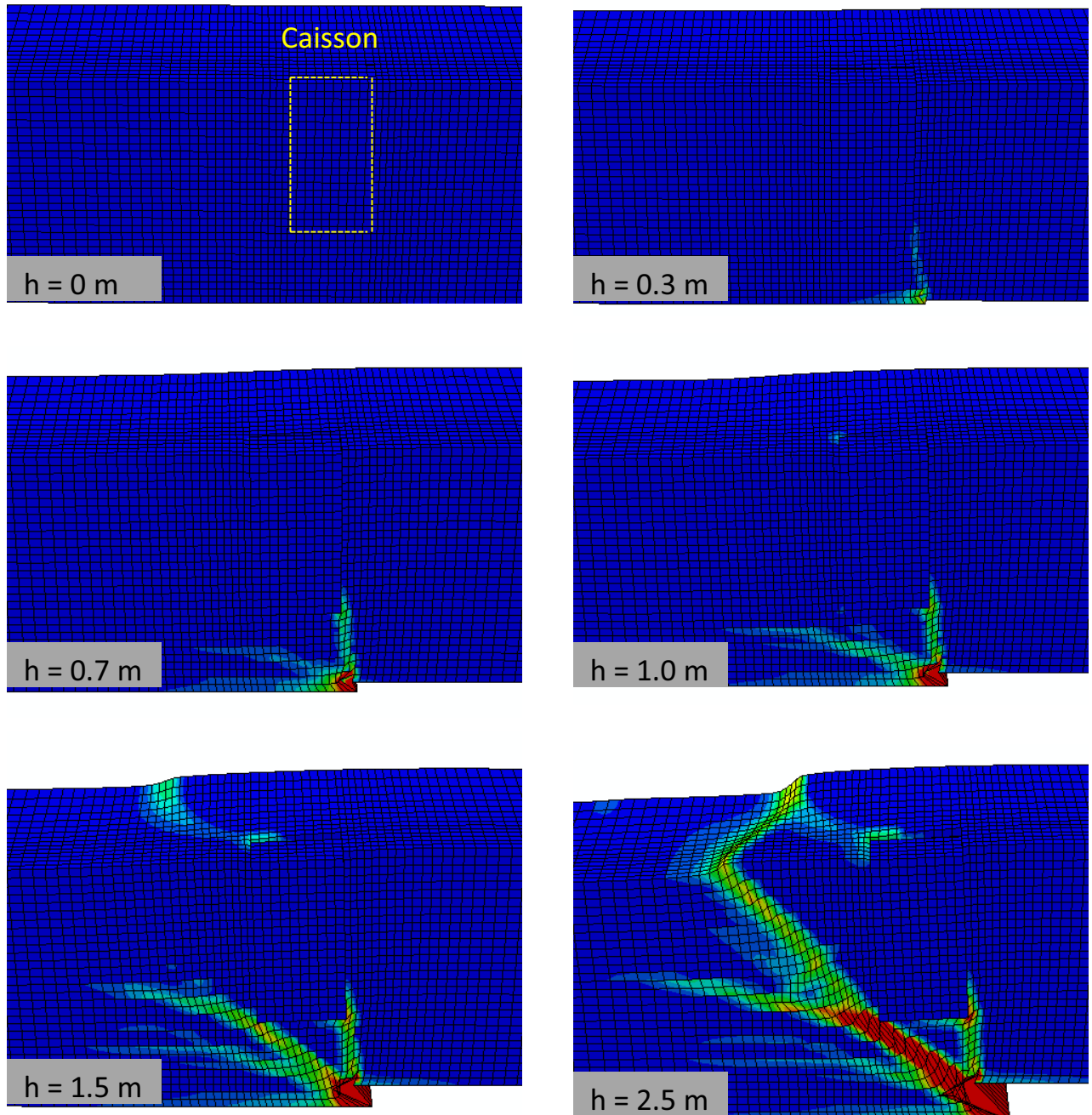


**Figure 6.5b. Analysis** - Snap-shots of soil and caisson deformation at characteristic values of the induced fault rupture displacement  $h$  (prototype scale), for the reverse fault rupture scenario with the caisson -  $s/B = 0.66$ . With red denoted the main fault rupture propagation through the soil and with yellow the secondary.

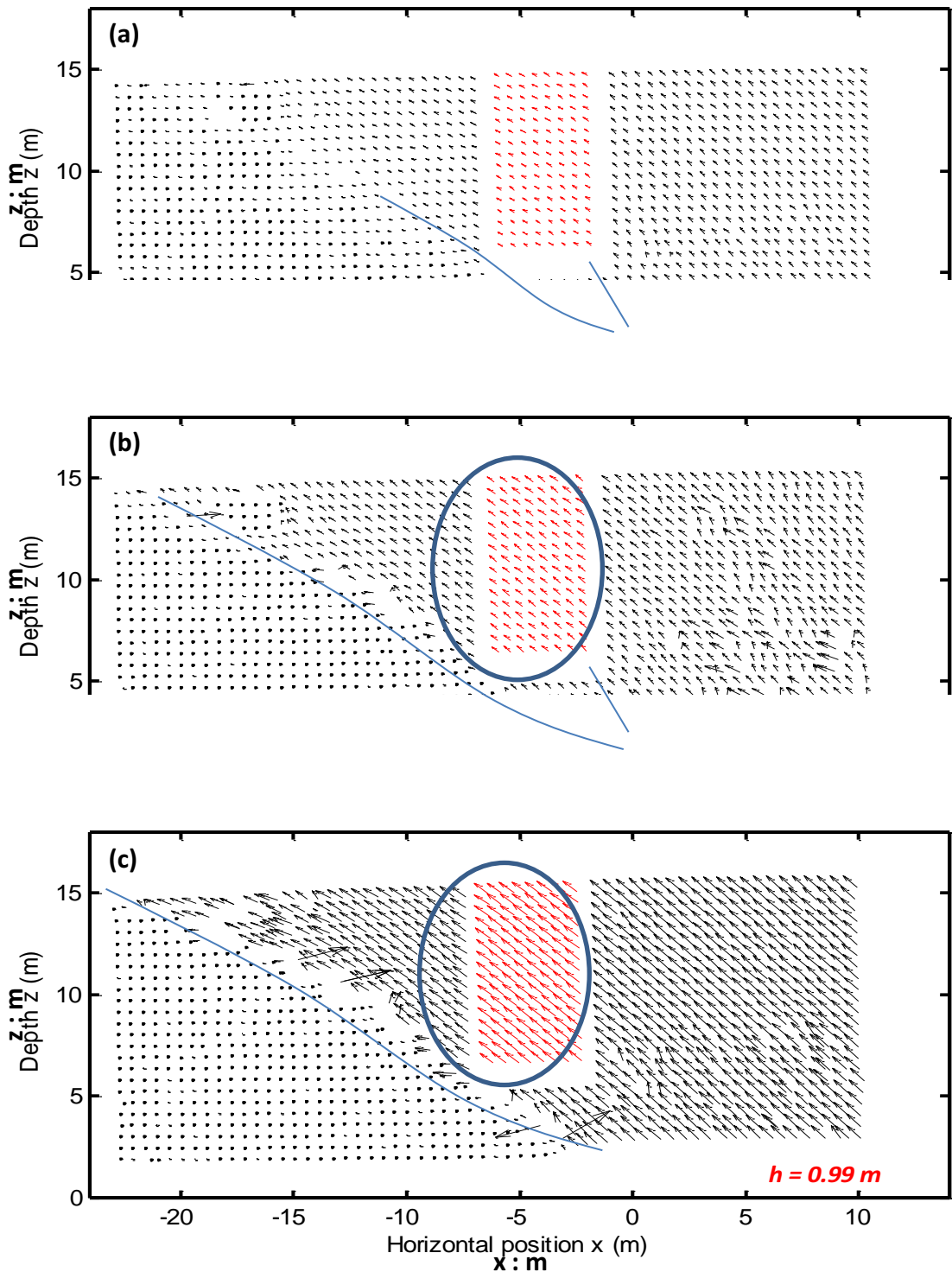


**Figure 6.6. Experiment** -Plot of the incremental displacement of the soil (black vectors) and the caisson (red vectors) in the  $x - z$  plane for different fault through levels, for the reverse fault rupture scenario with the caisson -  $s/B = 0.66$ .

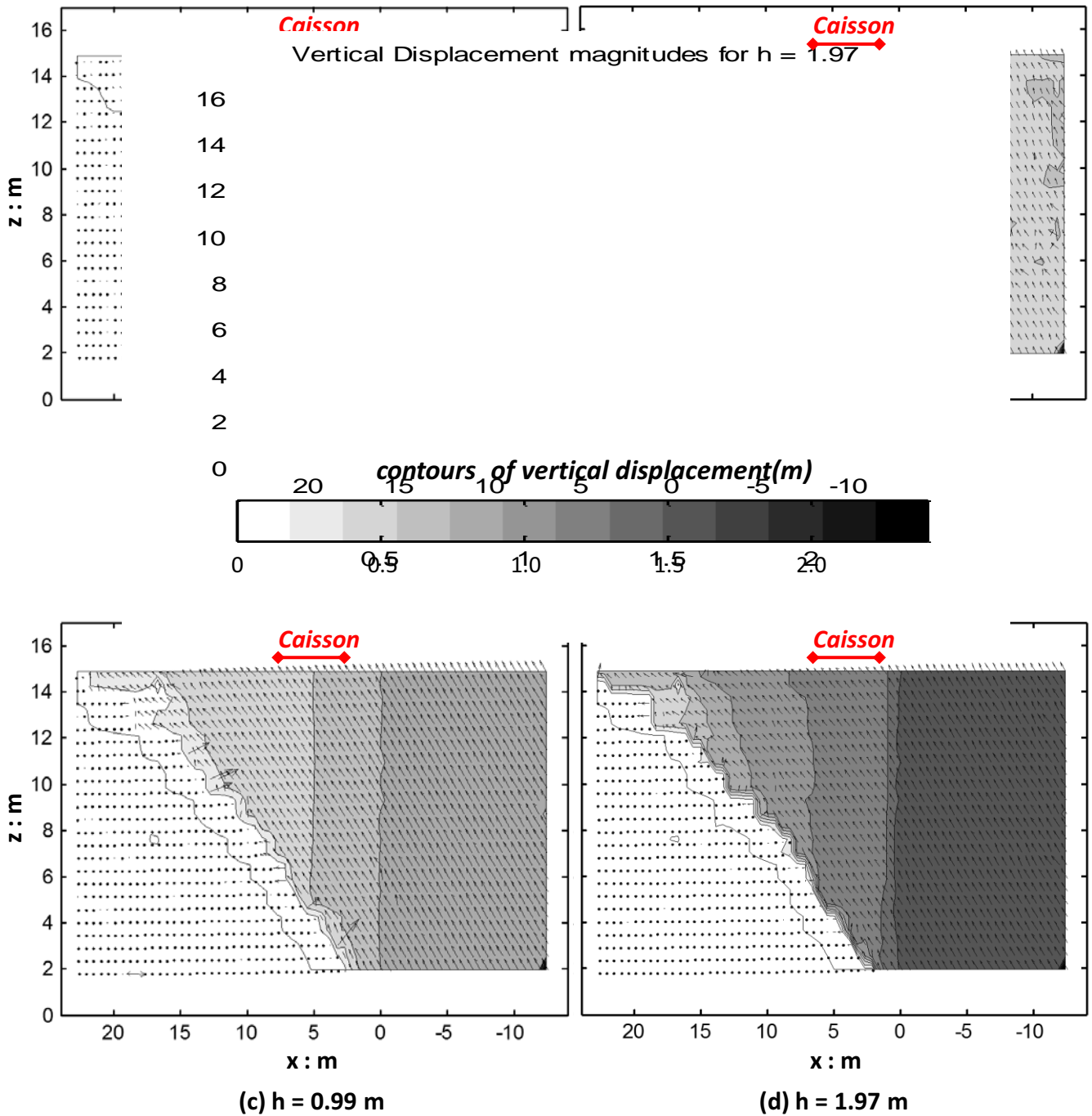


**Figure 6.7. Experiment** - Plot of the incremental displacement of the soil (black vectors) and the caisson (red vectors) in the  $x - z$  plane for different fault through levels, for the reverse fault rupture scenario with the caisson -  $s/B = 0.66$ .

*contours of deformations*

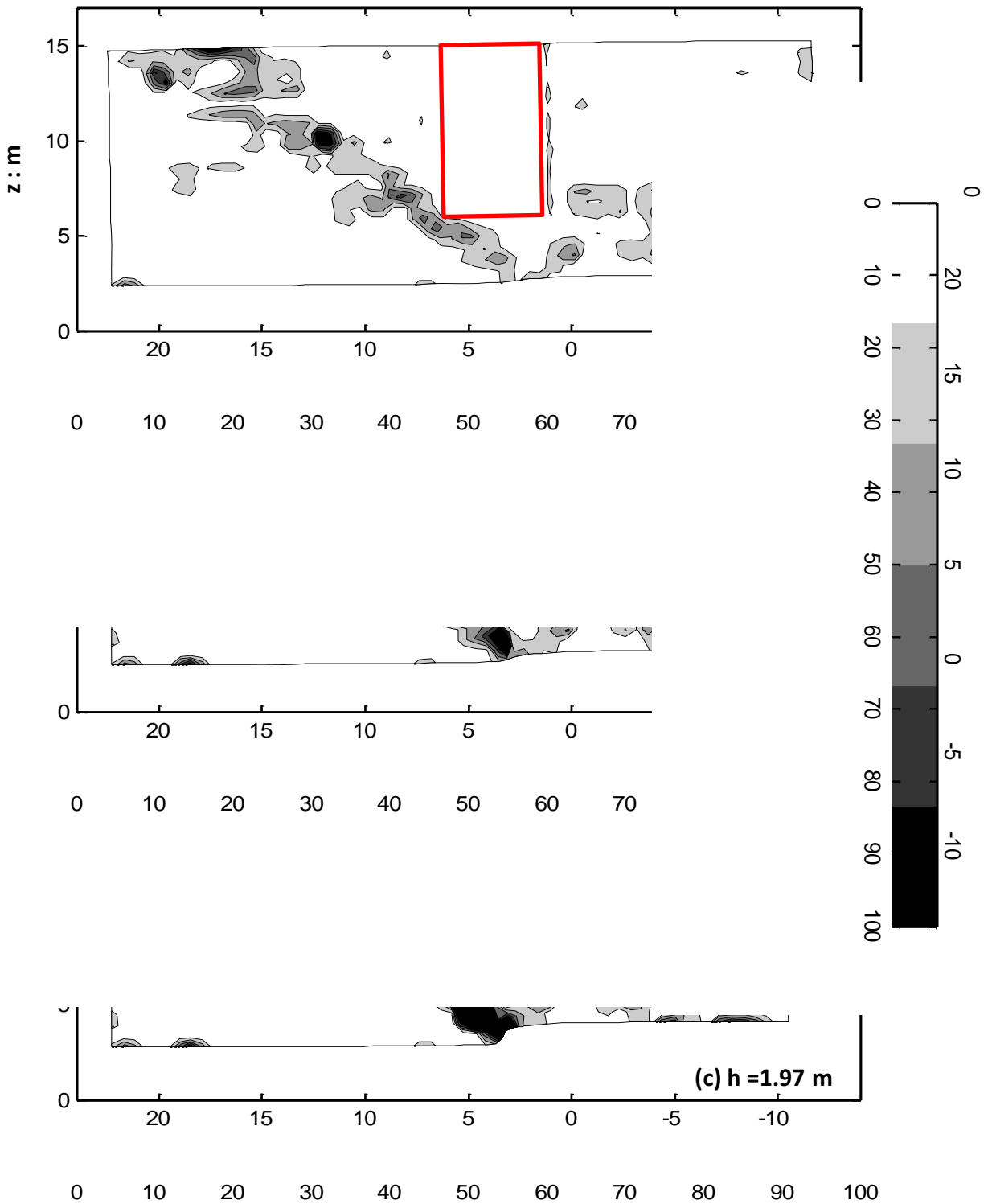


**Figure 6.8. Experiment** - Contours of the deformations in the deformed plane for characteristic values of the fault throw level. Reserve fault rupture scenario with the caisson -  $s/B = 0.66$ .

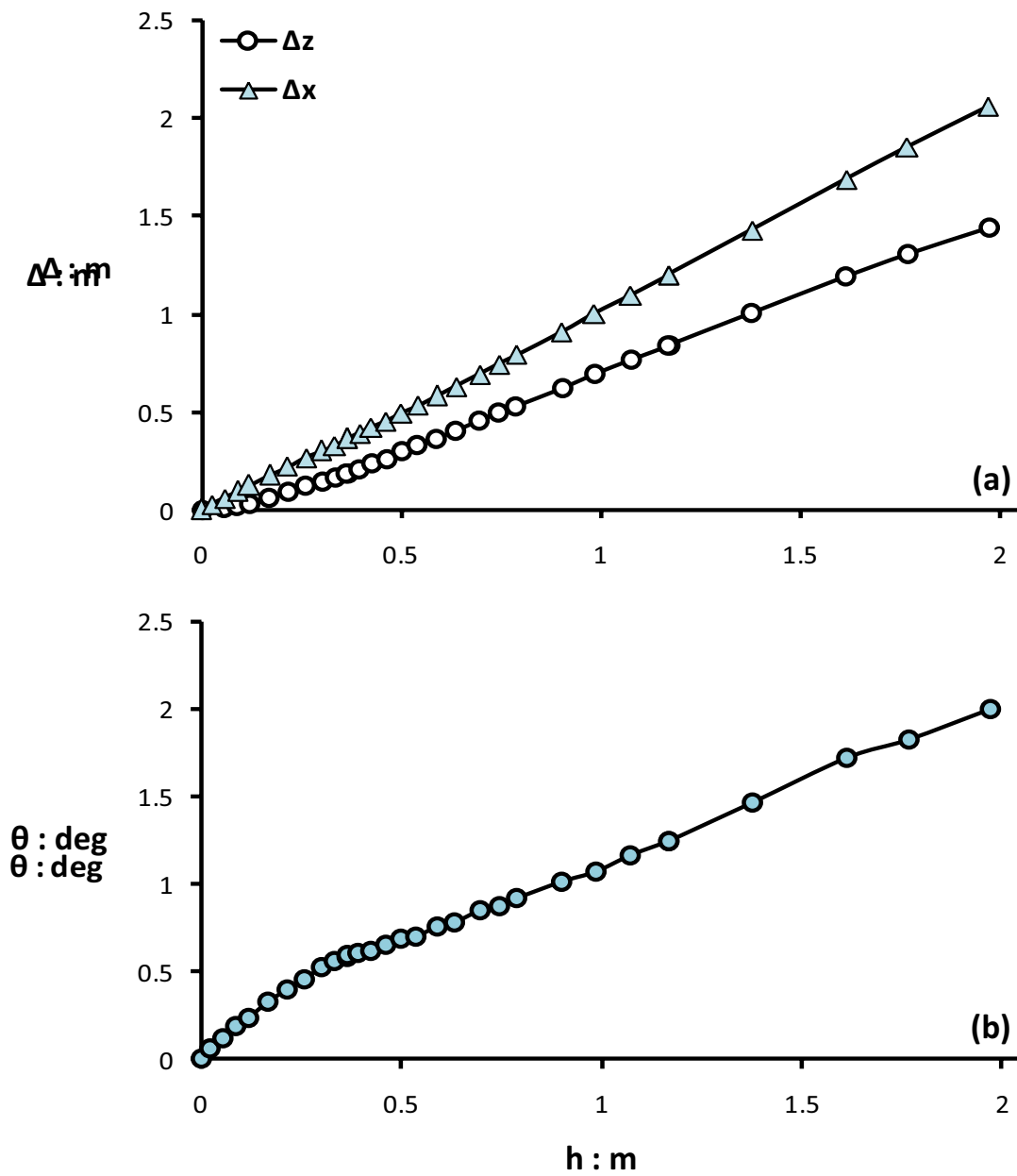


**Figure 6.9. Experiment:** Evolution of (a) the Displacement and (b) the rotation of the caisson with respect to the normal fault rupture displacement,  $h$ . Reverse fault rupture scenario with the caisson -  $s/B = 0.66$ .

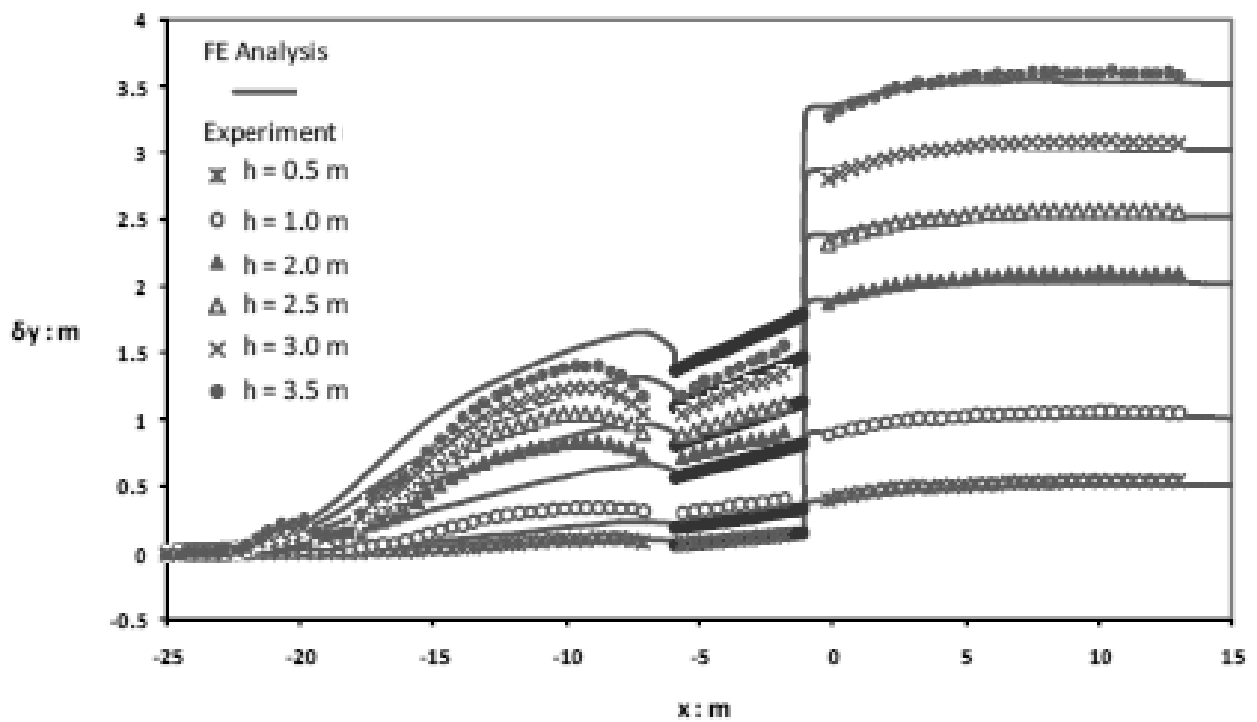


**Figure 6.10.** Comparison between numerical analysis and experimental results referring to the reverse FR propagation in the scenario of  $s/B=0.66$  : vertical displacements of the model surface with respect to the horizontal position for different fault throw values.



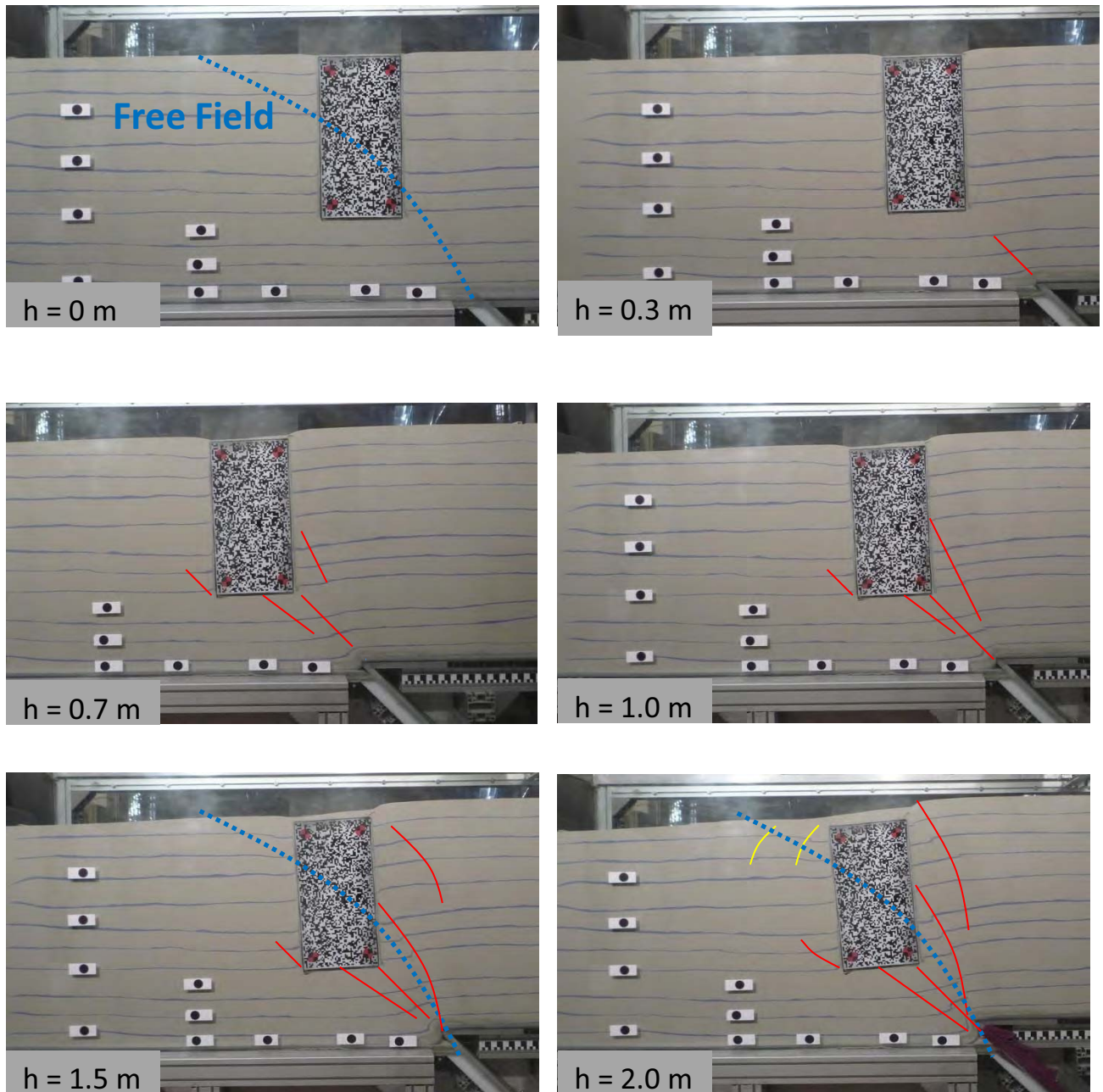


**Figure 6.11a. Experiment** - Snap-shots of soil and caisson deformation at characteristic values of the induced fault rupture displacement  $h$  (prototype scale), for the reverse fault rupture scenario with the caisson -  $s/B = -0.04$ . With red denoted the main fault rupture propagation through the soil and with yellow the secondary and the mechanisms due to the displacement and rotation of the caisson.

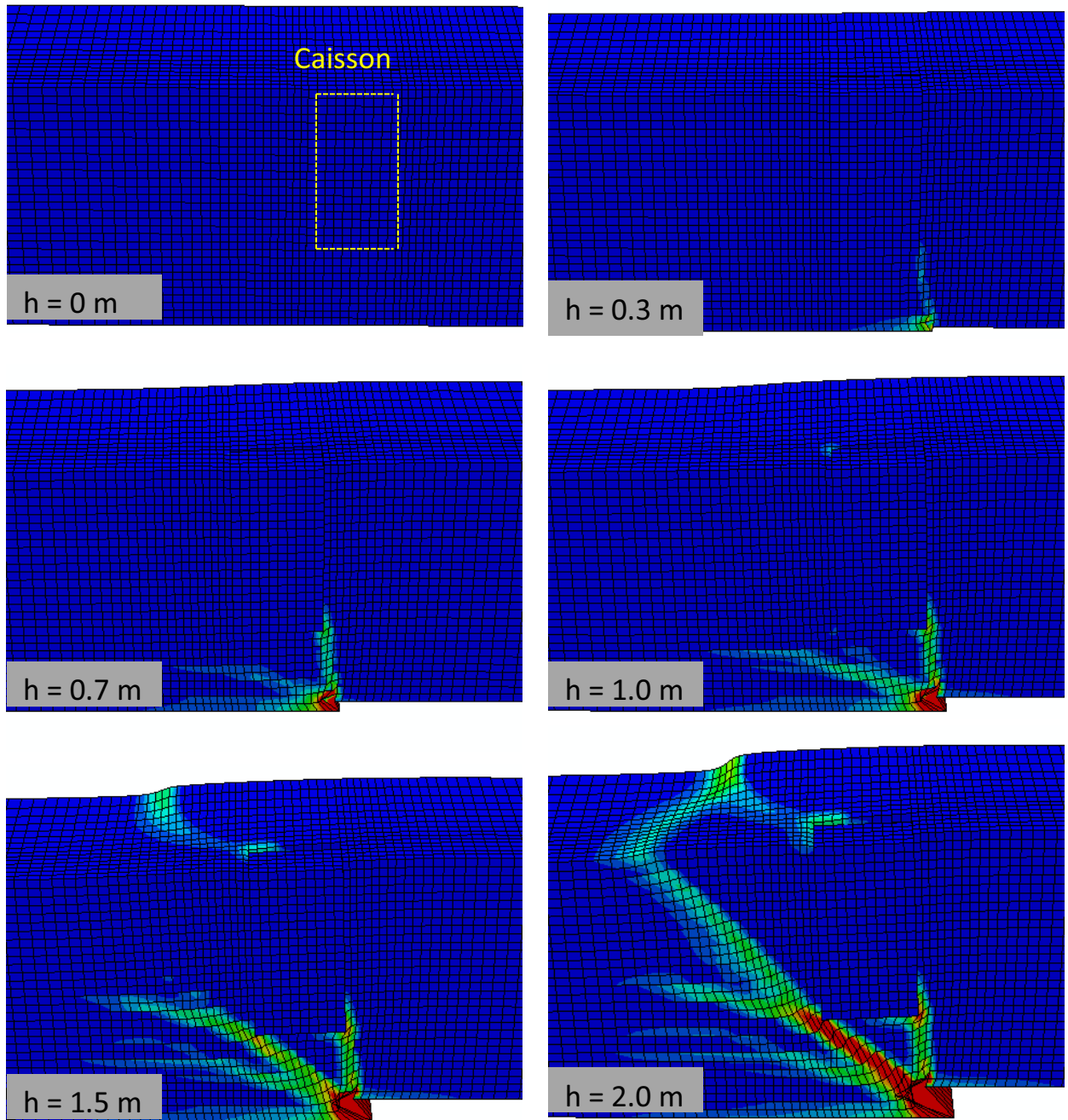


**Figure 6.11b.** Snap-shots of soil and caisson deformation at characteristic values of the induced fault rupture displacement  $h$  (prototype scale), for the reverse fault rupture scenario with the caisson  $-s/B = -0.04$ . The main fault rupture propagation through the soil, the diversion due to the foundation of the fault from the free field propagation path and the secondary ruptures can be visible.

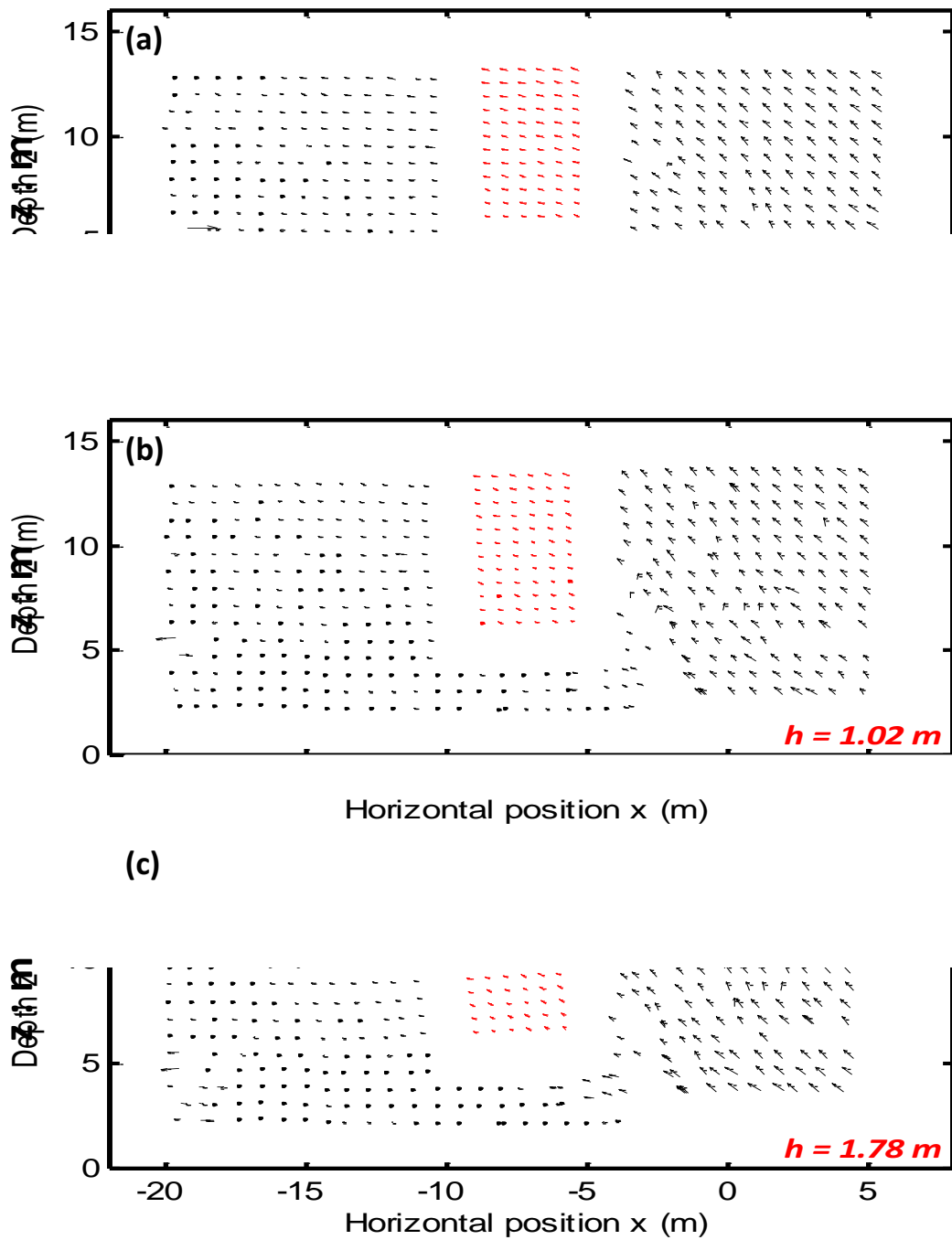


**Figure 6.12. Experiment** - Plot of the incremental displacement of the soil (black vectors) and the caisson (red vectors) in the  $x - z$  plane for different fault through levels, for the reverse fault rupture scenario with the caisson -  $s/B = -0.04$ .

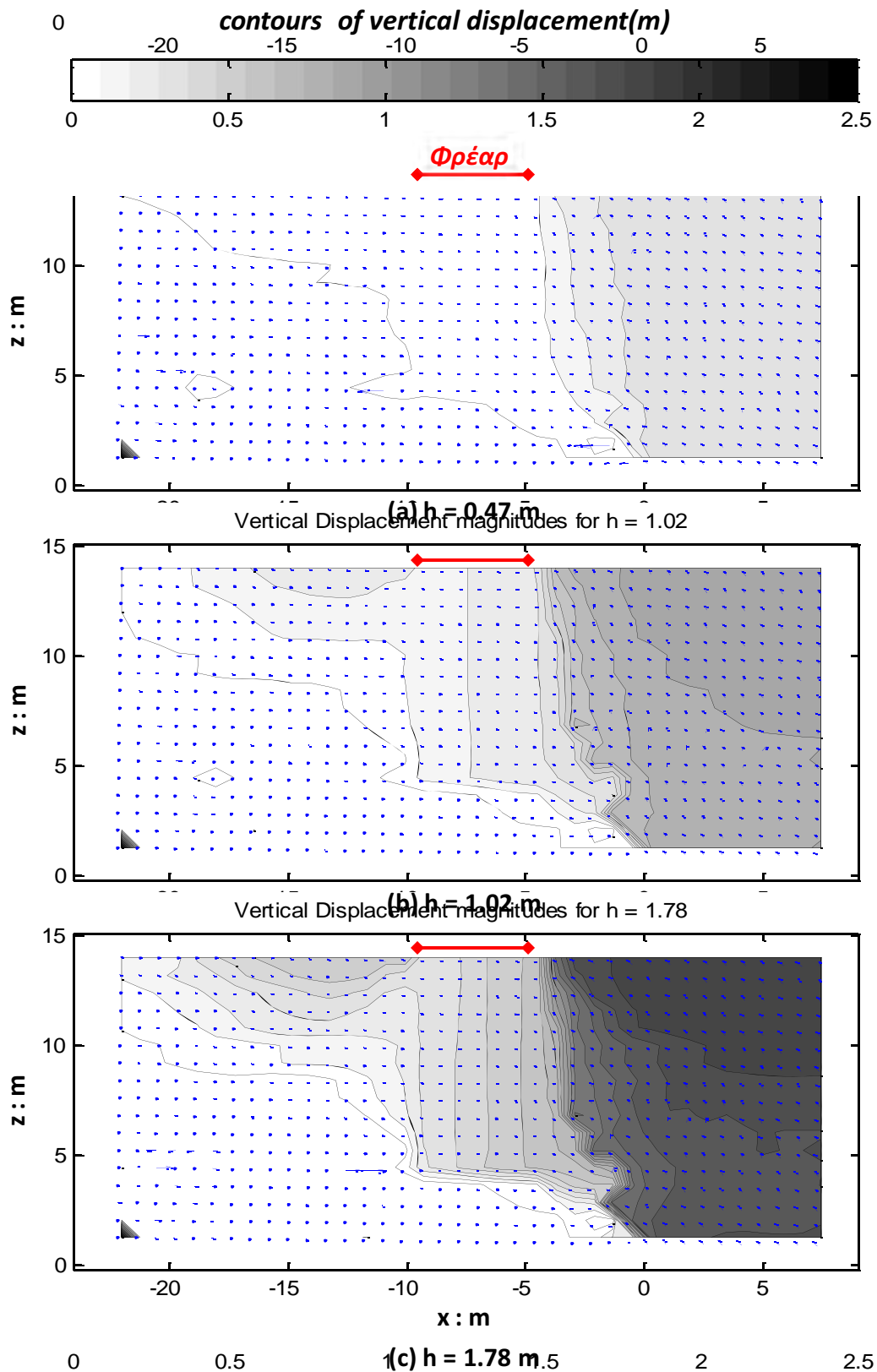


**Figure 6.13. Experiment** - Plot of the incremental displacement of the soil (black vectors) and the caisson (red vectors) in the  $x - z$  plane for different fault through levels, for the reverse fault rupture scenario with the caisson -  $s/B = -0.04$ .

*contours of deformations*

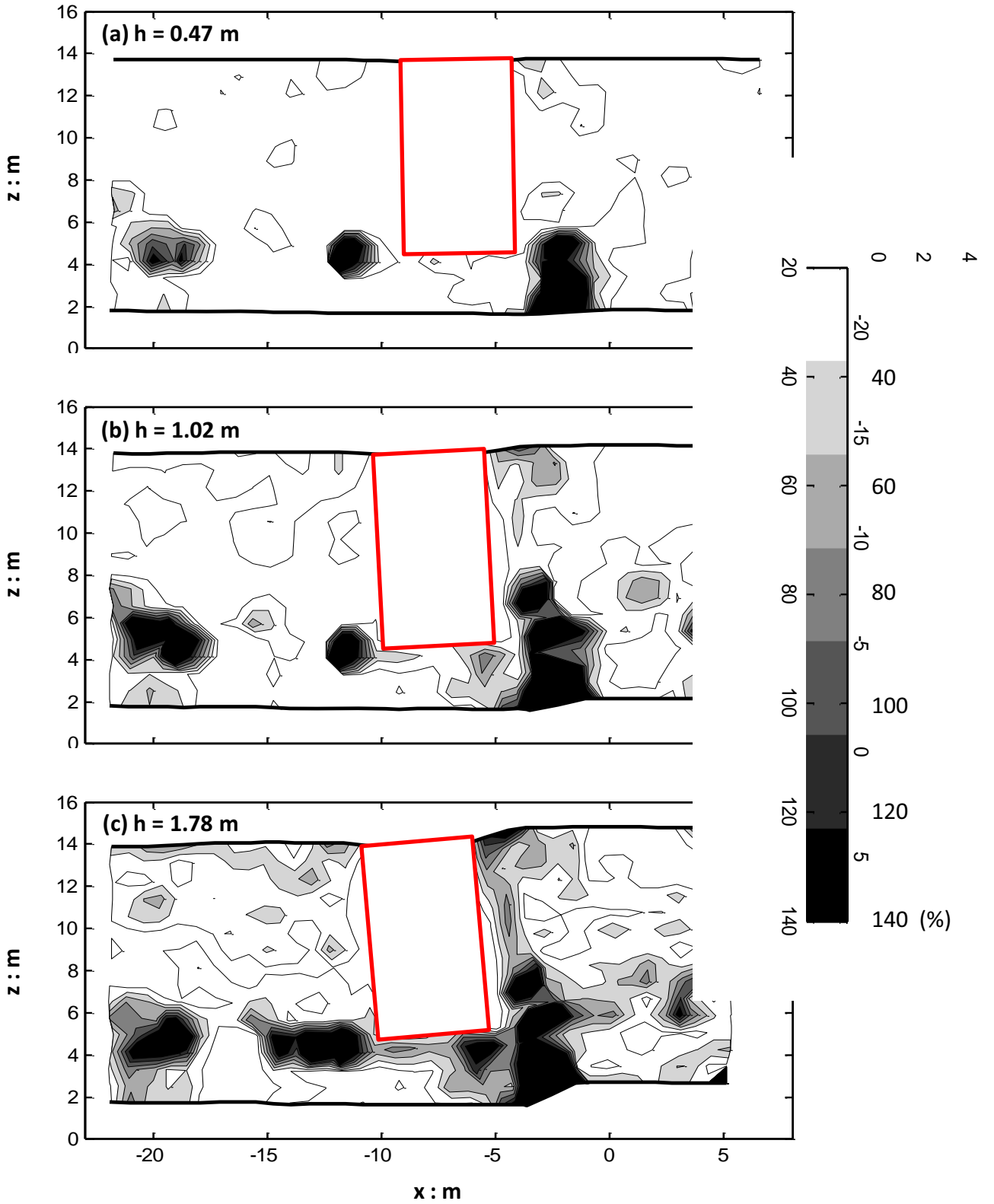


**Figure 6.14. Experiment** - Contours of the deformations in the deformed plane for characteristic values of the fault throw level. Reserve fault rupture scenario with the caisson -  $s/B = -0.04$ .

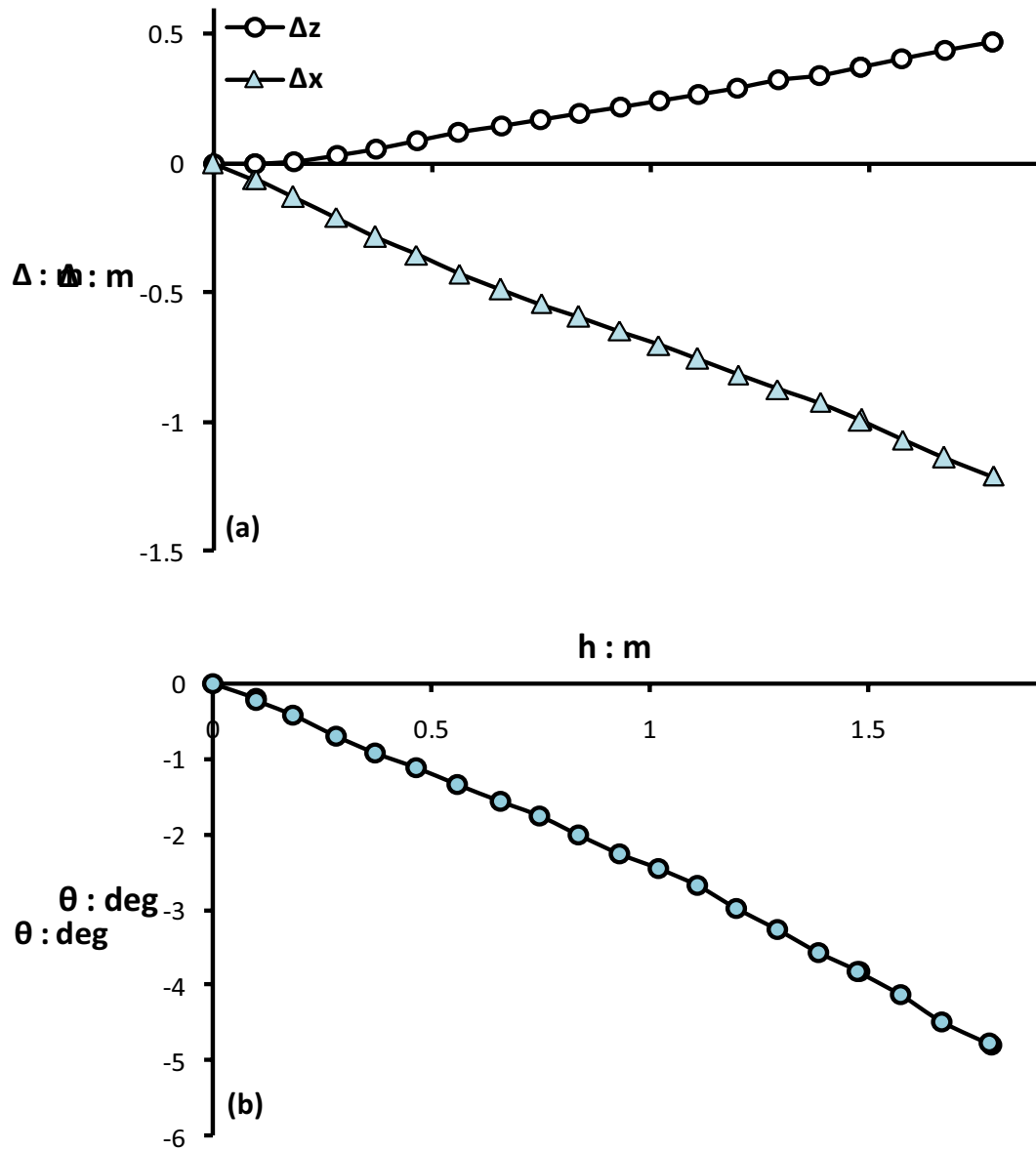


**Figure 6.15. Experiment** - Evolution of (a) the Displacement and (b) the rotation of the caisson with respect to the normal fault rupture displacement,  $h$ . Reverse fault rupture scenario with the caisson -  $s/B = -0.04$ .

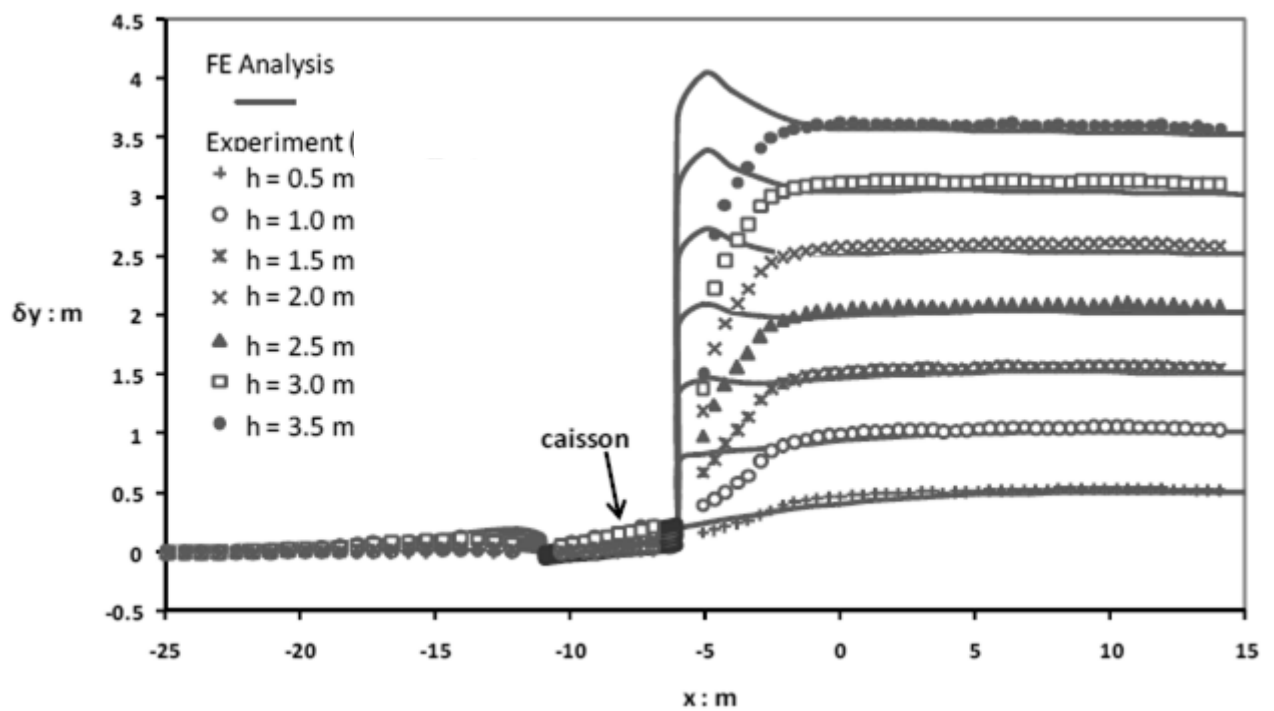


**Figure 6.16.** Comparison between numerical analysis and experimental results referring to the reverse FR propagation in the scenario of  $s/B=-0.04$  : vertical displacements of the model surface with respect to the horizontal position for different fault throw values.

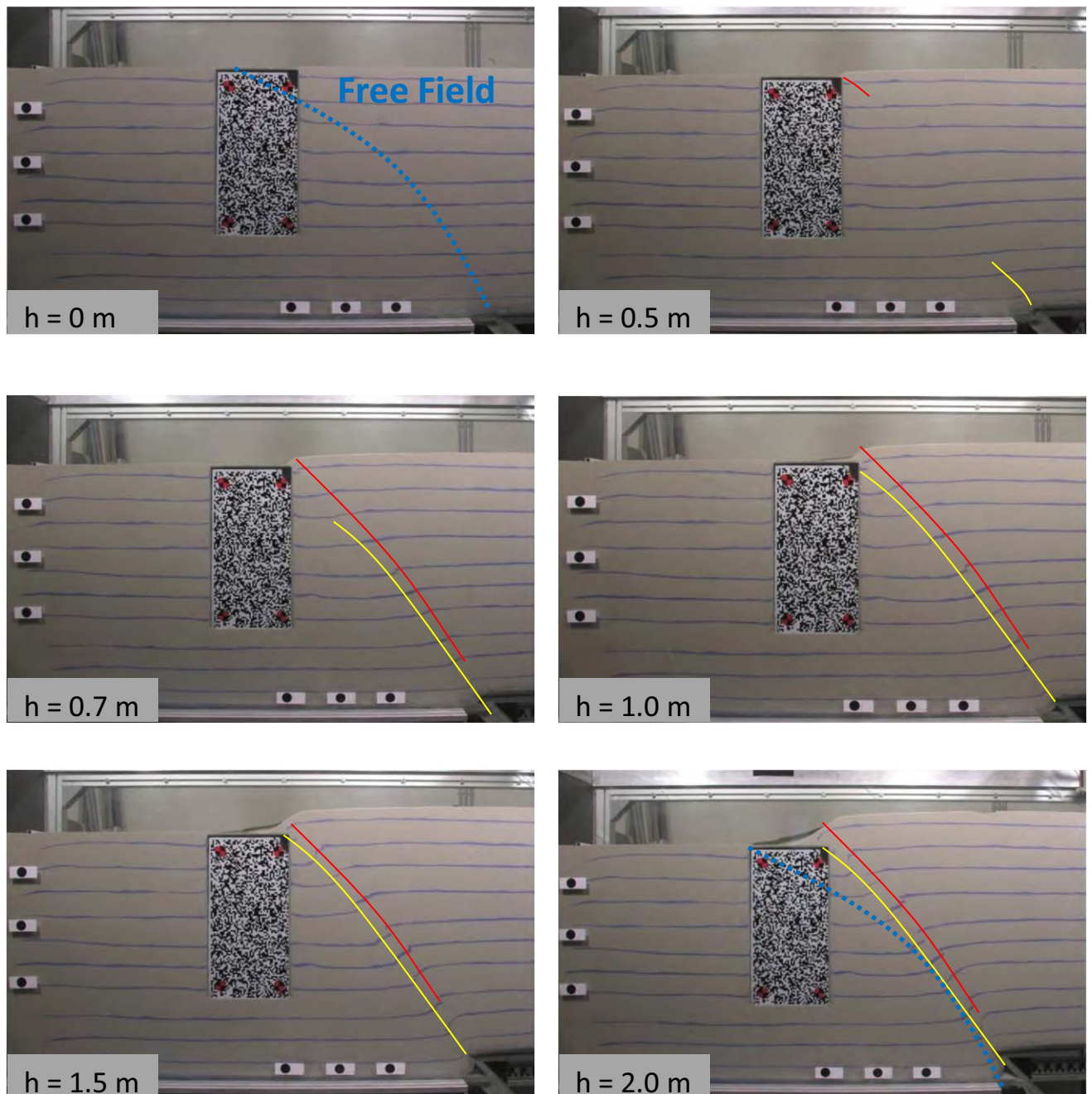


**Figure 6.17a. Experiment** - Snap-shots of soil and caisson deformation at characteristic values of the induced fault rupture displacement  $h$  (prototype scale), for the reverse fault rupture scenario with the caisson -  $s/B = -0.96$ . With red denoted the main fault rupture propagation through the soil and with yellow the secondary.



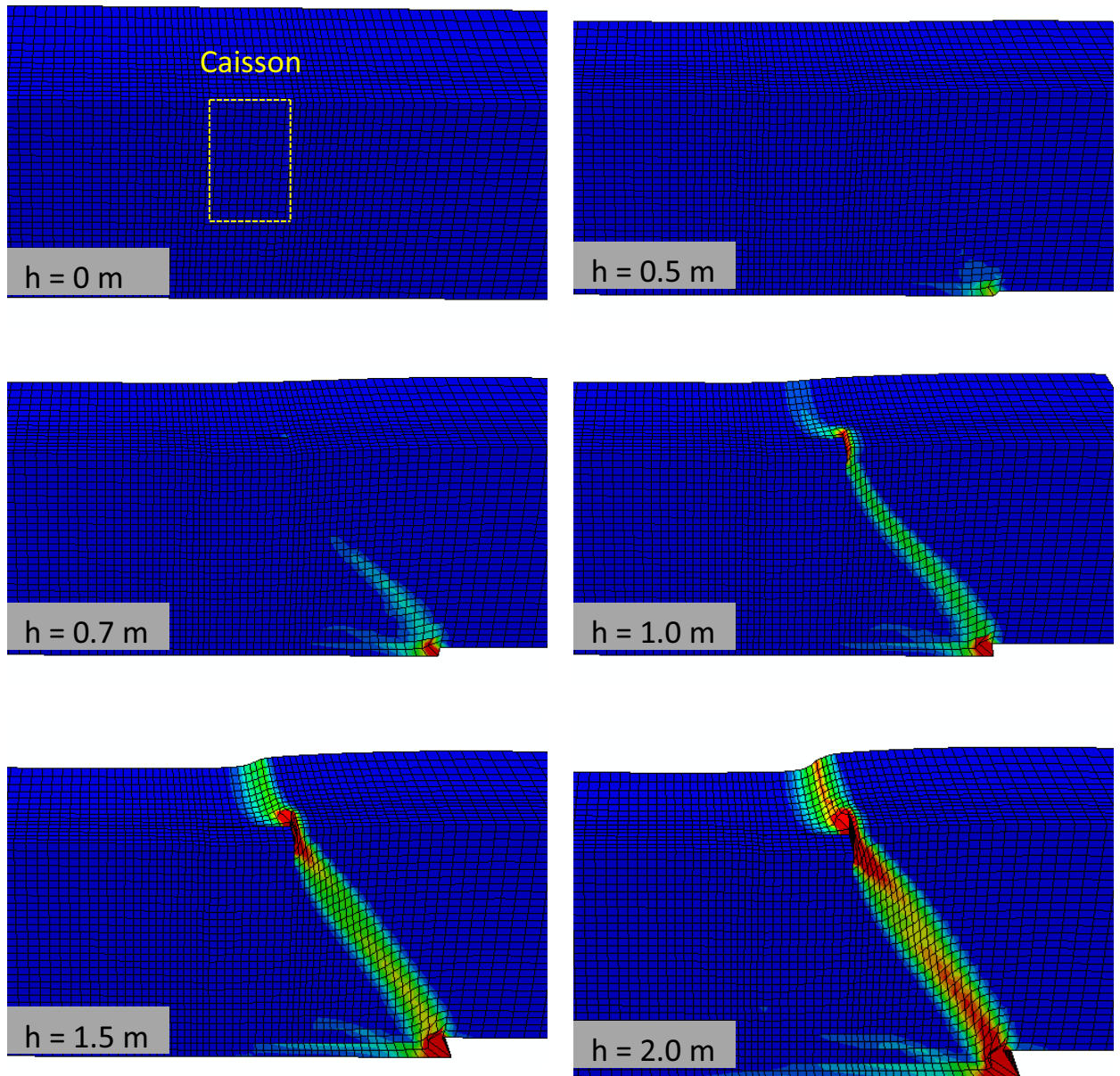


**Figure 6.17b.** Snap-shots of soil and caisson deformation at characteristic values of the induced fault rupture displacement  $h$  (prototype scale), for the reverse fault rupture scenario with the caisson  $-s/B = -0.96$ . The main fault rupture propagation through the soil, the diversion due to the foundation of the fault from the free field propagation path and the secondary ruptures can be visible.

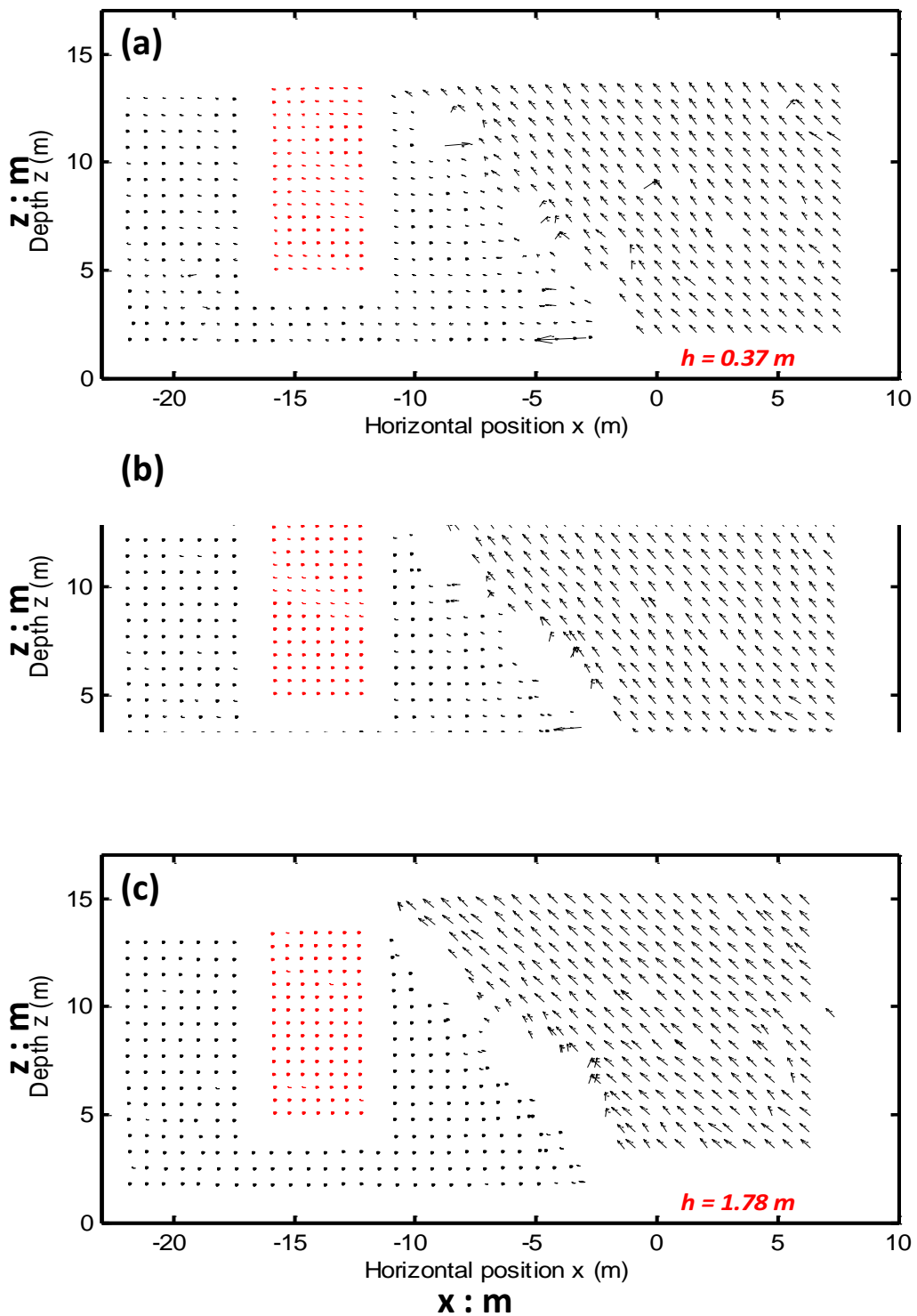


**Figure 6.18. Experiment** - Plot of the incremental displacement of the soil (black vectors) and the caisson (red vectors) in the  $x - z$  plane for different fault through levels, for the reverse fault rupture scenario with the caisson -  $s/B = -0.96$ .

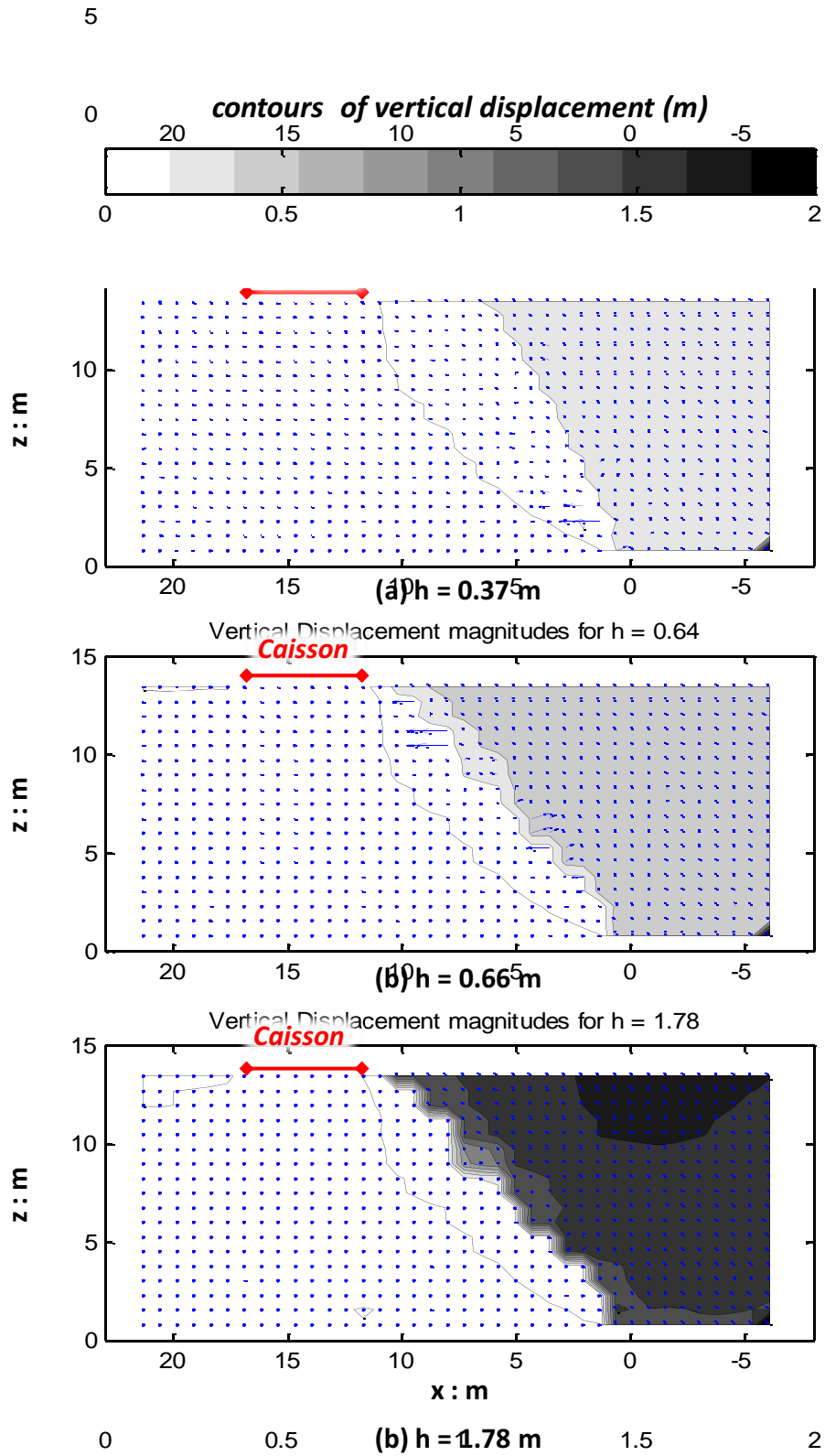


**Figure 6.19. Experiment** - Plot of the incremental displacement of the soil (black vectors) and the caisson (red vectors) in the  $x - z$  plane for different fault through levels, for the reverse fault rupture scenario with the caisson -  $s/B = -0.96$ .

*contours of deformations*

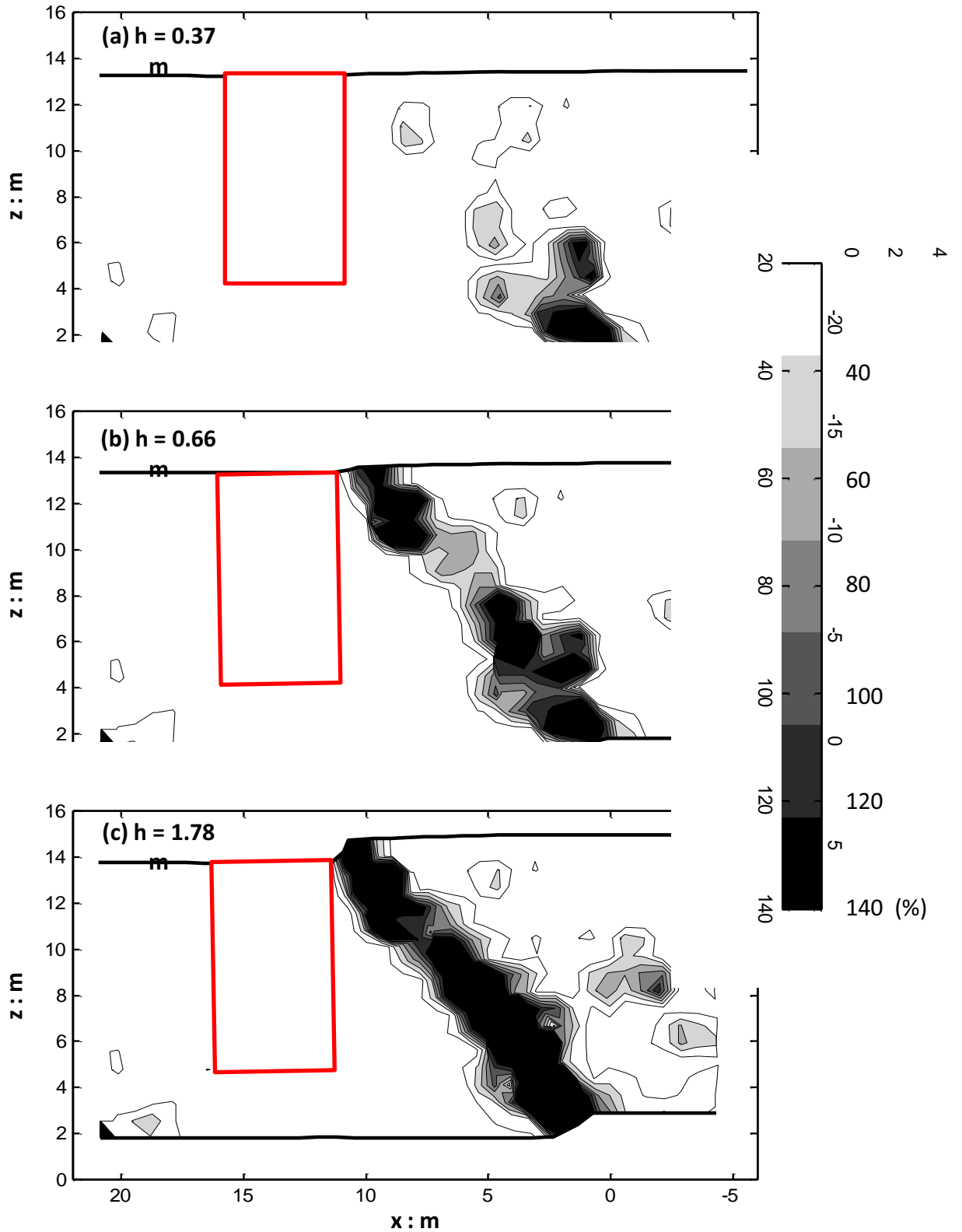


**Figure 6.20. Experiment** Contours of the deformations in the deformed plane for characteristic values of the fault throw level. Reserve fault rupture scenario with the caisson  $-s/B = -0.96$ .

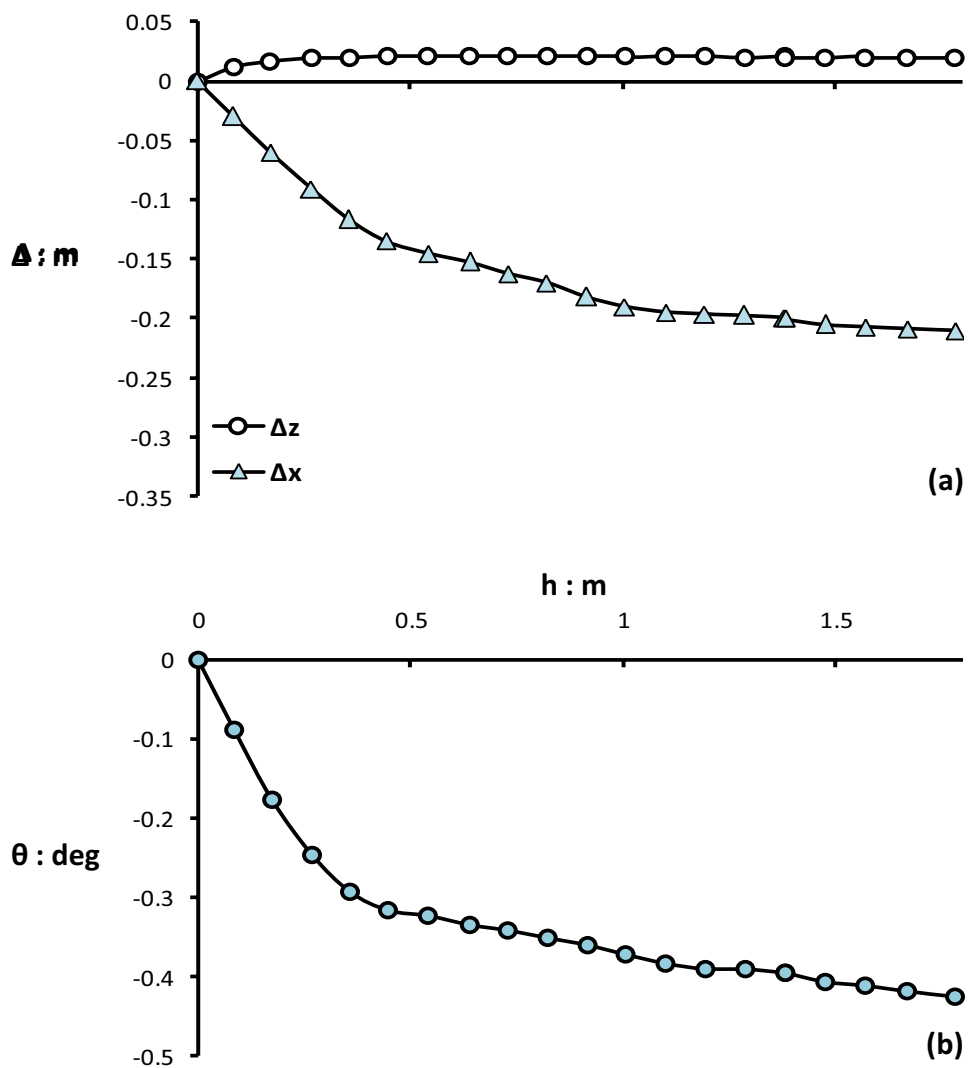


**Figure 6.21. Experiment** - Evolution of (a) the Displacement and (b) the rotation of the caisson with respect to the normal fault rupture displacement,  $h$ . Reverse fault rupture scenario with the caisson -  $s/B = -0.96$ .



# *Chapter 7*

## **CONCLUSIONS**

## 7.1 CONCLUSIONS

The concluding remarks drawn by the present study are that:

- Caisson foundations interact with dip-slip fault rupture (normal and reverse) and change, sometimes dramatically, its free field path. The rigid caisson body acts as a kinematic obstacle, which forces the fault to divert. This is an important difference of caissons compared to other types of foundations (shallow footings or piles), which cause only partial diversion of the fault if at all.

- The foundation position with reference to the free field rupture is proved to be a determinative parameter controlling the response of the system. Different FRSFSI mechanisms were observed for different positions of the caisson relative to the fault and were described previously in extent. The performance of the caisson, due to its interaction with the fault rupture varied from dramatic to minor when the position of the caisson with reference to the fault application point was changed by only 2 m.

- A sophisticated numerical methodology was employed and validated by the comparison between centrifuge experiments and equivalent numerical simulations. Despite the shortcoming of the numerical method to capture the strain localization along the rupture paths, the analysis captured the general pattern of the FRSFSI mechanisms and the consequent displacement performance of the caisson being in satisfactory agreement with the experimental results. Hence, the numerical method can effectively be employed for the study of other similar problems.



- The validation of the numerical method allowed the conduction of a parametric study to further investigate the effect of the foundation position on the system's response. The FRSFSI mechanisms taking place at different positions s/B were identified and the accompanying foundation performance was discussed. Moreover, the position - or the zone of positions - where the fault causes the most detrimental effect was identified for both reverse and normal faults.

- Admittedly, as it has been pointed out by previous studies, it is practically impossible to predict the exact outcrop position even in the case of existing-known faults. However, developed caisson rotation-position curves could be treated as response envelopes and used to estimate the maximum distress that a similar caisson would probably experience for a specific amount of fault throw.

- This can be a first step for the development of design guidelines regarding the response of structures supported on caisson foundations on seismically active areas.

## 8.2 LIMITATIONS

The results and hence the conclusions are subjected to the following limitations:

- The soil in both the experiment and the numerical analysis was considered to be dry – fully saturated sand.

- The nonlinear soil behavior and the scale effects associated with numerical modeling were taken into account only in an approximate-simplified manner.

- The stress conditions during the experimental simulation are not realistically, and can lead to miss-guiding results. Thus, the scaled 1-g modeling, although a very useful tool, it should be used carefully and always bearing in mind its inherent weaknesses, when interpreting the results.

- In case that the foundation–structural system is subjected to fault rupture deformation loading during an earthquake, this is obviously accompanied by dynamic loading. It is believed that the dynamic loading applied at the soil and the structure at the same time with the fault rupture would cause larger displacements of the foundation. However, this effect is ignored in the framework of the present study.

- In both numerical and experimental analysis the single caisson foundation, that could be that of a bridge pier, is modeled as a single degree of freedom pier. This is certainly a simplification of reality, especially since in most real cases the bridge failures under fault loading have been attributed to deck collapses due to relative displacements between consecutive piers.

### **8.3 FUTURE WORK**

Future research studies on the interaction of bridges–caissons with fault rupture could pursue the following objectives:

- Investigating the effect of other controlling parameters such as the soil depth, the foundation geometry and the fault dip angle.
- Investigating the response of a bridge in the longitudinal direction (i.e. the effect of relative displacements between consecutive piers).

- Experimental investigation of the response of the other type of deep foundations (i.e. piles).



# ***LIST of REFERENCES***

Ahmed, W., Bransby, M.F., (2009). "The interaction of shallow foundations with reverse faults." *Journal of Geotechnical and Environmental Engineering* 135 (7), 914- 924.

Anastasopoulos, I., Gazetas, G., (2007a). "Foundation-structure systems over a rupturing normal fault: Part I. Observations after the Kocaeli 1999 earthquake." *Bulletin of Earthquake Engineering*, 5 (3), pp. 253-275.

Anastasopoulos, I., Gazetas, G., (2007b). "Foundation-structure systems over a rupturing normal fault: Part II. Analysis of the Kocaeli case histories." *Bulletin of Earthquake Engineering*, 5 (3), pp. 277-301.

Anastasopoulos, I., Gazetas, G., (2007). "Interaction of shallow and deep foundations with a rupturing normal fault" *Proc., 2nd Japan-Greece Workshop on Seismic Design, Observation and Retrofit of Foundations*, Tokyo, pp. 1-26

Anastasopoulos, I., Gazetas, G., Bransby, M.F., Davies, M.C.R., El Nahas, A., (2007c). "Fault rupture propagation through sand: Finite-element analysis and validation through centrifuge experiments".*Journal of Geotechnical and Geoenvironmental Engineering*, 133 (8), pp. 943-958.

Anastasopoulos, I., Gazetas, G., Drosos, V., Georgarakos, P., Kourkoulis, R., (2008d). "Design of bridges against large tectonic deformations." *Earthquake Engineering and Engineering Vibrations*, Vol. 7, No. 4. (1 December 2008), pp. 345-368.

Anastasopoulos, I., Gerolymos, N., Gazetas, G., Bransby, M.F., (2008a). "Simplified approach for design of raft foundations against fault rupture. Part I: Free-field." *Earthquake Engineering and Engineering Vibration*, 7 (2), pp. 147-163.

Anastasopoulos, I., Gerolymos, N., Gazetas, G., Bransby, M.F., (2008b). "Simplified approach for design of raft foundations against fault rupture. Part II: Soil-structure interaction." *Earthquake Engineering and Engineering Vibration*, 7 (2), pp. 165-179.

Bolton, M. D., (1986). "The strength and dilatancy of sands." *Geotechnique* 36(1):65- 78.

Bransby, F., Davies, M.C.R., El Nahas, A., Nagaoka S., (2008). "Centrifuge modelling of normal fault-foundation interaction." *Bulletin of Earthquake Engineering, Special Issue: Integrated approach to fault rupture- and soil-foundation interaction, Vol. 6, no. 4, pp. 607-628.*

Bransby, F., Davies, M.C.R., El Nahas, A., Nagaoka S., (2008). "Centrifuge modelling of reverse fault-foundation interaction." *Bulletin of Earthquake Engineering, Special Issue: Integrated approach to fault rupture- and soil-foundation interaction, Vol. 6, no. 4, pp. 585-605*

Bray, J.D., Seed, R.B., Cluff, L.S., Seed, H.B., (1994a). "Earthquake fault rupture propagation through soil." *Journal of Geotechnical Engineering* 120(3), pp. 543-561.

Bray, J.D., Seed, R.B., Cluff, L.S., Seed, H.B., (1994b). "Analysis of earthquake fault rupture propagation through cohesive soil." *Journal of Geotechnical Engineering* 120(3), pp. 562-580.

Chang K-C., Chang, D-W., Tsai, M-H., Sung, Y-C., (2000). "Seismic performance of highway bridges." *Earthquake Engineering and Engineering Seismology*, 2(1), pp. 55- 77.

Day, R.W. (2002), *Geotechnical earthquake engineering handbook*, McGraw Hill.

EC8 (1994) Eurocode 8-design of structures for earthquake resistance. Part 5: foundations, retaining structures and geotechnical aspects. prEN1998-5, Final draft August 2003. *Comite Europeen de Normalisation, Brussels*

El Nahas, A., Bransby, M.F. and Davies, M.C.R. (2006). "Centrifuge modelling of the interaction between normal fault rupture and rigid, strong raft foundations." *Proc. International Conference on Physical Modelling in Geotechnics, Hong Kong, August 2006.* 337-342.

Faccioli, E., Anastasopoulos, I., Gazetas G., Callerio, A., Paolucci, R., (2008). "Fault rupture-foundation interaction: selected case histories." *Bulletin of Earthquake Engineering, Special Issue: Integrated approach to fault rupture- and soil-foundation interaction, Vol. 6, no. 4, pp. 557-583*

Gaudin, C. (2002). "Experimental and theoretical study of the behavior of supporting walls: Validation of design methods." Ph.D. dissertation, *Laboratoire Central des Ponts et Chaussées, Nantes, France.*



Gazetas G., Pecker, A., Faccioli, E., Paolucci, R., Anastasopoulos, I., (2008). "Preliminary design recommendations for dip-slip fault-foundation interaction." *Bulletin of Earthquake Engineering, Special Issue: Integrated approach to fault rupture- and soil foundation interaction*, Vol. 6, no. 4, pp. 677-687.

Kawashima, K. (2001). "Damage of Bridges Resulting from Fault Rupture in The 1999 Kocaeli and Duzce, Turkey Earthquakes and The 1999 Chi-Chi, Taiwan Earthquake." *Workshop on Seismic Fault-Induced Failures-Possible Remedies for Damage to Urban Facilities*, University of Tokyo Press, pp. 171-190.

Kramer, S. L. (1996) "Geotechnical earthquake engineering," Prentice-Hall, New Jersey.

Lade, P.V., and Cole, D.A., Jr. (1984), "Influence Zones in Alluvium Over Dip-Slip Faults." *Journal of Geotechnical Engineering*, Vol. 110, No. 5, pp. 599-615.

Muir Wood D (2004) *Geotechnical modelling*. Spon Press, London

Pamuk A, Kalkan E, Ling HI (2005). "Structural and geotechnical impacts of surface rupture on highway structures during recent earthquakes in Turkey." *Soil Dyn Earthq Eng* Vol. 25, pp. 581-589.

Ulusay R, Aydan O, Hamada M (2002). "The behaviour of structures built on active fault zones: examples from the recent earthquakes of Turkey." *Struct Eng Earthq Eng ASCE* 19(2):149-167.

White DJ, Take WA, Bolton MD, (2003). "Soil deformation measurement using particle image velocimetry (PIV) and photogrammetry." *Geotechnique* 53(7):619-631

Youd, T. L., Bardet, JP, and Bray, J.D. (2000) "Kocaeli, Turkey, Earthquake of August 17, 1999 Reconnaissance Report." Earthquake Spectra, Suppl. A to Vol. 16, pp. 456

# ***Appendix A***



**GeoPIV:**  
**Particle Image Velocimetry (PIV)**  
**software for use in geotechnical testing**

**White D. J.<sup>1</sup>, & Take W.A.<sup>2</sup>**

**CUED/D-SOILS/TR322**

**(October 2002)**

<sup>1</sup> Research Fellow, St John's College, University of Cambridge

<sup>2</sup> Research Fellow, Churchill College, University of Cambridge

# GeoPIV: Particle Image Velocimetry (PIV) software for use in geotechnical testing

**Cambridge University Engineering Department**  
**Technical Report**  
**CUED/D-SOILS/TR322**

**D.J. White & W.A. Take**

**October 2002**

## **Summary**

GeoPIV is a MatLab module which implements Particle Image Velocimetry (PIV) in a manner suited to geotechnical testing. This brief guide describes the practical details of using GeoPIV to measure displacement fields from digital images. In addition, some common pitfalls are described. The performance of the GeoPIV software is summarised, and the references from which further information can be found are listed. The software was written by the Authors during their PhD research.

## **1 Introduction**

The GeoPIV software implements the principles of Particle Image Velocimetry (PIV) in a style suited to the analysis of geotechnical tests. This technical report explains how to use the software and summarises the validation procedures undertaken during the development of the software.

PIV is a velocity-measuring procedure originally developed in the field of experimental fluid mechanics, and is reviewed by Adrian (1991). GeoPIV uses the

principles of PIV to gather displacement data from sequences of digital images captured during geotechnical model and element tests. GeoPIV is a MatLab module, which runs at the MatLab command line. The development and performance of the software are described in detail by White (2002) and Take (2002). Concise details are presented in White *et al.* (2001a, 2001b).

The principles of PIV analysis are summarised in Figure 1. The analysis process used in GeoPIV is indicated by the flowchart shown in Figure 2. PIV operates by tracking the texture (i.e. the spatial variation of brightness) within an image of soil through a series of images. The initial image is divided up into a mesh of PIV test patches. Consider a single of these test patches, located at coordinates  $(u_1, v_1)$  in image 1 (Figure 1). To find the displaced location of this patch in a subsequent image, the following operation is carried out. The correlation between the patch extracted from image 1 (time =  $t_1$ ) and a larger patch from the same part of image 2 (time =  $t_2$ ) is evaluated. The location at which the highest correlation is found indicates the displaced position of the patch  $(u_2, v_2)$ . The location of the correlation peak is established to sub-pixel precision by fitting a bicubic interpolation around the highest integer peak.

This operation is repeated for the entire mesh of patches within the image, then repeated for each image within the series, to produce complete trajectories of each test patch.

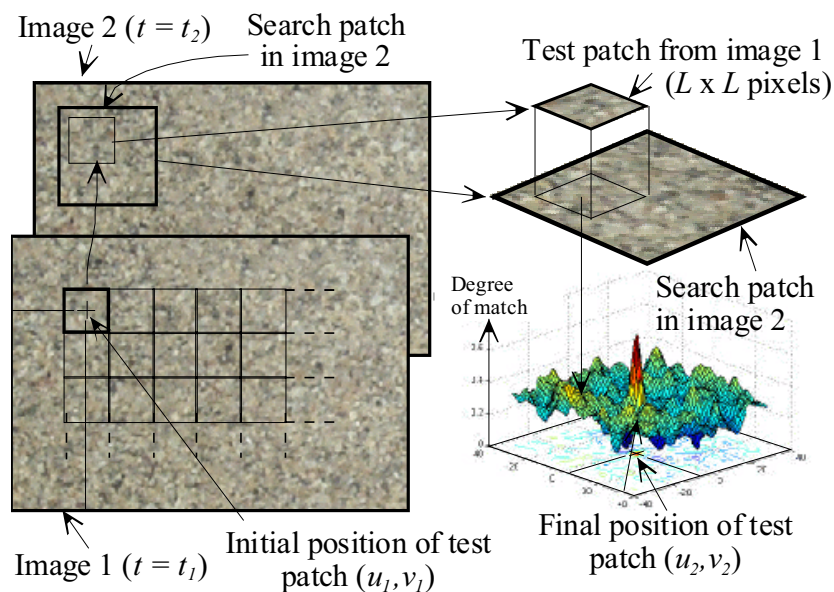


Figure 1. Principles of PIV analysis

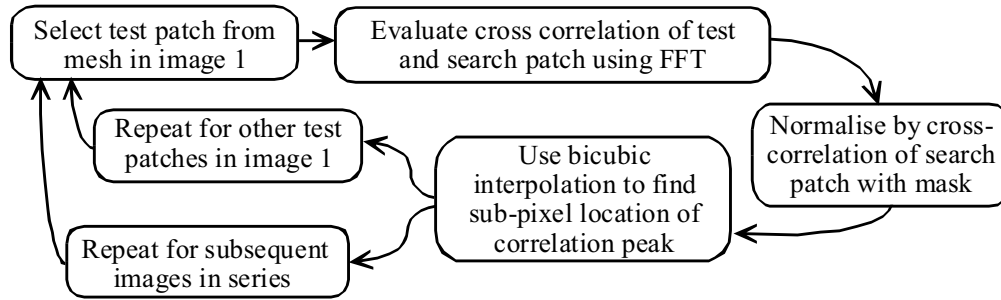


Figure 2. Flowchart of the GeoPIV analysis procedure

The MatLab module requires two input files (a launcher and an initial mesh file) which are prepared in ASCII format by the user. Simple MatLab scripts can be used to assist the preparation of these input files. The output files are in ASCII format, and can be manipulated by the user in MatLab or a spreadsheet to produce displacement and strain data.

## 2 Software validation

The performance of a measurement system can be assessed by considering the errors associated with accuracy and precision. Accuracy is defined as the systematic difference between a measured quantity and the true value. Precision is defined as the random difference between multiple measurements of the same quantity.

Any deformation measurement system based on image analysis consists of two stages. Firstly, the displacement field between two images is constructed. Secondly, this displacement field is converted from image-space (i.e. coordinates in terms of pixels in the image, or mm on the photograph) to object-space (i.e. coordinates in the observed soil).

The precision of a system depends on the method used to construct the displacement field. Random errors associated with the precision of image-based displacement measurement systems include human error in film measurement, and random errors induced by changes in lighting in centroiding (or ‘spot-chasing’) techniques.

The accuracy of a system depends on the process used to convert from image-space to object-space coordinates. Systematic errors associated with the accuracy of image-



based displacement measurement systems arise if the spatial variation in image-scale (i.e. the ratio between lengths in object- and image-space) is ignored.

The GeoPIV software is used to construct the displacement field in image-space coordinates. The conversion from image-space to object-space is separate process, and must be carried out subsequent to the PIV analysis. Validation of the GeoPIV software requires the precision of the technique to be established. The accuracy of any resulting measurements depends on the user's technique of converting from image-space to object-space coordinates.

The image-space to object-space conversion process can be carried out by assuming a constant image scale, or by using photogrammetry to establish the image- to object-space transformation more accurately. Taylor *et al.* (1998) and White *et al.* (2001b) present systems based on the principles of close range photogrammetry. White (2002) describes the photogrammetric reconstruction procedure used in the latter system. Take (2002) describes the target location technique used to perform accurate photogrammetric reconstruction, and assesses the accuracy of this system.

The precision of GeoPIV over small displacement increments was initially evaluated by White *et al.* (2001a), and was considered in greater detail by White (2002) and Take (2002). An experimental apparatus consisting of a translating brass container allowed a non-deforming plane of soil to be translated horizontally beneath a rigidly fixed camera. Small known increments of movement were applied to the soil container via a micrometer and the resulting sequence of images was analysed using GeoPIV. The precision of GeoPIV was evaluated by comparing the displacement vectors deduced from a grid of PIV patches overlying the soil. Since the soil translates as a rigid body, the displacement vectors should be identical; the random variation within the measured vectors indicates the system precision. In addition, artificial images were created and tested in a similar manner.

The precision was found to be a strong function of patch size,  $L$ , and a weak function of image content. An empirical upper bound on the RMS error,  $\rho_{pixel}$ , is given by Equation 1. Although a larger patch size leads to improved precision, the number of

measurement points that can be contained within a single image is reduced. Larger patches ‘smear’ the displacement field in area of high strain gradient. A compromise is necessary. The number of measurement points,  $n_{points}$ , that can be fitted in an image depends on  $L$  and the number of pixels within the image. Equation 2 indicates the number of measurements that can be obtained as a function of image width,  $W$ , and height,  $H$ , in pixels. Equations 1 and 2 are combined in Figure 3 to show the potential precision and measurement array sizes that can be achieved for various sizes of camera CCD.

The performance of GeoPIV compares favourably with the precision of commercial PIV software used in experimental fluid mechanics, although the processing speed is significantly slower. Christensen *et al.* (2000) report an RMS error of 0.0537 pixels for  $L = 64$ , when using orthogonal one-dimensional curve fits through the highest integer pixel correlation peak to establish the sub-pixel displacement increment. GeoPIV uses a slower sub-pixel estimator, in which a bicubic interpolation is fitted to the correlation peak. This sub-pixel estimator is considered responsible for the improved precision, but adds a significant computational burden.

$$\rho_{pixel} = \frac{0.6}{L} + \frac{150000}{L^8} \quad \text{(Equation 1)} \quad n_{points} = \frac{WH}{L^2} \quad \text{(Equation 2)}$$

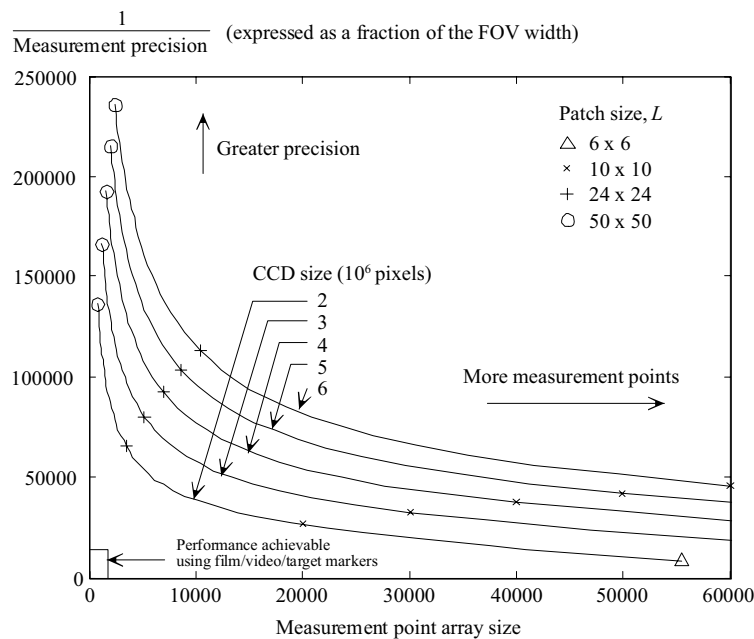


Figure 3. GeoPIV precision and measurement array size vs. camera CCD resolution

### 3 Software usage

Figure 4 shows schematically the steps required to conduct PIV analysis on a series of digital images using the GeoPIV software. The user is required to prepare two ASCII input files.

GeoPIV7\_launcher.txt (at the time of writing the latest development of GeoPIV is version 7) lists the images to be analysed and the display parameters to be used during the run. GeoPIV7\_mesh.txt contains the coordinates and sizes of the initial grid of PIV patches. This grid of patches is established in the first image of the series and each patch is tracked through the subsequent images. The two input files are formatted as follows.

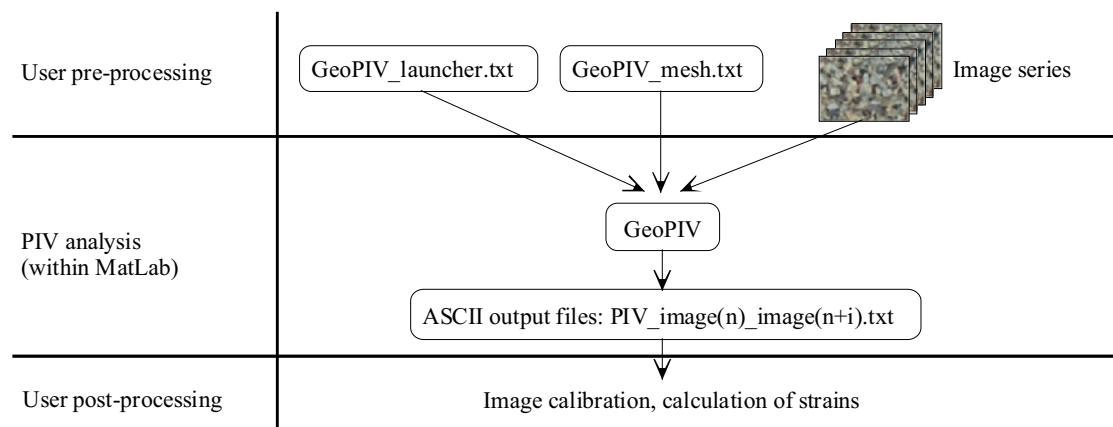


Figure 4. GeoPIV software usage

#### 3.1 Input file #1: *GeoPIV7\_launcher.txt*

The file `GeoPIV7_launcher.txt` is shown in Figure 5. This template contains the input variables for each PIV analysis. It is recommended that the name of this file be changed to identify each PIV run.

All lines preceded by the ‘%’ symbol are ignored by GeoPIV, and can be used to store comments. The input variables are as follows:

`GeoPIV7_mesh.txt` The ASCII input file containing the initial patch locations.

`searchzonepixels` The value following this string is the largest displacement vector which GeoPIV will search for. This value is equal to half

the difference in size of the PIV patch and the search patch shown in Figure 1.

`show_?` By switching the Boolean operator after these variables between 1 (on) and 0 (off), the display options during the PIV run can be changed. Figure 6. shows the displays activated by each variable. These displays allow the progress of the PIV run to be monitored, but add considerably to the calculation time.

`spare_?` Spare. For future use.

`C:\users\` This string indicates the location of the image files. By referring to a remote directory, a single set of image files can be stored at one location, and multiple PIV runs, all stored in different directories, can be conducted without having to make multiple copies of the images.

`leapfrog` The integer following this string indicates how often image 1 is updated. If `leapfrog = 1`, GeoPIV compares images 1 and 2, then 2 and 3, then 3 and 4, etc... This leads to a low measurement precision over a long series of images (since the measurement errors are summed as a random walk), but reduces the chance of wild vectors since patches are easily identifiable after only one displacement step. If `leapfrog` is set higher, for example 3, GeoPIV compares images 1 and 2, 1 and 3, and 1 and 4. At this point the initial image is updated, before comparing images 4 and 5, 4 and 6 etc... To improve precision, the `leapfrog` flag should be set as high as possible, without creating an unacceptably high number of wild vectors.

`subpixelmeth` This flag is superseded, and should be set to one.

`%[Images]` The images to be analysed should be listed below this heading. Most image formats are accepted, including .jpg, .gif, and .tif.

```

GeoPIV7_launcher.txt - Notepad
File Edit Format View Help
%GeoPIV7 LAUNCHFILE, April 2002, Dave White & Andy Take
%project:
%task:

%[MESH TO LOAD]
GeoPIV_mesh.txt 0           %filename of initial mesh

%[PIV ANALYSIS]
searchzonepixels 10        %PIV search zone, smax. (<max disp).

show_mesh 1                %Show PIV mesh during analysis.
show_patch 1               %Show each PIV patch during analysis.
show_quiver 1              %Show quiver plot during analysis.
show_vector 0              %Print vector magnitude during analysis.

spare_A 0                  %Spare. For future use.
spare_B 0                  %Spare. For future use.
spare_C 0                  %Spare. For future use.
spare_D 0                  %Spare. For future use.
spare_E 0                  %Spare. For future use.

C:\users\ 0                %Location of image files

leapfrog 1                 %Leapfrog flag

subpixelmeth 1             %FFT on/off boolean

%[IMAGES]
DCP_0001.jpg
DCP_0002.jpg
DCP_0003.jpg
    
```

Figure 5. GeoPIV7\_launcher.txt

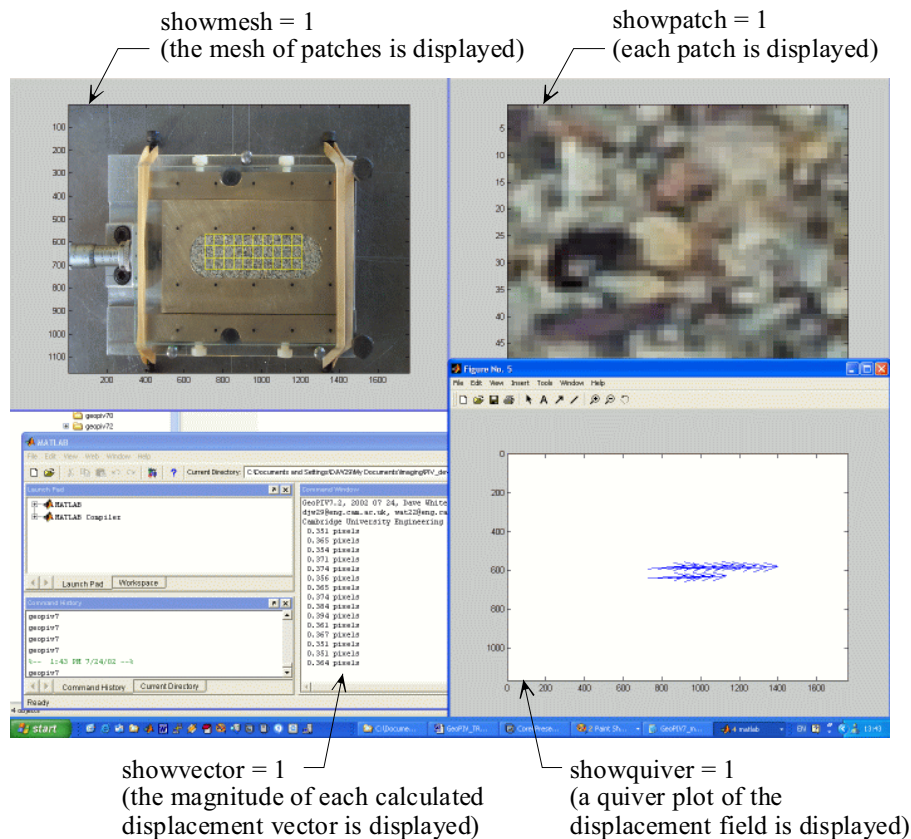


Figure 6. Display options during GeoPIV analysis

### 3.2 Input file #2: *GeoPIV7\_mesh.txt*

The *GeoPIV7\_mesh.txt* input file contains the locations of the initial mesh of PIV patches. This file is in ASCII format, but can be generated from a spreadsheet or using MatLab. The name of *GeoPIV7\_mesh.txt* can be changed to allow easy identification of a particular mesh, with the change being passed through to the fifth line of *GeoPIV7\_launcher.txt*.

Each row of *GeoPIV7\_mesh.txt* defines a single patch. Each initial patch is identified by an ID number (column 1), the  $(u,v)$  coordinates of its centre (columns 4 and 5), and its width,  $L$ , (column 8). The  $(u,v)$  image coordinate system has its origin at the top left of the image, with  $u$  increasing from left to right. A simple mesh file and the resulting grid of patches are shown in Figure 7.

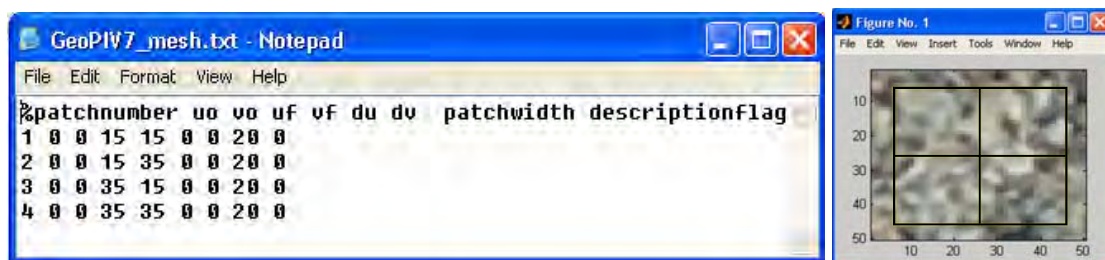


Figure 7. *GeoPIV7\_mesh.txt*

### 3.3 Launching *GeoPIV*

After preparing the two ASCII input files, the user launches *GeoPIV* from the MatLab command line, by typing *GeoPIV7* (at the time of writing the latest release of *GeoPIV* is version 7). The following files must be on the MatLab path:

*GeoPIV7.dll*

*load7.m*

A pop-up box prompts the user to select the appropriate *GeoPIV\_launcher.txt* file. All output files are created within the same directory as the selected launcher file.

After the launcher file is selected, the analysis begins. Any display options selected in the launcher file appear, and construction of the displacement field between the first

image pair starts. After each image pair has been analysed, an expected completion time is shown in the MatLab command window. Meanwhile, an ASCII output file is created after comparison of each image pair.

### 3.4 Output files: *PIV\_image(n)\_image(n+i).txt*

The ASCII output files have an identical format to the GeoPIV\_mesh.txt files. Therefore, the output file from one PIV run can be used as the initial mesh for a subsequent analysis. Each output file has a filename composed of the two images being compared (Figure 8).

Each row of the output file corresponds to a single PIV patch. The first column indicates the patch ID number. The 2<sup>nd</sup> and 3<sup>rd</sup> columns indicate the coordinates of the patch in the first image. The 4<sup>th</sup> and 5<sup>th</sup> columns indicate the coordinates of the patch in the second image. The 6<sup>th</sup> and 7<sup>th</sup> columns show the corresponding displacement vector. Column 7 contains the patch width,  $L$ , carried over from the mesh file. For post-processing, it is usual to load the series of PIV output files created by a single run into a spreadsheet or MatLab.

%patch	uo	vo	uf	vf	du	dv	size	desc	
1	728.0000	591.0000	728.3500	590.9733	0.3500	-0.0267	50.0000	0.0000	
2	778.0000	591.0000	778.3633	590.9667	0.3633	-0.0333	50.0000	0.0000	

Figure 8. PIV output file

## 4 Troubleshooting

It should be noted that PIV analysis can be conducted badly, creating misleading or incorrect displacement data; the phrase “garbage in, garbage out” can be applied. The following section describes some of the pitfalls which can lead to invalid data. The Authors accept no responsibility for any data created using the GeoPIV software. Users should satisfy themselves that the data they have obtained is reliable.

Furthermore, good PIV analysis represents only one stage in the process of obtaining accurate and precise deformation data from a geotechnical test. As noted earlier, the accuracy of the resulting deformation data depends on the process used to convert image-space (PIV) measurements into object-space values.

#### ***4.1 Search zone set too small: wild vectors.***

The search range over which GeoPIV searches for a displaced patch is set by the ‘searchzonepixels’ flag. This flag should be set higher than the largest expected displacement vector. If not, GeoPIV will not search far enough to locate the larger displacement vectors. Instead, wild vectors will be recorded. This problem can be surmounted by setting ‘searchzonepixels’ to be greater than the image width. In this case, GeoPIV will search the entire image, ensuring that each patch is located (assuming that it remains within the image). However, this approach will lead to an impractically long computation time. Therefore, a compromise is needed. The user should manually examine a typical image pair in order to estimate the displacement of the fastest moving point within the image. The ‘searchzonepixels’ flag should then be set comfortably above this value.

If a measured displacement vector is greater than 90% of the search range, an exclamation mark (!) will appear in the command window. This warns the user that the displacement field contains vectors that are approaching or are greater than the search range. The user may wish to rerun the analysis with a larger value of the ‘searchzonepixels’ flag.

#### ***4.2 Frame rate too low: wild vectors***

If wild vectors continue to appear, even when searchzonepixels is set higher than the maximum expected displacement, the frame rate may be too low. This can result in excessive change in the appearance of each patch over each displacement step. This change in appearance may prevent correct identification of the patch. Correct identification is not possible if the correlation peak created when the initial and displaced patches overlay each other is drowned by the noise of the random correlation peaks created elsewhere on the correlation plane (Figure 1 shows a correlation plane in which the displaced patch position creates a single distinct peak).

This situation can be remedied by increasing the patch size. This reduces the influence of random changes in patch appearance. Alternatively, the experiment can be repeated with a higher frame rate, leading to less change in patch appearance between image pairs.



### ***4.3 Patch size too large: strain field detail lost***

If large patches are used, the displacement field is ‘smeared’ within zones of localised deformation. Smaller patches produce improved spatial resolution of the displacement field. If a zone of localised deformation, for example a slip plane, is known to exist, and small patches cannot be used, it may be appropriate to establish an initial mesh consisting of lines of patches on either side of the localisation.

### ***4.4 Patch size too small: wild vectors, reduced precision***

Smaller patches contain less information and are therefore more sensitive than large patches to changes in appearance due to distortion or unsteady lighting. This can lead to wild vectors. Also, small patches offer a lower measurement precision than large patches (Figure 3). These disadvantages are balanced by the improved spatial resolution of the displacement field.

### ***4.5 Leapfrog flag set too low: reduced precision***

It should be noted that the values of measurement precision shown in Figure 3 are for a single small displacement step. If an series of  $n$  images are analysed, with a leapfrog flag equal to  $f$ , the overall measurement error accumulated in the final image is equal to a random walk of length  $\sqrt{(n-1)}$  divided by  $f$ . Therefore, the leapfrog flag should be set as high as possible, to maximise precision, notwithstanding the comments in Section 4.6.

### ***4.6 Leapfrog set too high: wild vectors***

A high leapfrog flag can lead to wild vectors if a patch has become unrecognisable over the  $f$  image steps between updating of the initial patch (cf. Section 4.2). Also, the cumulative displacement of the patch may exceed the search range (cf. Section 4.1 )

### ***4.7 Scratched viewing window: ‘stuck’ patches***

Small scratches on the viewing window can cause image patches to become ‘stuck’. This occurs if the stationary image content due to the scratch outweighs the moving content created by the soil. Larger patches that reach beyond the scratch may overcome this problem.

#### ***4.8 Insufficient texture: wild vectors***

If the image does not contain sufficient texture, i.e. there is a low spatial variation in brightness, the correlation peak created by the displaced patch may not exceed the random noise on the correlation plane. If the images under analysis contain zones of constant brightness, larger patches may be needed to straddle these zones and create an identifiable correlation peak.

### **5 Conclusions**

GeoPIV is a MatLab module which implements Particle Image Velocimetry (PIV) in a manner suited to geotechnical testing. This report describes the practical details of using GeoPIV to measure displacement fields from digital images. In addition, some common pitfalls are described.

Also, the performance of the GeoPIV software is summarised, and the references from which further information can be found are listed. The software can be made available for research external to CUED; contact the Authors for further information.

### **6 Contact details**

The Authors can be contacted as follows if required:

Dave White

djw29@eng.cam.ac.uk

Dept. of Engineering, Trumpington Street, Cambridge, CB2 1PZ

Andy Take

wat22@eng.cam.ac.uk

Dept. of Engineering, Trumpington Street, Cambridge, CB2 1PZ

Any comments on the performance or usability of this software would be appreciated.

## 7 References

Adrian R.J. 1991. Particle imaging techniques for experimental fluid mechanics. Annual review of fluid mechanics 23:261-304

Christensen K.T., Soloff S.M. & Adrian R.J. 2001. PIV Sleuth: integrated Particle Image Velocimetry (PIV) Interrogation/Validation Software. Technical Report 943, Dept. of Theoretical & Applied Mechanics, Univ. Illinois at Urbana-Champaign.

Take W.A. 2002. The influence seasonal moisture cycles on clay slopes. University of Cambridge PhD Dissertation

Taylor R.N., Grant R.J., Robson S. & Kuwano J. 1998. An image analysis system for determining plane and 3-D displacements in soil models. Proceedings of Centrifuge '98, 73-78 pub. Balkema, Rotterdam.

White D.J., Take W.A, Bolton M.D. (2001a) Measuring soil deformation in geotechnical models using digital images and PIV analysis. Proceedings of the 10th International Conference on Computer Methods and Advances in Geomechanics. Tucson, Arizona. pp 997-1002 pub. Balkema, Rotterdam.

White D. J., Take W.A, Bolton M.D. & Munachen S.E. (2001b) A deformation measuring system for geotechnical testing based on digital imaging, close-range photogrammetry, and PIV image analysis. Proceedings of the 15th International Conference on Soil Mechanics and Geotechnical Engineering. Istanbul, Turkey. pp 539-542. pub. Balkema, Rotterdam.

White D. J. (2002) An investigation into the behaviour of pressed-in piles. University of Cambridge PhD Dissertation.

# ***Appendix B***

